Active Flow Control of a Boundary Layer Ingesting Serpentine Diffuser

by

Neal A. Harrison

Thesis submitted to the faculty of Virginia Polytechnic Institute and State University
in partial fulfillment of the requirements
for the degree

Master of Science
in
Aerospace Engineering

Approved by:

Dr. Wing F. Ng, Committee Co-Chairman
Dr. William H. Mason, Committee Co-Chairman
Dr. William J. Devenport

July 13, 2005
Blacksburg, Virginia

Keywords: active, flow control, serpentine, diffuser, duct, inlet, distortion, swirl, boundary layer ingestion, BLI, AFC, aerodynamics

Active Flow Control of a
Boundary Layer Ingesting Serpentine Diffuser

Neal A. Harrison

(ABSTRACT)

The use of serpentine boundary layer ingesting (BLI) diffusers offers a significant benefit to the performance of Blended Wing Body aircraft. However, the inherent diffuser geometry combined with a thick ingested boundary layer creates strong secondary flows that lead to severe flow distortion at the engine face, increasing the possibility of engine surge. This study investigated the use of enabling active flow control methods to reduce engine-face distortion.

An ejector-pump based system of fluidic actuators was used to directly manage the diffuser secondary flows. This system was modeled computationally using a boundary condition jet modeling method, and tested in an ejector-driven wind tunnel facility. This facility is capable of simulating the high-altitude, high subsonic Mach number conditions representative of BWB cruise conditions, specifically a cruise Mach number of 0.85 at an altitude of 39,000 ft.

The tunnel test section used for this experiment was designed, built, and tested as a validation tool for the computational methods. This process resulted in the creation of a system capable of efficiently investigating and testing the fundamental mechanisms of flow control in BLI serpentine diffusers at a minimum of time and expense.

Results of the computational and wind tunnel analysis confirmed the large potential benefit of adopting fluidic actuators to control flow distortion in serpentine BLI inlets. Computational analysis showed a maximum 71% reduction in flow distortion at the engine face through the use of the Pyramid 1 ejector scheme, and a 68% reduction using the Circumferential ejector scheme. However, the flow control systems were also found to have a significant impact on flow swirl. The Pyramid 1 ejector scheme was found to increase AIP flow swirl by 64%, while the Circumferential ejector scheme reduced flow swirl by 30%. Computational analyses showed that this difference was the result of jet interaction. By keeping the jet flows separate and distinct, the diffuser secondary flows could be more efficiently managed. For this reason, the most practically effective flow control scheme was the Circumferential ejector scheme.

Experimental results showed that the computational analysis slightly over-predicted flow distortion. However, the trends are accurately predicted despite slight variances in freestream Mach number between runs and a slightly lower tested altitude.

Acknowledgements

Foremost, I would like to thank my family for their unwavering support throughout the years of my education. Their guidance, advice, and encouragement have made all of my accomplishments possible; I could not have done this without you.

I would like to thank my advisors: Dr. Wing Ng, Dr. William Mason, and Dr. William Devenport for the benefit of their guidance, experience, and encouragement.

I would like to thank the employees of Techsburg, Inc.. In particular, I would especially like to thank Dr. Jason Anderson, Severin Kempf, and Dr. Jon Fleming for their continued support and guidance.

This work was supported by NASA Langley under the Ultra Efficient Engine Technology (UEET) initiative, contract NAS1-03066. The contract monitor at NASA was Ms. Susan A. Gorton.

Table of Contents

List of Figures

List of Tables

Nomenclature

p_t – total pressure
q – dynamic pressure
ρ - density
u – flow velocity
M – Mach number
Re – Reynolds Number
μ - fluid viscosity
ν - kinematic viscosity
p – static pressure
$\dot{m}$ – mass flow
A – area
γ - ratio of specific heats
T – temperature
R - Universal Gas constant
δ - boundary layer thickness
δ^* - boundary layer displacement thickness
θ - boundary layer momentum thickness
H – Boundary layer shape function
C_f – skin friction coefficient
DC(60) – Circumferential Distortion Coefficient
SC(60) – Swirl Distortion Coefficient
AIP – Aerodynamic Interface Plane
CFD – Computational Fluid Dynamics
BWB – Blended Wing-Body
BLI – Boundary Layer Ingesting/Ingestion
RANS – Reynolds Averaged Navier Stokes
SLA – Stereo-lithography
UAV – Uninhabited Air Vehicles
S-A – Spalart-Allmaras Turbulence Model
AFC – Active Flow Control
PFC – Passive Flow Control

Subscripts

t - total conditions
∞ - freestream conditions
i – at duct inlet

Chapter 1: Introduction

Aircraft design has undergone tremendous progress over the last 100 years in moving from the original Wright flyer to the modern wide-body commercial airliners of today. Despite these advances, the now-common tube and wing aircraft configuration has remained essentially unchanged in form since the 1950s, with little significant deviation.[1] However, over the last decade enabling technologies and new mission requirements have changed the very way that airplanes are designed and built. The Blended Wing Body (BWB) concept offers a significant deviation from the traditional aircraft configurations of today, and promises substantial improvements over conventional performance expectations. One of the most promising elements of this design is the incorporation of boundary-layer-ingesting serpentine engine inlets.

1.1: Motivations for Adopting Serpentine Boundary Layer Ingesting Diffusers

1.1.1: Serpentine Diffusers

Serpentine (or offset) diffusers allow for a centerline engine placement by ingesting the intake flow through an S-shaped duct. In this configuration, engines can be directly incorporated into an aircraft's airframe providing a number of benefits including increased accessibility for engine maintenance, drag reduction, and the reduction of thrust-related pitching moments. This type of diffuser was first incorporated into commercial aircraft in the early 1960's into designs such as the Hawker-Siddeley Trident, Boeing 727, and Lockheed L-1011.

In more recent years, serpentine ducts have been increasingly incorporated into newer aircraft designs due to their potential benefits. The explosion of interest in Uninhabited Air Vehicles (UAVs) has brought the use of serpentine diffusers to the forefront due to their inherent stealth capabilities and life-cycle cost implications.[2] And, because these aircraft are typically used for high-risk reconnaissance operations, they need to be as stealthy and cost-effective as possible.

Serpentine ducts have stealth implications because the engine face is a major source of radar signature. A primary method of signature reduction in military aircraft is

achieved by integrating the engine into the aircraft using a serpentine diffuser, which prevents direct radar line-of-sight to the engine face. Submergence of the engine inlet reduces the inlet ram drag as compared to a conventional pylon-mounted engine, and decreases the wetted area of the installation, thereby reducing the aircraft's parasitic drag. The elimination of the pylon also results in a decrease in weight due to the removal of the required supporting structure. If the engine is located judiciously, thrust-related pitching moments can also be decreased by locating the engines closer in line with the aircraft's center of gravity -- a large benefit for "flying-wing" or tailless configurations which require significant control authority in order to nullify these moments during flight. With so many benefits to aircraft design, it is no wonder that many modern tailless aircraft are adopting serpentine engine inlet diffusers.

1.1.2: Boundary Layer Ingestion

To ensure maximum performance commercial aircraft engines are typically located in areas where the flow is relatively unobstructed, ensuring that the air captured by the diffuser is essentially uniform. Locations such as wing pylons provide the engine with a stream of relatively undisturbed flow. However, additional propulsive benefit can be derived from serpentine diffusers if the design also incorporates high levels of boundary layer ingestion (BLI), as indicated in Figure 1.1.

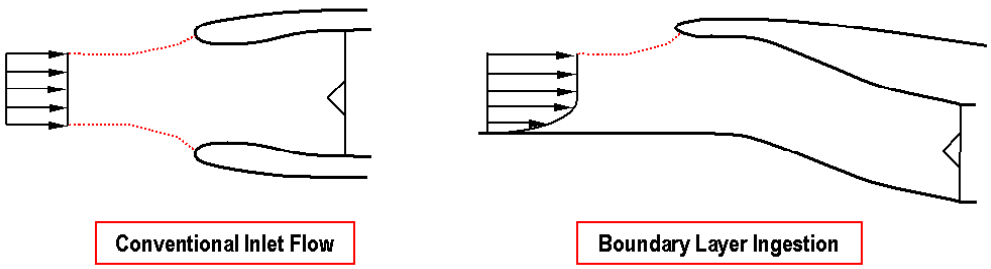

Figure 1.1: Conventional vs. Boundary Layer Ingesting Inlets

By ingesting some of the boundary layer fluid, an effective increase in the aircraft's lift-to-drag ratio can be realized through the benefits of wake ingestion and wake filling.[3] The result is a decrease in operational fuel expenditure, and a decrease in overall aircraft life-cycle cost. At present, this type of installation is more typical of military aircraft configurations where it is often more critical to block direct line-of-sight

to the engine face than worry about the aerodynamic consequences of adopting such a geometry. One of the major exceptions to the "typical" aircraft configurations is the NASA/Boeing Blended Wing Body (BWB) shown in Figure 1.2.

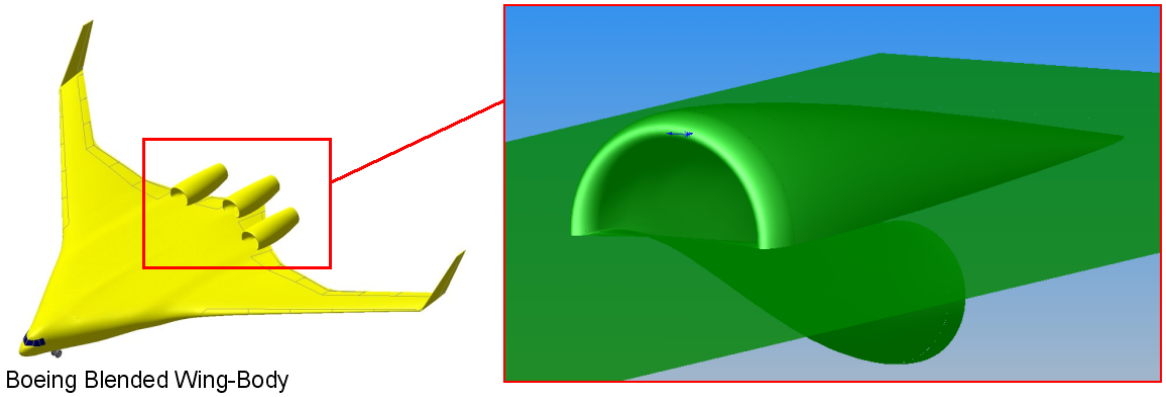

Figure 1.2: BWB Aircraft with a BLI Serpentine Inlet

The BWB is a flying-wing concept capable of significant performance benefits over the conventional tube-and-wing construction. Of particular interest is the incorporation of serpentine engine inlet diffusers coupled with significant amounts of boundary layer ingestion. If adopted, this configuration promises to have a large advantage over aircraft constructed using a more conventional design. In order to realize the large potential benefits, it will first be necessary to overcome the primary difficulty with serpentine BLI inlets, namely engine-face flow distortion.

1.2: Flow Mechanisms of a BLI Serpentine Diffuser

1.2.1: Curvature and Swirl

A primary type of engine-face distortion associated with engine-inlet compatibility is the creation of flow swirl. Swirl represents non-axial or cross-flow velocities, and is especially prominent in serpentine ducts due to their physical curvature. More specifically, swirl develops in these types of ducts due to the centrifugal forces associated with turning the flow through curves in the diffuser. As the flow passes through the first bend of a serpentine diffuser, a centrifugal pressure gradient proportional to $\rho u^2/R$ exerts a force on the fluid.[4] As a result, greater force is exerted on the fluid at the outside of the bend and a strong transverse pressure gradient is created across the duct. This gradient drives the flow on the outside of the turn in towards the inside turn, establishing a secondary flow field, as shown in Figure 1.3. The secondary flows have the

effect of driving the low-momentum boundary layer fluid from the periphery of the duct towards the inside turn. This fluid then collects on the inside of the turn forming an area of total pressure deficit.

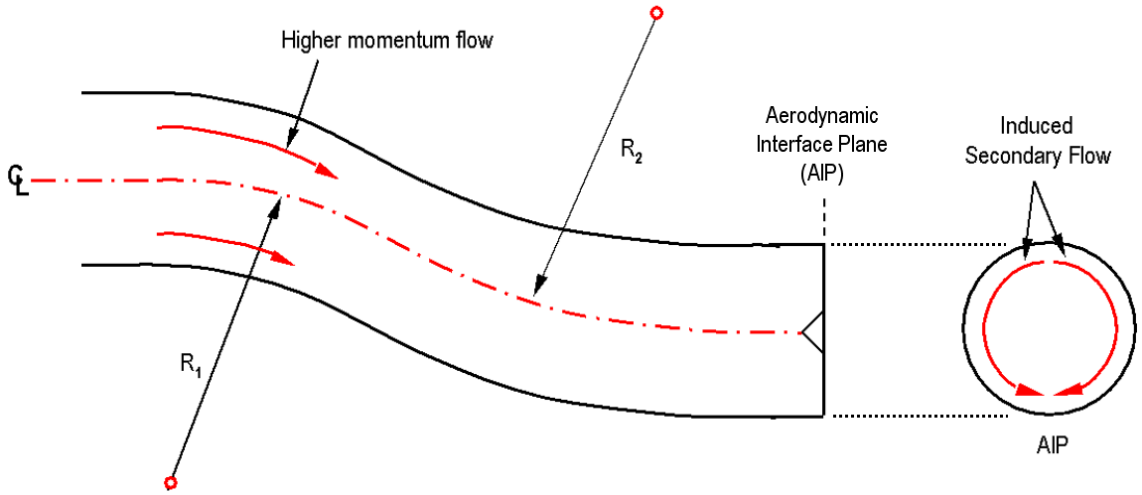

Figure 1.3: Effect of Centrifugal Forces

In a complete serpentine diffuser, it might be expected that the second duct turn would reverse some of the distortion as it should establish the reverse pressure gradient. However, once the first turn is completed, much of the low momentum fluid has gathered on the outside of the second turn. Though the low-momentum fluid has been relocated to the outside turn, a strong reverse pressure gradient is not established to help drive the flow back in the opposite direction. Therefore, if allowed, the secondary flows will establish strong pressure gradients that lead to large flow distortion. Guo[5] established a relationship correlating the increase in the flow swirl with an increase in total pressure distortion. These elements are intuitively related; their combined effects will be examined later in this report.

1.2.2: Boundary Layer Ingestion

Boundary layer ingestion provides an additional complication to the creation of flow distortion. In practice if the engine is not located in an area that provides uniform flow to the inlet (particularly when the engines are mounted next to the aircraft fuselage) the boundary layer is usually diverted away from the inlet. Boundary layer diverters and splitter plates can effectively prevent boundary layer ingestion, but also

contribute to the aircraft's drag. More importantly, if the boundary layer is ingested as indicated in Figure 1.4, it can cause a large increase in engine-face distortion.

Because a serpentine inlet creates non-uniformity in the flow due to differences in centrifugal forces, the typical distortion problem is further compounded by supplying areas of low momentum flow from the boundary layer to the diffuser inlet; flows that are easily influenced by pressure gradients.

In addition, the interaction of vorticity present in the boundary layer with the nacelle-body junction can cause the formation of a junction (or horseshoe) vortex. This vortex has the same sense of rotation as the secondary flows formed by the centrifugal forces, and thus increases the severity of the flow distortion at the engine face – also know as the Aerodynamic Interface Plane (AIP). The presence of this vortex is highlighted by Figure 1.4 which shows the fluid downstream of the junction being drawn down and towards the center of the inlet.

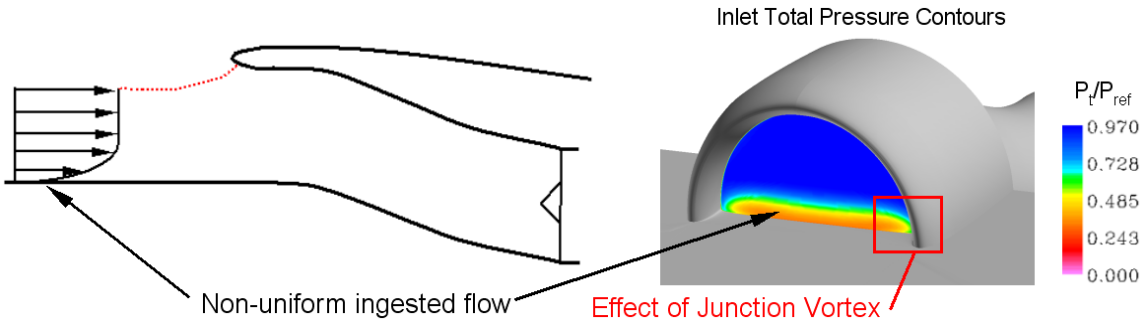

Figure 1.4: Non-Uniform Ingested Profile

1.2.3: Combined Flow Effects

Due to the physical curvature of serpentine inlets, the flow has a tendency to separate in areas of strong adverse pressure gradients, as well as induce strong secondary flows throughout the duct. Increased total pressure losses, as well as severe flow distortion at the engine-fan interface are characteristic of these types of systems. This trend is only increased in severity when coupled with designs that incorporate high levels of boundary layer ingestion. By introducing low momentum fluid to the inside turn of a serpentine duct, the severity of the cross-flow pressure gradients is increased. The high-momentum fluid from the outside turn collects the boundary layer fluid at the bottom of

the duct creating a substantial circumferential total pressure distortion as depicted in Figure 1.5.

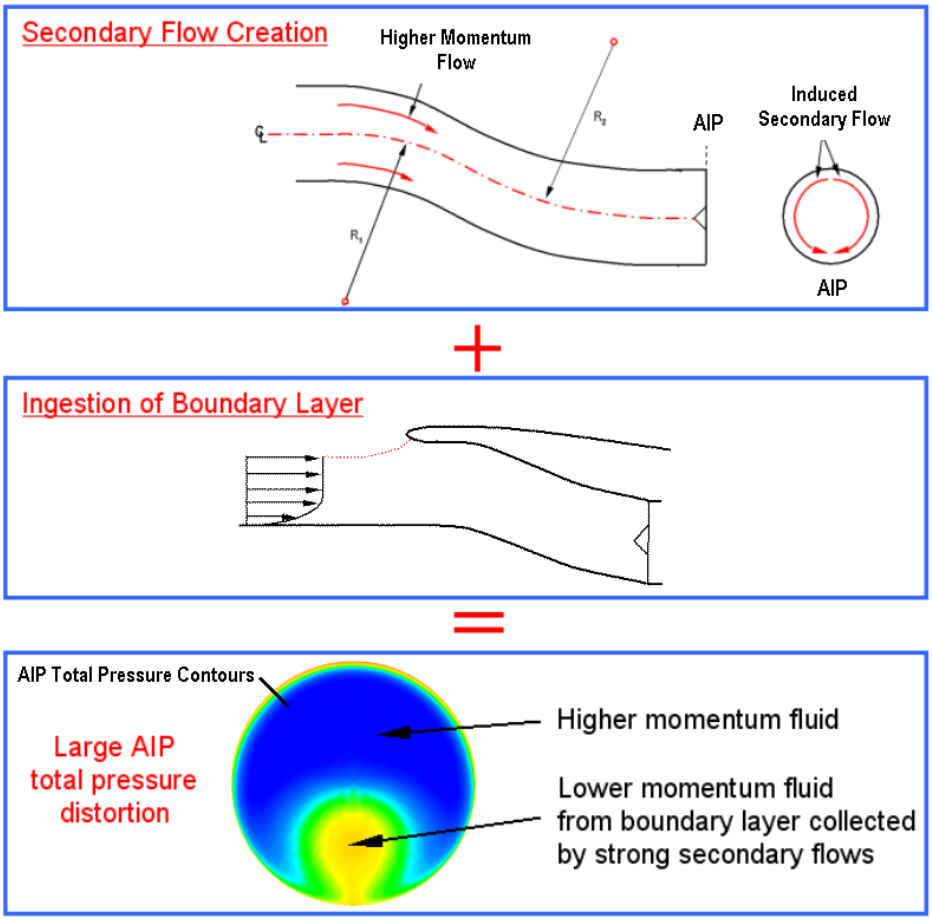

Figure 1.5: Serpentine BLI Inlets and Distortion .

1.3: Implications of Adopting BLI Serpentine Diffusers

Despite the many benefits that can be realized when adopting serpentine BLI inlets into an aircraft design, this type of system is not without its share of drawbacks. Flow complexities created by the geometry have negative impacts on overall engine and propulsive efficiency. The most severe of these elements are the creation of engine-face total pressure distortion and swirl.

1.3.1: Flow Distortion

The primary function of an engine intake duct is to deliver uniformly distributed airflow at a prescribed velocity to the AIP. A non-uniform airflow is considered to be

distorted. Historically, experimentalists have found it is easiest to measure total pressure at the AIP, and thus, distortion descriptors are generally based on total pressure. These descriptors are described later in section 2.3.1. Distortions can also be steady or unsteady as the result of cruise and maneuver conditions. (This study will focus only on steady-state conditions.) Practically speaking, to a certain extent there is always some level of flow distortion at the AIP. However, due to the efforts of inlet designers, this distortion usually lacks the intensity and extent to make an impact on engine operation. AIP distortion can be categorized into two main types: radial and circumferential. In general, radial distortion (along blade span) can be neglected, allowing for the majority of focus to be based upon circumferential distortion.[4] Circumferential distortion has a number of impacts on practical engine operation.

Most importantly, circumferential distortion has a direct impact on engine compressor operation, as depicted in Figure 1.6.

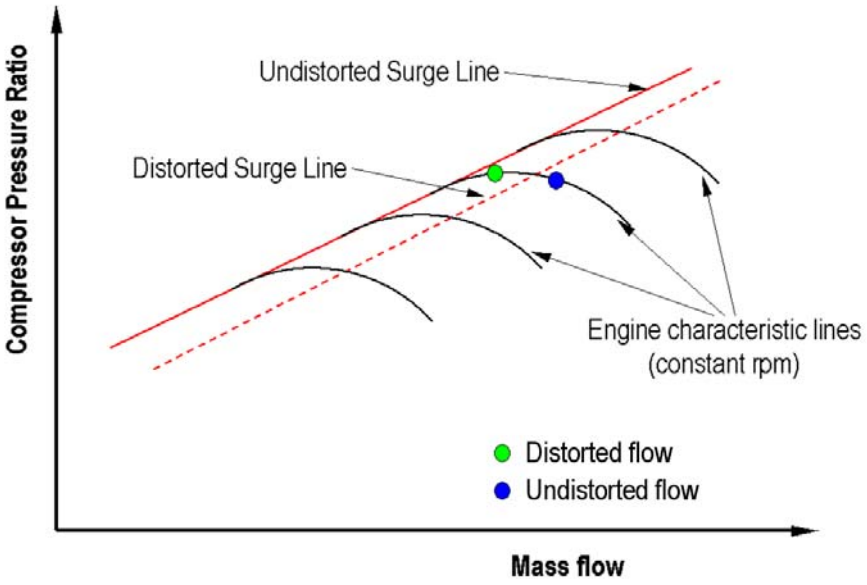

Figure 1.6: Representative Compressor Map

When the flow reaches the AIP and there is a substantial variation in total pressure across the face, more work is done by the compressor on the low total pressure flow (distorted) than on the higher total pressure flow (undistorted). These low and high total pressure flows operate at different points along the compressor characteristic, as noted in Figure 1.6. The distorted flow operates closer to the surge line of the compressor than the undistorted flow, thereby reducing the overall operational surge margin. This can

trigger a rotating stall, and if of significant extent can cause the compressor to surge. Consequently, total pressure distortion moves the engine operating point closer to the surge line. In order to operate the compressor with a safe surge margin, the engine must operate lower on the characteristic (i.e. at a lower compressor pressure ratio) thereby forcing a reduction in usable engine performance.

From a structural standpoint, circumferential distortion creates a cyclical loading/unloading of the compressor blades. These cyclical stresses create a high fatigue load on the blades and significantly reduce the life-cycle of the engine.[2]

1.3.2: Swirl

Flow swirl can also have serious implications on engine operation by altering the local angle of attack for individual compressor blades. Depending on the severity and orientation of the swirl, these angles can be varied to the extent that some blades of the compressor may stall, thereby reducing efficiency and possibly triggering a rotating stall.

1.4: Research Motivation and Objective

To realize the substantial performance benefits of serpentine BLI diffusers[3], this study investigated the use of flow control methods to reduce AIP flow distortion. Computational methods and novel flow control modeling techniques were utilized that allowed for rapid, accurate analysis of flow control geometries. Results were validated experimentally using an ejector-based wind tunnel facility capable of simulating the high-altitude, high subsonic Mach number conditions representative of BWB cruise conditions.

Chapter 2: Managing Flow Distortion

For boundary layer ingesting serpentine ducts to be incorporated into aircraft designs, methods to eliminate or reduce flow distortion must be developed. Fundamental investigations of the mechanisms of flow distortion in serpentine ducts by Vakili et al.[6] revealed that the formation of strong secondary flows are primarily responsible for creating distorted airflows, as described in section 1.2.1. These examinations helped to create benchmark data for categorizing the secondary flow within offset ducts and their effect on duct pressure recovery. Once the fundamental mechanisms were understood, it was possible to move towards solutions that could successfully counter the effects of secondary flows, and thereby reduce flow distortion in BLI serpentine inlets.

2.1: Passive Flow Control

2.1.1: Serpentine Diffusers

In the case of simple offset diffusers, the primary mechanism for improvement in duct pressure recovery was based upon the prevention of flow separation within the duct. Early investigations focused on the application of physical systems such as vane-type vortex generators to counter the adverse effects of strong secondary flows and ultimately prevent any adverse flow behavior. By implementing vortex generators to re-energize the flow in areas of strong adverse pressure gradients, secondary flow strengths were reduced and flow separations were delayed. This resulted in improved AIP flow uniformity and pressure recovery.

One of the earliest practical examinations of this problem occurred during the original design of the Boeing 727.[7] During original flight testing it was found that center engine surge was experienced as a result of flow distortion created by the clean offset diffuser geometry. In order to meet required performance levels, various configurations of vane-type vortex generators were installed and tested. A final configuration of two rows of generators allowed for surge-free operation up to altitudes of 40,000 ft, and was found to drastically reduce distortion while providing increased duct pressure recovery. More fundamentally, test data indicated that flow distortion was primarily a function of inlet flow Mach number.

Vakili et al.[8] continued to investigate secondary flows in more aggressive offset geometries and categorized the behavior of separation-induced vortex lift-off resulting from strong secondary flows. They investigated various passive flow control devices including counter-rotating vane generators and rail-type generators. Benchmark quality results showed that only the counter-rotating vane configuration was successful in countering the secondary flows, thereby reducing flow distortion and increasing pressure recovery.

Reichert and Wendt[9] used low-profile wishbone type vortex generators to examine some of the fundamental performance characteristics of vortex generators. By varying height, spacing, and location of the effector arrays, some fundamental principles were established. It was determined that mixing performance of the generators is determined by the strength and downstream interaction of the resultant vortices. While strength is a function of generator size, downstream interaction is a function of generator spacing. Reichert et al. also determined that the most effective vane-type generator had a height equal to the local boundary layer thickness, and was located upstream of any disturbances in order to provide the appropriate length for vortex interaction. The resulting upstream shift was shown to have little effect on generator effectiveness as compared with the potentially large penalty associated with being too close to any separation points. It is also noted that generators are most effective when located in the low-momentum (boundary layer) fluid, with little benefit derived from placement in undisturbed flow.

A computational examination of distortion was implemented on the re-engine program for the Boeing 727 center engine nacelle.[10] This study showed that vortex generator performance was primarily a function of three variables: duct Mach number, aerodynamic characteristics of the duct, and the design parameters related to geometry, placement, and arrangement of the generators within the duct. It was also found that blade height, blade chord, and angle of attack are the most important generator characteristics. Investigations also documented a dramatic shift in flow control strategy. This strategy resulted in a shift from a local to a global mentality when examining inlet distortion. It was found that improved results (i.e. lower distortion) could be achieved by

moving focus away from the prevention of separation to an overall management of secondary flows within the diffuser.

Reichert and Wendt[11] further explored the use of tapered-fin type generators to investigate their effect on secondary flow control. Their results showed that when employing generators for secondary flow control significant reduction in flow distortion could be achieved. However, there was little impact on inlet total pressure recovery.

2.1.2: Boundary Layer Ingesting Serpentine Diffusers

The problem of flow distortion in serpentine diffusers becomes more severe when coupled with large amounts of boundary layer ingestion due to the introduction of ingested flow non-uniformity. This type of configuration is typical of a BWB aircraft, which utilizes aft-mounted engines that are buried into the top of the aircraft fuselage in order to realize certain propulsive benefits. Due to the increased severity of distortion in these conditions, it becomes of increasing importance to develop flow control strategies to enable the use of such configurations.

Anabtawi et al.[12] examined the use of vane-type vortex generators in a boundary layer ingesting offset diffuser and their effect on flow distortion. Anabtawi et al. found that in order for the generators to influence the boundary layer and to induce a change in the diffuser secondary flow, they had to have a height on the order of the boundary layer thickness. The optimum configuration tested had a mix of various generator heights due to variation in local boundary layer thickness. Due to the losses associated with such large generators it was suggested that coupling passive flow control with other methods could help reduce the distortion.

When coupled with inlets that have significant amounts of boundary layer ingestion, vane-type generators are typically used to ‘re-energize’ or ‘mix’ the boundary layer fluid with higher-momentum fluid from the freestream. Due to the scale of the necessary generators and their created vortices, it becomes much more difficult to manage secondary flows within the duct in such a way as not to produce large amounts of swirl. In addition, the scale also suggests that large losses in duct pressure recovery would be associated with such systems due to the viscous losses resulting from skin friction on the effectors.

2.2: Active Flow Control

An alternative to passive control, although more complex and costly, offers the opportunity to provide effective flow control in a variety of flight conditions without the losses associated with physical generators. This alternative is known as active flow control and uses embedded vortex generating jets to add vorticity to combat flow distortion and either reduce or eliminate flow separation. As these jet-based systems are not constrained to one configuration, arrays of jets are adaptable to any flight condition, and can be turned on, adjusted, or turned off as needed. When coupled with a closed-loop feedback controller and a network of sensors to detect flow conditions, the result is a highly adaptive and efficient system capable of maintaining low-distortion flow at the engine-diffuser interface.

Gorton et al.[13] experimentally investigated unsteady active flow control on a boundary layer ingesting inlet at low Mach numbers. The study investigated the feasibility of flow control to reduce distortion in a BLI inlet the acceptable level of DC(60)q = 0.10. (The DC(60)q distortion parameter is defined in section 2.4.) Tests showed that the required distortion level could be achieved with active flow control, and laid the groundwork for further investigations using high Mach number analysis and testing.

Allan et al.[14,15] investigated the use of vortex-generating jets to manage flow distortion using computational methods. They showed that significant benefit could be derived from the use of vortex generating jets, with significant reductions in distortion for jet mass flows greater than 2% of the inlet mass flow. Allan suggests that further study into jet placement would be required to achieve the desired distortion level of 0.10. Baseline (no flow control) distortion was over-predicted by the flow solver they used as compared with wind tunnel results at high Reynolds numbers. Allan also added that significant effort was required to grid the individual generators and jets, and that the results would be used to investigate the use of source-term modeling to facilitate quicker results for fundamental investigations.

Over the years, extensive research has been conducted to evaluate devices such as vortex generators to effectively reduce the flow distortion resulting from serpentine duct geometries. Computational and experimental testing has been conducted using active

flow control at low Mach numbers, although experimental verification of results for high Mach numbers is as yet incomplete. Computational analysis of active flow control has been extensive. Results have shown that to achieve the required distortion level, jet mass flows of greater than 2% of engine mass flow will be required.

Since designers are reluctant to sacrifice engine performance by expending bleed air for flow control purposes, the current study will further investigate the use of an ejector-pump based system of jets to help minimize the bleed air requirements while still maintaining the required jet mass flow rates.

2.3: The Ejector Pump and Flow Control

Air used in active flow control is typically bled from the engine compressor. As such, the greater the required flow control effort, the greater the penalty on engine performance. Typical flow control systems are allowed up to 1% of the engine mass for use in flow control systems.[15] To maximize the possible effectiveness of active flow control jets, an ejector pump system of fluidic jets could be used to boost the system performance. The ejector concept couples the use of a motive jet with suction to increase total jet mass flow, as depicted in Figure 2.1.

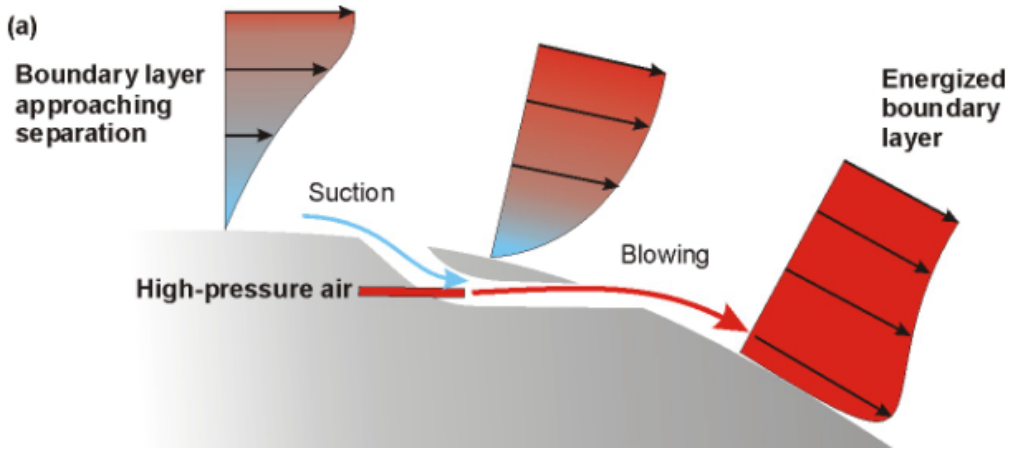

Figure 2.1: Ejector Pump Principle

To increase jet effectiveness, the ejector pump utilizes a high-pressure motive jet to entrain additional air mass into a core jet. The motive jet creates an area of locally lower static pressure behind the jet. When this area is connected to a plenum chamber of higher static pressure, fluid is entrained into the jet according to the Venturi effect. Thus, air from a higher static pressure is drawn into the low pressure region created by the jet and entrained into the jet core flow. By locating the plenum chamber under the surface of a body, fluid from the flow boundary layer can be drawn into the plenum chamber, providing a measure of boundary layer suction.

The effectiveness of the ejector pump is also aided by taking advantage of existing pressure gradients. By locating the suction in areas of locally high pressure, and the jets in areas of lower pressure, a natural pressure gradient is established and additional system effectiveness is obtained. When aided by existing pressure gradients,

motive to suction mass flow ratios of 1:1 can be realistic performance expectations.[16] Thus, the ejector-pump approach can yield blowing mass flow rates of up to 2% of the total duct mass flow at the bleed expenditure of only 1% of the total mass flow while simultaneously providing 1% of mass in flow suction.

2.4: Distortion Descriptors

To characterize the flow at the AIP, several descriptors are available that characterize the various elements of distortion. The primary of these descriptors are the DC(60) parameters.[4] These examine the flow distortion based upon measurements obtained from a six-arm distortion rake that measures total pressures in 60° sections. Each arm has five probe measurement locations that are located such that they each represent an equal area-averaged section of the 60° wedge, as shown in Figure 2.2. Values from this rake are then used to determine the flow distortion at the AIP. However, for computational analyses, the 60° sector values were interpolated using the whole wedge (to increase accuracy), while experimental values utilized the rake measurements to determine an area-average result.

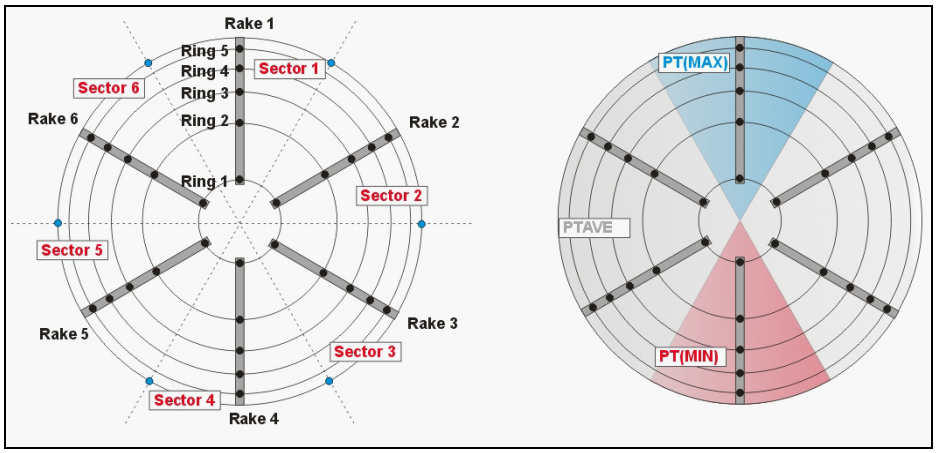

Figure 2.2: DC(60) Distortion Rake

The DC(60)pt value is used as a general flow health monitoring parameter by determining the 'worst' case for a 60° sector of the flow.

$$DC(60)pt = \frac{PT_{MAX} - PT_{MIN}}{PT_{AVE}} \qquad (2\text{-}1)$$

The DC(60)q parameter is the most common of the DC(60) parameters and examines the ratio of the difference between the average and minimum total pressure sectors and the face dynamic pressure. This parameter determines the average flow distortion and compares it to dynamic pressure; this can roughly serve as a non-dimensionalization by the flow kinetic energy, which is related to distortion severity.

$$DC(60)q = \frac{PT_{AVE} - PT_{MIN}}{q_{AVE}} \tag{2-2}$$

The flow at the AIP can also be characterized by examining the magnitude of the secondary flow or swirl velocities.[5] The SC(60) parameter provides a measure of the severity of the secondary flows and characterizes the non-axial flow that could lead to a stalling of the compressor blades:

$$SC(60) = \frac{V_{CF\_MAX} - V_{CF\_MIN}}{V_{AVE}}\ , \tag{2-3}$$

where V_{CF_MAX} represents the maximum average secondary flow over a 60° sector, V_{CF_MIN} represents the minimum average secondary flow over a 60° sector, and V_{AVE} represents the average flow velocity at the AIP

Another typical duct flow descriptor is the inlet pressure recovery. This parameter characterizes the efficiency of the diffuser to convert kinetic energy to pressure energy.

$$PR = \frac{AIP\ Total\ \ pressure}{Freestream\ Total\ \ pressure} \tag{2-4}$$

Additional distortion descriptors used in this study are based upon standards proposed by SAE-ARP1420.[17] The parameters use the standard distortion rake to characterize circumferential, radial, and average (DPCPavg) distortion intensity. These parameters are more complicated to calculate, but can provide a more detailed analysis of the flow distortion.

Refer to Appendix A for a more complete description of all distortion parameters used in this analysis.

2.5: Study Approach

This study will focus on the computational design and experimental validation of fluidic vortex generators for the purpose of reducing flow distortion in BLI serpentine inlets. Fluidic generators have been chosen over their vane-type counterparts because

they are non-intrusive (i.e. they contribute less loss) and their flow control effect can be varied in location and magnitude. The inlet aerodynamic effects of using the simulated ejector-pump concept to augment the thrust from the fluidic vortex generators will also be analyzed.

The computational analysis will be based upon investigation that utilizes a novel jet modeling technique in order to analyze multiple jet configurations and investigate the fundamental mechanisms of fluidic vortex generating jet effectiveness.

Results will be verified experimentally at flight Mach number (~0.85) for selected configurations to verify the validity of the computational approach. The Techsburg wind tunnel will be used to simulate the low pressure, high subsonic Mach number cruise conditions typical of the BWB. This is accomplished by using an ejector-pump based system, which offers significant advantage over systems such as the NASA 0.3m cryogenic tunnel which utilizes helium in order to obtain the desired simulated flight condition -- a feature that adds complexity and cost to the system.

Chapter 3: Computational Analysis

The computational analysis focused on the evaluation of the vortex generator flow control configuration in several stages. In the first phase, baseline flow distortion was analyzed in order to provide a benchmark result for comparison with accepted data. In the second phase, the flow control was analyzed using boundary conditions for jet modeling that allowed for rapid analysis of jet performance and fundamental flow investigations.

3.1: Flow Domain and Mesh Generation

3.1.1: Computational Domain

The computational domain was created to simulate one half of a center-mounted engine in a BWB configuration as represented in Figure 3.1. The computational domain was required to simulate both duct capture and a portion of the bypass flow. The precise inlet geometry for this study was defined by NASA configuration 'A'. (Geometry details are outlined in detail in Appendix B.)

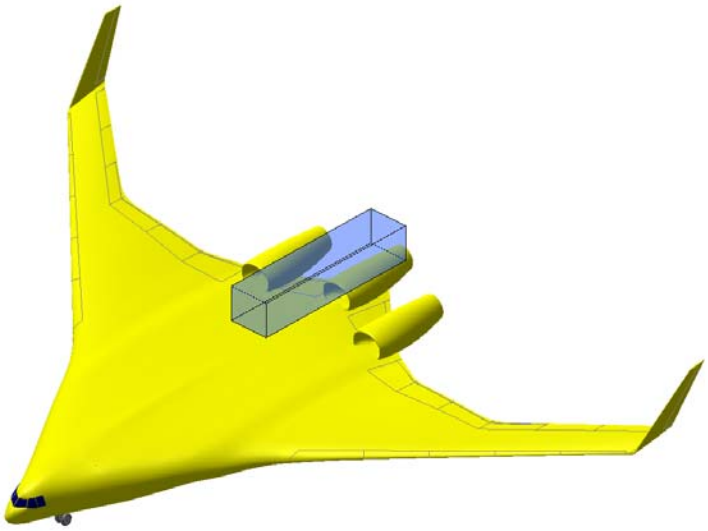

Figure 3.1: Extent of Computational Domain

To simulate the BWB flight condition, the domain had to simulate the appropriate boundary layer thickness and Mach number consistent with this type of installation. The design requirement for the simulation is depicted in Figure 3.2: an ingested boundary layer thickness of approximately 30% of the total inlet height at a freestream Mach number of M = 0.85, and altitude of ~39,000 ft.

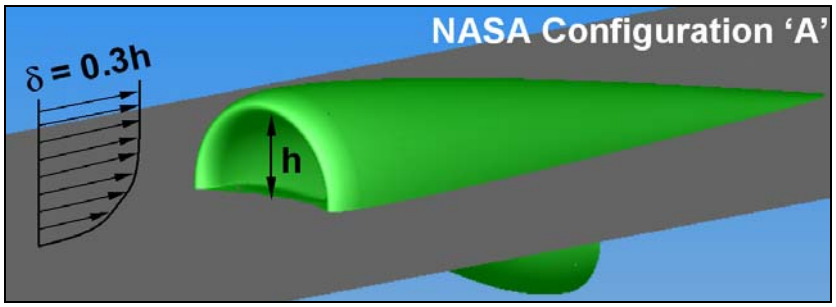

Figure 3.2: 30% Boundary Layer Ingestion

3.1.2: Computational Grid

The domain grid for the analysis was created using the mesh generator Gridgen.[18] The general mesh topology was based upon a multiple-block structured grid, and was created to be compatible with the multi-grid solving capability of the CFD code ADPAC[19] (**A**dvanced **D**ucted **P**ropfan **A**nalysis **C**ode discussed in Section 3.3). The completed grid consisted of 10 blocks and a total mesh size of ~ 2.7 million nodes. Near wall spacing was created with a nominal y+ ≈ 1 to fully capture the boundary layer. General grid topology is shown in Figure 3.3.

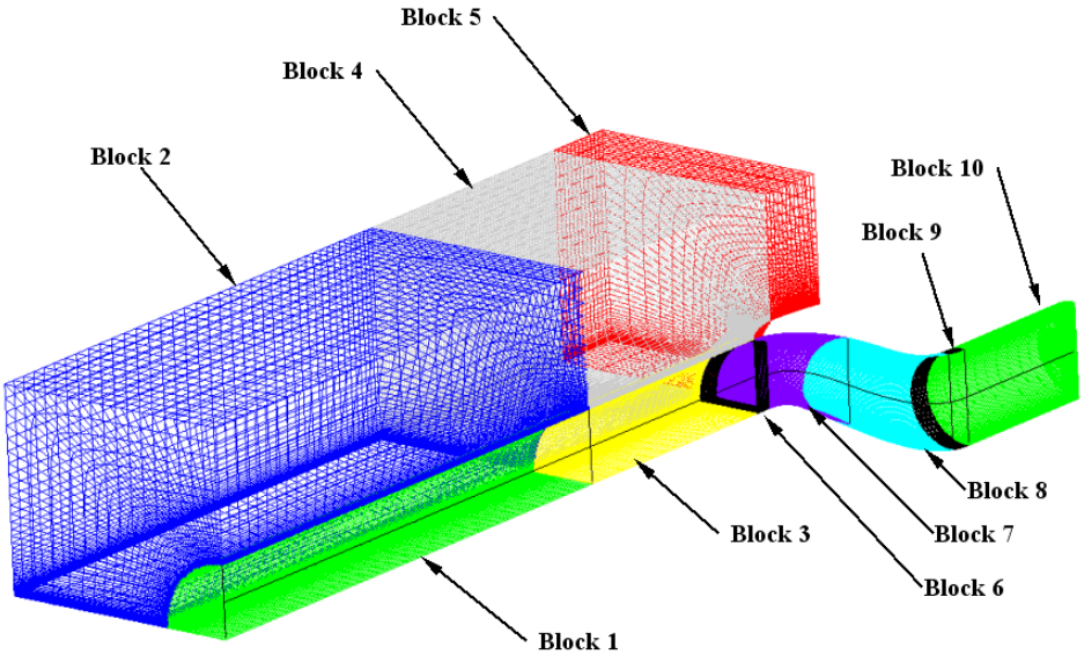

Figure 3.3: Block Topology of Computational Domain

Blocks 1-4 were used to 'grow' the boundary layer to the desired 30% thickness, and simulate the freestream flow. Block 5 diverts the bypass air around the external engine nacelle. Blocks 6-9 represent the inside of the diffuser. Block 10 was added to the end of

the diffuser so that boundary conditions were not imposed directly at the AIP, which could have influenced the calculated distortion values.

Due to the limitations of structured mesh geometries, it was not possible to individually address different areas of interest using differing cell spacings. Thus, to closely manage the size and shape of the cells in the near wall region in the duct, mesh cell concentrations were established by using a polar mesh. This allowed for the most even cell spacing with the least amount of skewness. This configuration was determined to be the best meshing geometry for monitoring the secondary flows that move around the periphery of the duct.

3.2: Flow Control CFD Grid Design

To better model the vortex generating jets, the internal duct grid was designed with a high cell density in the axial direction in regions where the flow control would be applied. This enabled more realistic hole sizes and geometries to be modeled, since more control over the sizing of the blowing or suction "hole" size was possible with increased cell density. Figure 3.4 gives a detailed look at the inlet mesh, showing the cell density in close detail. Increased block cell density allowed for higher-fidelity modeling of the local flow field; downstream block cell densities were also increased to capture the increased flow complexity resulting from flow control. A study of the solution dependence on the grid size is detailed in Appendix C.

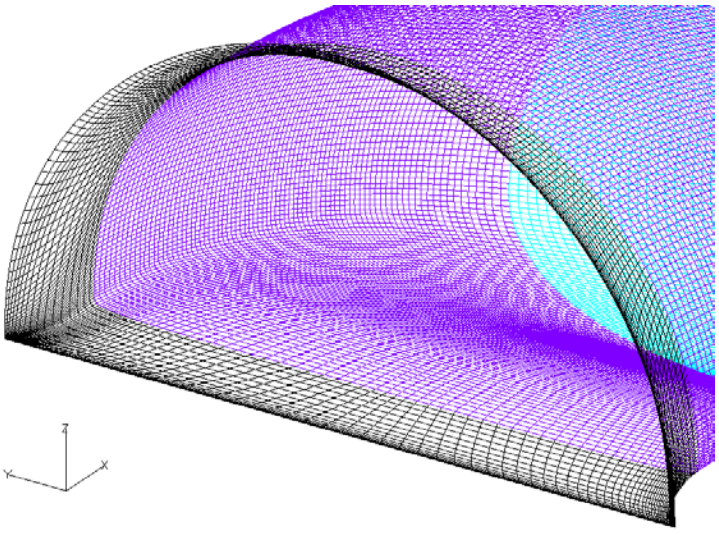

Figure 3.4: Mesh Detail Near Jet Location

3.3: Computational Fluid Dynamics

The CFD solution solver used in this investigation was ADPAC (**A**dvanced **D**ucted **P**ropfan **A**nalysis **C**ode), which was developed by the Allison Engine Company in cooperation with NASA Glenn.[19] The code utilizes a finite volume formulation to solve the Reynolds-Averaged Navier-Stokes (RANS) equations. For a more detailed description, refer to Appendix K.

3.3.1: Boundary Conditions

As noted earlier, the computational domain is intended to simulate the aft portion of a center engine installation on a Blended Wing-Body aircraft. Thus, the boundary conditions must be specified in order to simulate this condition as closely as possible.

The inboard and outboard boundaries were both modeled using a mirror condition (inviscid wall) to simulate the symmetry associated with a centerline engine installation. By modeling half of the inlet, the total computational grid size was decreased. All boundaries coinciding with aircraft surfaces were modeled using a viscous wall condition, while the fore and aft boundaries were used to control the total mass flow and velocity through the block consistent with cruise performance at 39,000 ft. Flow conditions are given below, and are meant to be representative of a BWB aircraft at cruise conditions:

- Freestream Mach Number $M_\infty = 0.85$
- Altitude 39,000 ft
  - Reference total pressure $p_t = 664.58$ lb/ft^2
  - Reference total temperature $T_t = 447.26$ ^oR
- AIP mass flux = $mc/A_{AIP} = 30.8$ lbm/s / ft^2 (corrected mass flow / per unit area)

These conditions were used to set up the CFD analysis. In the design case, this would yield a nominal Mach number of ~0.5 at the AIP. This mass flow is typically related to sea level conditions as a reference:

$$\dot{m}_c = \dot{m}_{actual}\left(\frac{\sqrt{T_{t\infty}/T_{ref}}}{P_{t\infty}/P_{ref}}\right). \qquad (3\text{-}1)$$

To compare CFD results from different sources with different geometries, additional mass flow-related parameters are specified. The AIP mass flux is useful to compare inlets of different physical size[15], and was calculated according to:

$$mc / A_{AIP} = \frac{\dot{m}_c}{A_{AIP}}. \qquad (3\text{-}2)$$

The mass flow coefficient parameter can be used to compare mass flow rates for different flow properties and conditions, as well as different sized inlets[14]:

$$C_{\dot{m}} = \frac{\dot{m}_{actual}}{\rho_\infty V_\infty A_{AIP}}. \qquad (3\text{-}3)$$

Through the use of these parameters computational solutions were compared with similar studies conducted by NASA.

3.3.2: Jet Modeling and Hole Geometry

CFD modeling of the jets for the flow control cases was based upon the simulation of a plenum that supplies air to all of the jets at equal pressure. As such, individual jet mass flows varied according to pressure values near the jets within the diffuser. These boundary conditions were held constant for all configurations tested. Values for the supply pressure were set to simulate compressor bleed air characteristics. Additional details of flow control jet modeling are outlined herein.

The fluidic jets were modeled using ADPAC's INLETG condition at the mesh boundary. The INLETG condition specifies flow total pressure, total temperature, and local flow angle (relative to cell orientation). In the past, computational investigations have typically utilized either source-term modeling (vorticity terms added into the computational domain to simulate vortex generator characteristics), or have modeled individual flow effectors at great time and computational expense.[10,14] By utilizing the wall boundaries for jet modeling, significant simplification of flow control was achieved. This allowed for the examination of a multitude of different jet configurations in a short period of time. The jet modeling concept is shown in Figure 3.5. Thus, the driving parameters of flow control effectiveness could be examined on a fundamental level. To facilitate jet modeling, a clustering of four cells was typically used to represent the blowing holes. (The same technique was used to model the flow suction.) This resulted in

a roughly square geometry for the holes, on average having an approximate area of 0.01 in^2. Because the jets are oriented at a blowing angle of 30° from the wall (jet orientation is detailed in a later section), the jet diameter size is physically scaled by sin(30°). Thus, the actual jet area (from which air is blown) is equal to 0.005 in^2. This resulted in a jet with an area equivalent to a circular jet with a diameter of 0.080 in. (For the duct geometry described in Appendix B.)

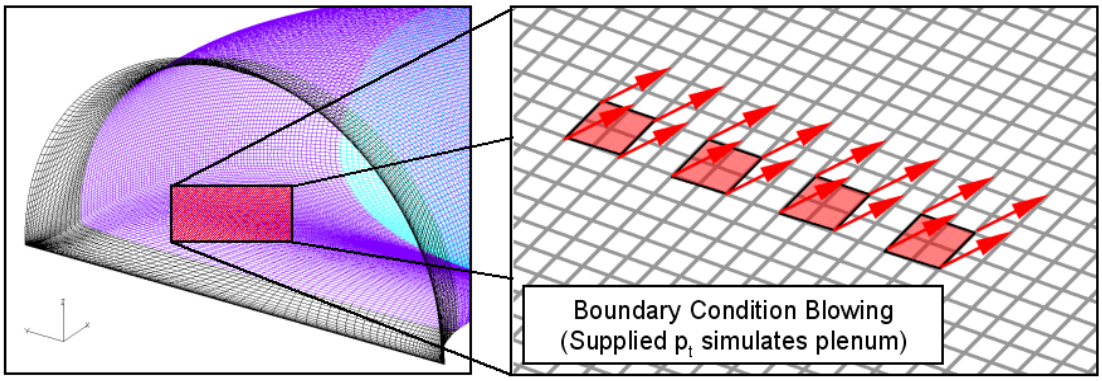

Figure 3.5: Jet Boundary Condition Modeling

The specific impacts of using square holes for the jets as opposed to circular holes was not examined in this study, although it is not believed to have a first-order impact on the results.

3.3.3: The Spalart-Allmaras Turbulence Model

The computational analysis used the one-equation Spalart-Allmaras (S-A) turbulence model. The S-A model was chosen for the study as it is the highest fidelity working turbulence model available in ADPAC[19], and is well established for its separated flow modeling and shock capturing ability. For a more detailed description, refer to Appendix K.

3.4: Solution Convergence

The solution convergence was based upon a relative decrease of the solution error by at least three orders of magnitude from the initial starting value. Duct mass flow and distortion parameters were also monitored for convergence. A representative convergence graph is shown in Figure 3.6. The time required to reach convergence was approximately 8 hours.

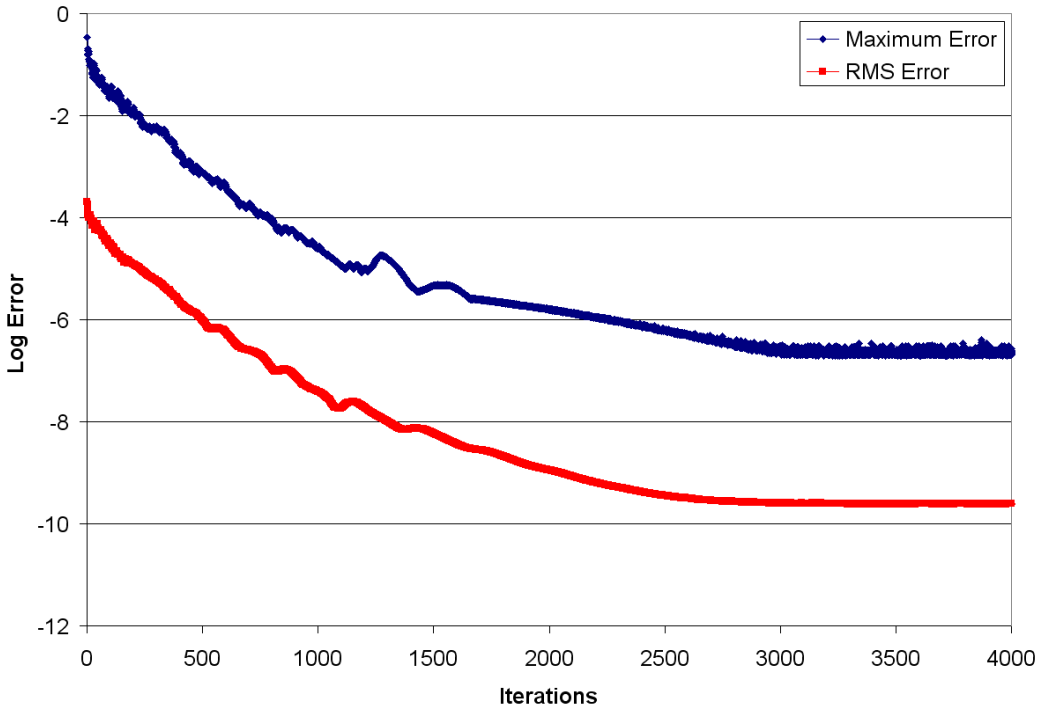

Figure 3.6: Solution Convergence

3.5: Baseline Configuration

This section summarizes the CFD results of the baseline configuration (no flow control). A grid resolution study was conducted to ensure that the mesh was of sufficient resolution to accurately capture the flow solution. For complete details of the grid resolution study, please refer to Appendix C.

3.5.1: External Boundary Layer Characteristics

Modeling the approaching boundary layer is of paramount importance when analyzing a BLI inlet. As mentioned previously, a 30% boundary layer height is desired ($\delta/h = 0.30$). To determine an appropriate boundary layer growth length prior to ingestion, an approach boundary layer with an appropriate velocity profile and skin friction value was modeled using an extended "flat plate" section upstream of the inlet. This is similar to the approach used by Allan.[14,15] The boundary layer thickness growth over this region was calculated (theoretical prediction) using a turbulent flat plate boundary layer growth formulation.[20] This method simulates the boundary layer profile according to the 1/7 power law:

$$\frac{u}{U_e} = \left(\frac{y}{\delta}\right)^{\frac{1}{7}}. \tag{3-4}$$

This assumption results in a fully turbulent profile to predict the flat-plate growth. The desired boundary layer growth length was predicted according to:

$$\delta(x) = 0.375 \cdot x \cdot \mathrm{Re}_x^{1/5}. \tag{3-5}$$

The adverse pressure gradient caused by the ram effect of the inlet also results in a local boundary layer thickening. Thus, the final ingested boundary layer thickness was determined in combination with the ram effect of the inlet capture, resulting in the boundary layer thickness as shown in Figure 3.7. In this figure, the flat-plate prediction (blue) was compared with measurements from ADPAC on both the inlet centerline and at a location outboard of the diffuser (i.e. in the undisturbed freestream flow at the same axial location). It is apparent that the boundary layer growth is accurately predicted up to the point where the pressure gradients imposed by the diffuser ram effects begins to alter the ingested flow.

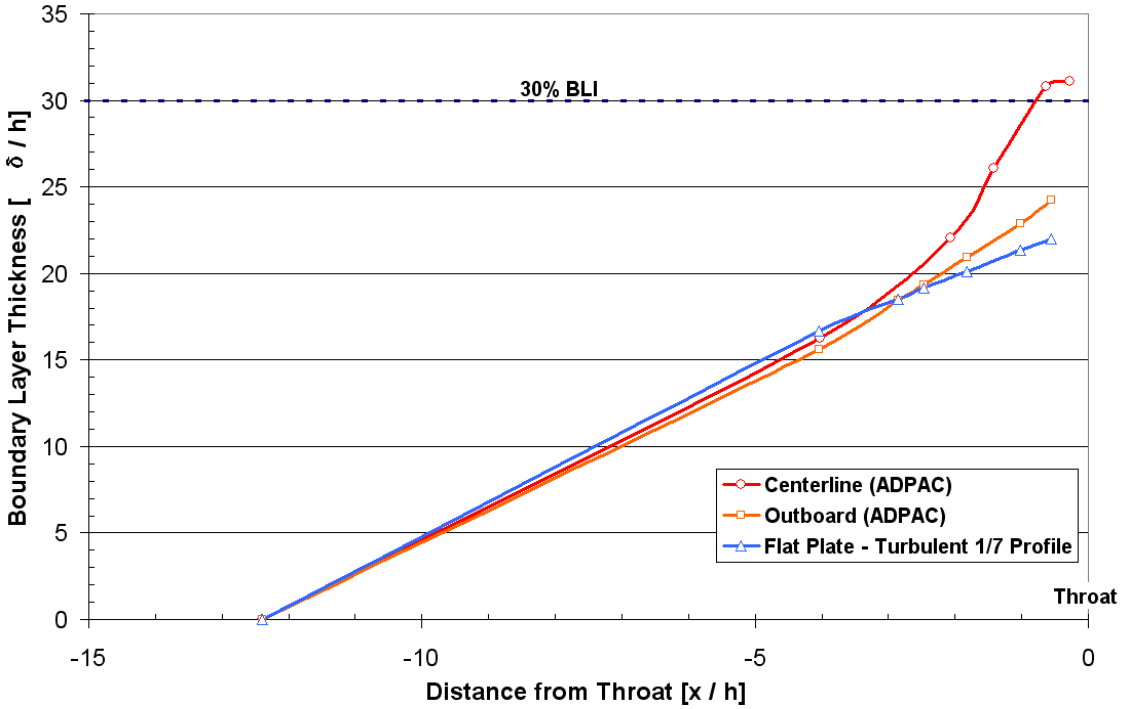

Figure 3.7: Boundary Layer Growth

The resulting velocity profile as measured at one inlet height upstream of the inlet (x/h = -1.0) is shown in comparison with the predicted 1/7 Power profile in Figure 3.8. These profiles were examined to determine the effects of pressure gradients created by engine ram on the boundary layer characteristics at the measurement location, and to ensure boundary layer uniformity between the inboard and outboard mesh blocks. The blue line (lowest) is a profile calculated according to the 1/7 power law, which was used to approximate the required boundary layer growth distance based on 2D turbulent boundary layer estimates. The calculated profile shows higher skin friction versus the "natural growth" baseline profiles which have significantly lower skin friction. At this location the boundary layer thickness was calculated to be $\delta/h \approx 0.29$. Additional boundary layer parameters were calculated to be:

$$\delta = 0.723 \text{ in}$$

$$\delta^* = 0.257 \text{ in}$$

$$\theta = 0.089 \text{ in}$$

$$H = \delta^*/\theta = 2.88$$

$$C_f \approx 0.0002$$

$$Re_\theta \approx 10{,}400$$

The high value for the boundary layer shape factor H (above 2.0) suggests that the flow may be approaching separation, although no reversed flow was seen near the wall. The low estimated skin friction value also indicates incipient separation, and is significantly lower than the skin friction value obtained from the computed 1/7 velocity profile (0.0014). Further computational analysis of thicker approaching boundary layers caused separation with reverse flow along the inlet centerline. Thus, capturing the correct boundary layer physics is of critical importance as the AIP distortion pattern and magnitude appear to be highly sensitive to the ingested boundary layer characteristics. Based upon the obtained profile as shown in Figure 3.8, the boundary appears to be of appropriate thickness and profile to be suitable for modeling this application.

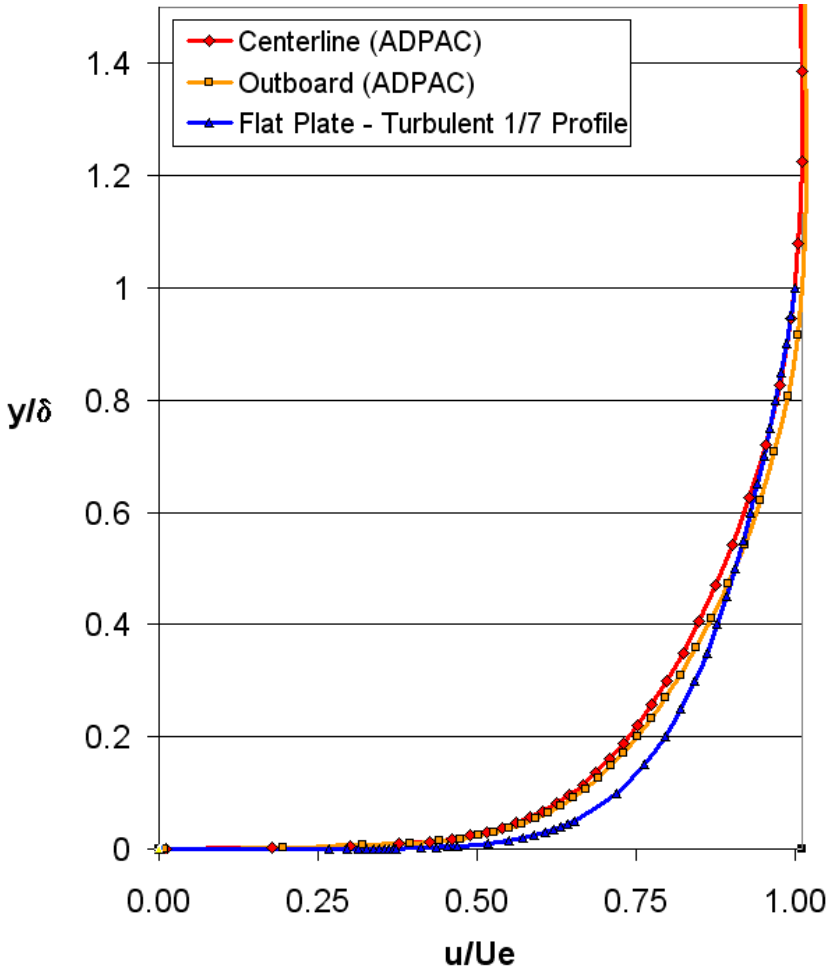

Figure 3.8: Boundary Layer Velocity Profiles (Baseline) at x/h = -1.0

3.5.2: Baseline Solution Results

The results of the baseline configuration (without flow control) will be presented by examining the characteristics of the flow at critical locations, and determining the flow mechanisms that characterize the formation of flow distortion.

An isometric view of the diffuser in Figure 3.9 shows the baseline solution with several normalized total pressure contours shown for constant streamwise cross-sections. These results clearly show the initial boundary layer flow distortion generated at the nacelle entrance, followed by the influence of the circumferential pressure gradients that shape the low momentum boundary layer fluid into a central core of low total pressure fluid.

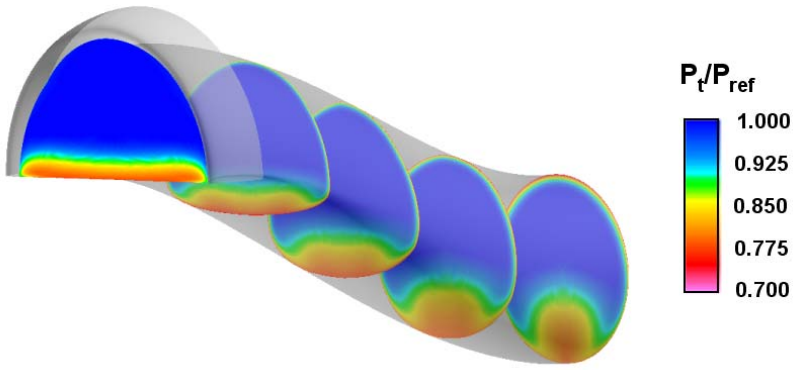

Figure 3.9: Diffuser Total Pressure Contours – Baseline

Surface static pressure contours in the diffuser are shown in Figure 3.10. As noted in section 1.2.1, the turns induce locally higher pressures on the outside of the diffuser creating the secondary flows and large pressure gradients across the diffuser.

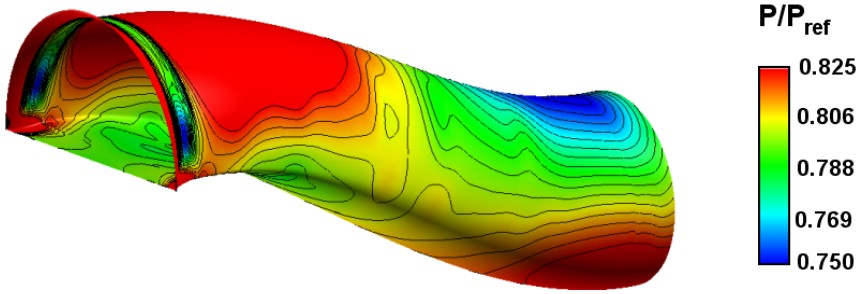

Figure 3.10: Diffuser Wall Static Pressure Contours – Baseline

Figure 3.11 shows non-dimensional velocity magnitude contours along the inlet centerline. A low speed region exists just upstream of the AIP, but this region does not appear to be separated based on boundary layer profiles inspected at the AIP. However, it is apparent that some vortex lift-off has occurred, forming the distinctive distortion pattern at the AIP. Studies examining higher inlet mass flows do not show as strong a buildup of low speed fluid ahead of the inlet throat, as discussed in Appendix D. Another distinctive flow characteristic is the formation of a "supervelocity" region just upstream of the inlet throat. This velocity profile is the result of interaction between the ingested boundary layer flow, the potential field effects of the diffuser lip, and the required engine mass flow. Also evident is a local thickening of the ingested boundary layer resulting from the adverse pressure gradient created by engine ram effects.

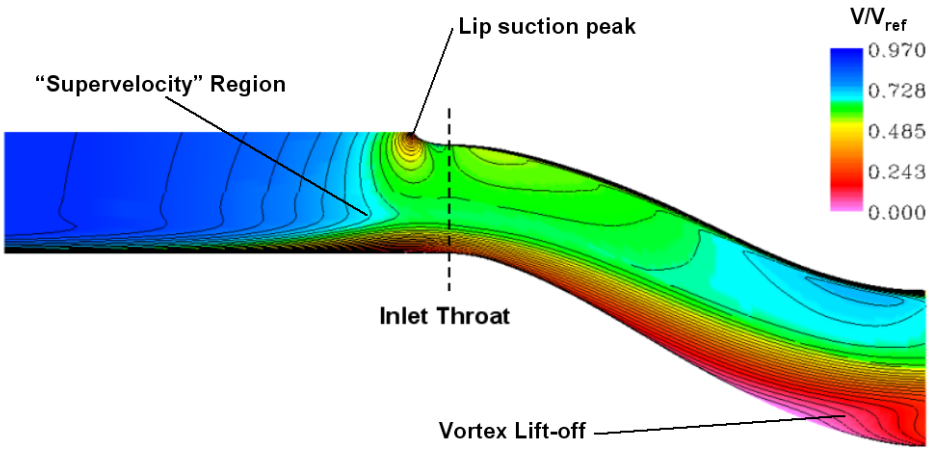

Figure 3.11: Centerline Velocity Contours – Baseline

The computed velocity contour plots for the baseline flow can be compared to data obtained by NASA for the configuration 'A' inlet geometry; it should be noted however, that NASA investigations used a freestream Mach = 0.83, while Techsburg used a freestream Mach = 0.85 (defined by contract). Figure 3.12 compares the baseline (no flow control) centerline Mach contours computed at Techsburg to those by Berrier et al.[15] They used an overset grid topology to examine the flow using a modified Menter Shear Stress Transport (SST) turbulence model. Despite these differences, it can be seen that the Mach contours compare favorably with the results obtained for the baseline solution. The contours show that the average Mach number of the inlet flow remains relatively unchanged in the upper half of the inlet; this is due to the small diffusion ratio (A_{AIP}/A_{Throat} = 1.069) of the inlet. Target Mach numbers for the inlet and AIP (0.7 and 0.55, respectively) are achieved through mass averaging at the location face. The fluid buildup upstream of the AIP and flow super-velocity region are clearly visible in both solutions.

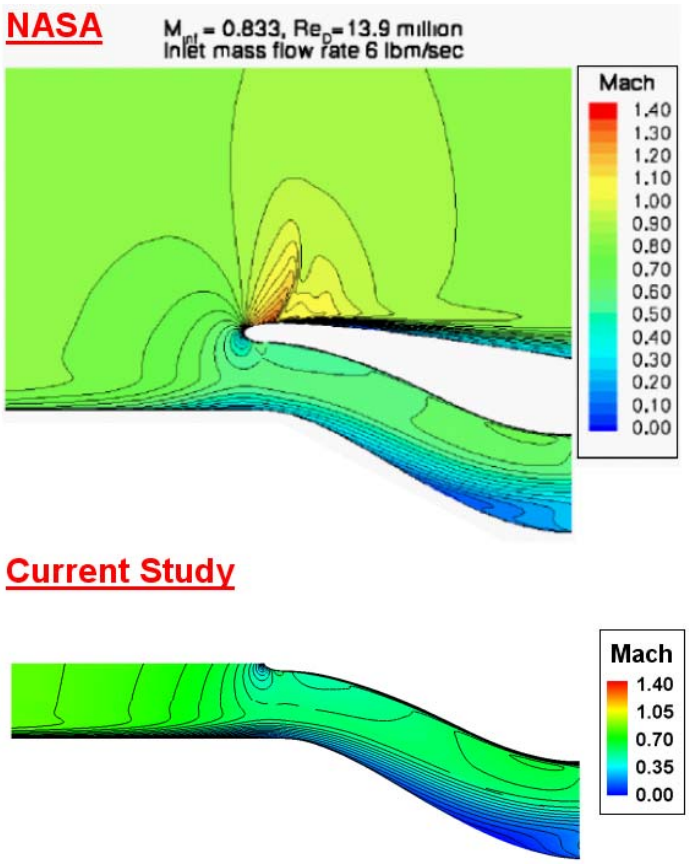

Figure 3.12: Comparison Baseline Mach Contours

Shown in Figure 3.13 are the total pressure contour results at the AIP, as well as the DC(60), DPCPavg, and total pressure recovery numbers for the baseline flow solution. The total pressure contours from the current study compare well qualitatively to NASA results for the same geometry also shown in Figure 3.13. It is evident that the flow mechanism present at the AIP is the same for the two cases, although the flow Mach number and modeled vortex behavior are somewhat different. This difference is likely the result of different turbulence models used in the analyses. The NASA solution used the Menter Shear Stress Transport turbulence model in their analysis, while Techsburg used the Spalart-Allmaras turbulence model. NASA's Allan noted that vortices embedded in boundary layers behave differently between these two models[21], and thus would not model the flow identically. In particular, the strength of modeled vortices was different particularly in the vortex core, this difference then directly impacts the predicted distortion.

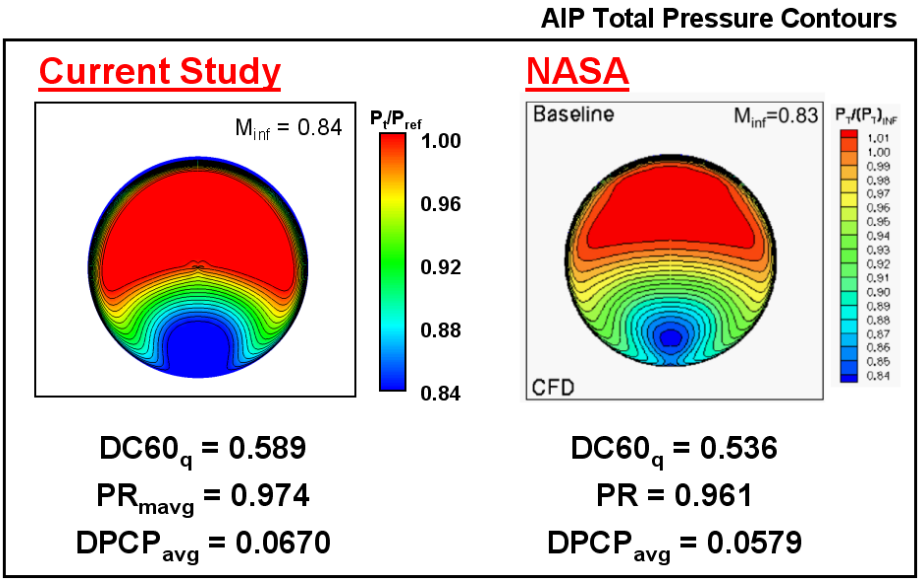

Figure 3.13: AIP Total Pressure Contours – Baseline BLI

3.5.3: Baseline Flow Swirl

The results obtained from the baseline solution as characterized by the SC(60) swirl parameter are presented in Figure 3.14, which shows the secondary flows in terms of streamwise vorticity. It is clear that the region of highest cross-flow velocity is located at the base of the duct. In this location the flow is characterized by two large counter-rotating vortices as shown by the secondary flow velocity vectors in Figure 3.14. Additional vorticity is also present around the periphery of the duct as a result of the boundary layer movement.

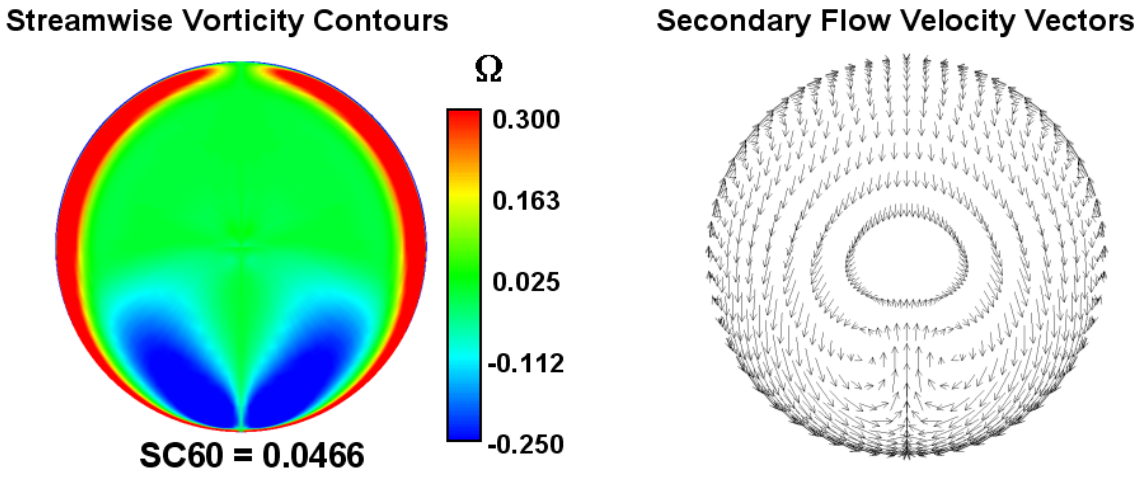

Figure 3.14: Baseline AIP Streamwise Vorticity Contours and Secondary Flow Velocity Vectors

3.5.4: Baseline Flow Distortion Mechanisms

For this inlet flow and diffuser geometry there are three distortion mechanisms at work:

1) Nacelle junction vortex
2) Circumferential pressure gradients created by offset
3) Ingested boundary layer

The junction vortex is the result of interaction between streamwise vorticity present within the boundary layer flow as it interacts with the geometry of the junction between the nacelle lip and the bottom of the diffuser or "floor" surface. The circumferential pressure gradients create secondary flows within the diffuser due to differences in flow momentum as it is forced to turn through the serpentine diffuser (as noted in section 1.2.1). The ingestion of a large boundary layer serves to enhance the effects of both of the previous mechanisms.

The combined effects of these mechanisms are shown in Figure 3.15. The boundary layer fluid at the nacelle entrance is pushed toward the center of the inlet by the ingested junction vortex legs, which have the same sense of rotation as the diffuser secondary flows. The induced rotation is highlighted by the streamlines in Figure 3.16. Once inside the diffuser, the existing circumferential pressure gradients establish the secondary flows, resulting in the low momentum boundary layer fluid collecting near the bottom of the inlet in a "tongue" or "mushroom" shaped distortion pattern.

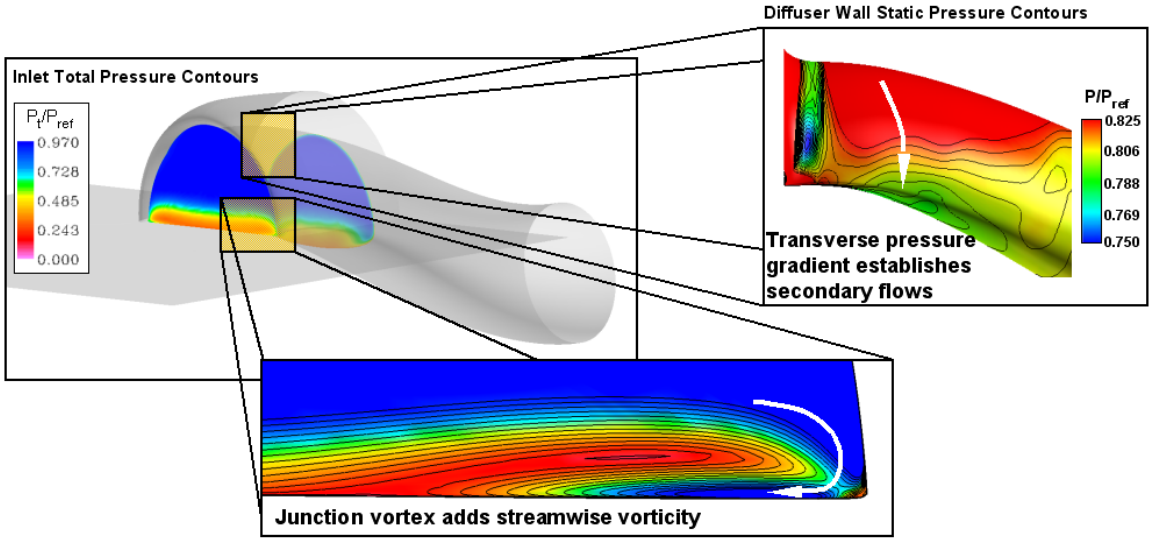

Figure 3.15: Flow distortion mechanisms

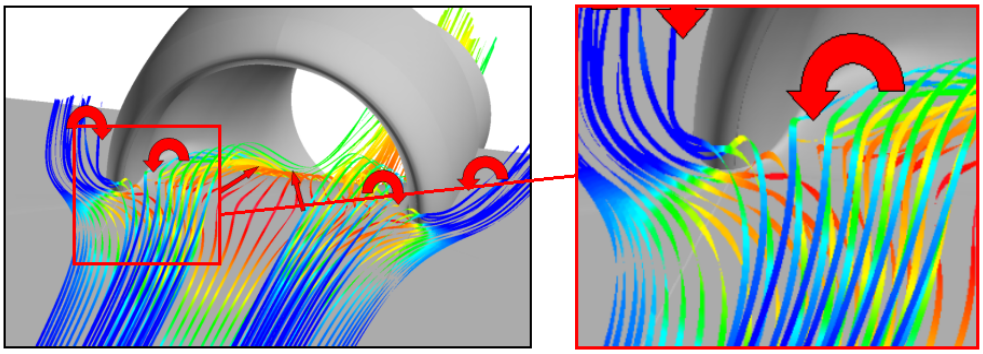

Figure 3.16: Streamlines Depicting Horseshoe/Junction Vortices

3.6: Flow Control Design Strategy

Flow control design strategies were based upon achieving a strong understanding of the driving parameters of engine face distortion. Some elements of the flow control design (i.e. jet orientation) were based on the body of previous work for serpentine inlet flow control[10,13], as well as previous experience at Techsburg.

To investigate the effectiveness of an ejector-pump based flow control device, flow control implementation was limited to combinations of suction and blowing. To make use of the existing pressure field and maximize ejector performance, suction was primarily employed in regions of high static pressure, while blowing was employed in regions of lower static pressure. To prevent secondary flows from forming, the effectors were placed slightly downstream of the duct throat. This utilized a prevention methodology as opposed to attempting to cure distortion after it has formed. Figure 3.17 shows the optimal locations for flow control based on these criteria. The left image in Figure 3.17 shows contours of pressure coefficient Cp and correspondingly locates the areas of high local static pressure suitable for the location of suction. The right image in Figure 3.17 shows diffuser surface static pressure contours and graphically depicts the optimum flow control jet location.

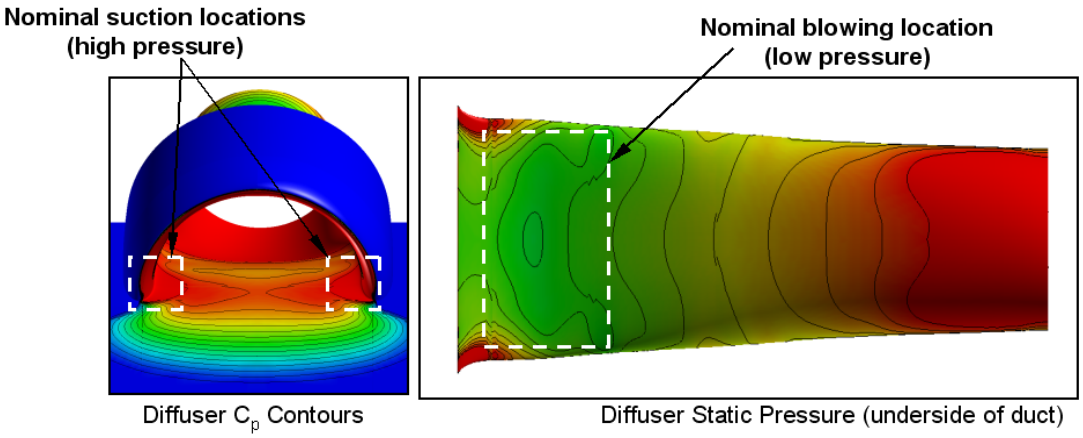

Figure 3.17: Flow Effector Location Rationale

The blowing jet orientation used for all jets in this study was based on the work of Anderson[22] and Gorton[13]. The jets were configured to have a circumferential blowing angle of 30° from the local surface tangent (blowing outward from the centerline in all cases) with a streamwise angle of 90°. Thus, the jets were blowing perpendicular to diffuser axial direction, thereby adding no momentum in streamwise direction. In this orientation, as depicted in Figure 3.18, all the jet momentum is used to directly manage the secondary flow.

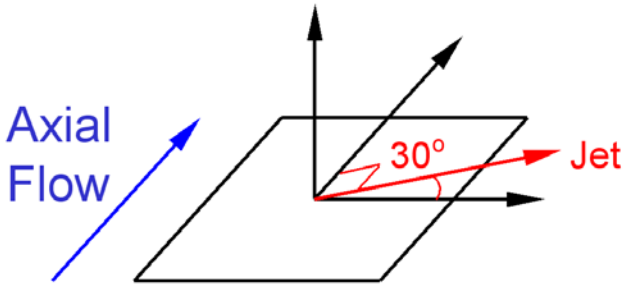

Figure 3.18: Nominal blowing jet configuration

Previous studies have examined the use of vane-type vortex generators with the goal of preventing separation or maximizing diffuser total pressure recovery. However, studies by Anderson et al.[22] have shown that using effectors to manage flow separation does not necessarily result in the minimum flow distortion at the fan face. By using fluidic actuators to directly manage the diffuser secondary flow, the distortion can be directly managed.

3.7: Blowing Configurations

Blowing investigations covered a wide variety of parameters and geometries. To evaluate ejector-based performance vs. conventional blowing, two nominal mass flow rates of 1% and 2% of the inlet mass flow were examined. Cases that used 1% blowing were used to simulate the use of engine bleed for a conventional blowing scenario. The 2% blowing case would be used in combination with a 1% suction to simulate ejector-pump performance.

Different types of jet arrangements were investigated in order to determine key factors leading towards an optimum jet configuration. The general blowing schemes of Figure 3.19 - Figure 3.22 were labeled: Circumferential, Axial, Pyramid, and Reverse Pyramid In all cases, the jet placement began at x/L = 0.067, where 'L' represents the total duct length. The circumferential scheme placed all jets at this axial location whereas the following schemes placed only the most forward jet at this station, with successive jets being placed at a distance farther down the diffuser. (Complete details of jet locations shown in Appendix L) The initial axial location for the jets was based upon research which showed that losses in jet performance and effectiveness at upstream locations was far less than the penalty of jets being located too close to flow disturbances.[9] This upstream location also coincided with an area of lower static pressure, which is useful in optimizing ejector pump performance due to the necessity for a lower required motive pressure.

As noted by Gorton, for an array of blowing jets there will be distinct blowing jet combinations that are optimal for the control of distortion, especially when seeking to minimize mass flow requirements.[13] Thus, a variety of different configurations were examined.

3.7.1: Circumferential Blowing

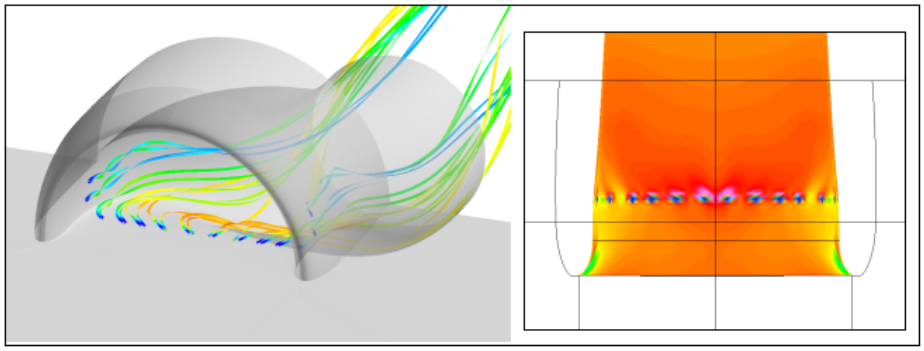

Figure 3.19: Circumferential Blowing

For the circumferential blowing configuration, the jets are spaced around the perimeter of the diffuser at a constant axial location. Ten Jets are located along the diffuser "floor", and two on each sidewall (14 total). The goal of this configuration is to spread the low momentum fluid from the near wall region around the periphery of the duct, while maintaining separation between the vortices created by the jets.

3.7.2: Axial Blowing

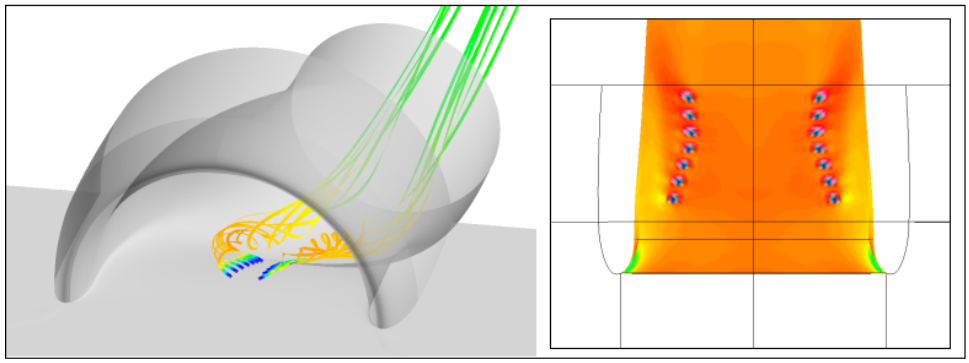

Figure 3.20: Axial Blowing (Axial 1 (left), Axial 2 (right))

For the axial blowing configuration, the jets are located in a streamwise row, extending down the axial duct length. The goal is to continually spread the low momentum fluid from the center of the diffuser towards the outside of the duct. Two configurations were tested, one with the jets located near the outside of the diffuser Axial 2), and the other with the jets located near the center of the diffuser (Axial 1).

3.7.3: Pyramid Blowing

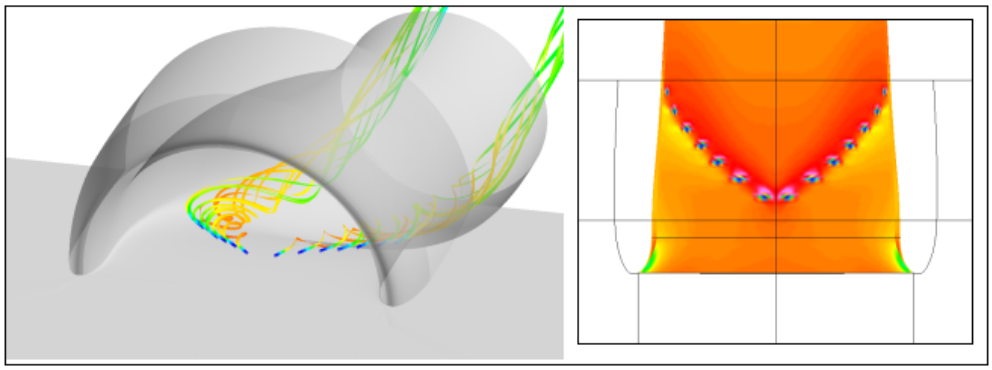

Figure 3.21: Pyramid Blowing (Pyramid 1)

This configuration aims to continually manage the vortex induced by the jets by providing a more constant "push" to the secondary flows while traveling up the diffuser sidewalls. Different jet configurations were tested by progressing through a series of array skew angles. (Pyramid 1, Pyramid 2, Pyramid 3, Pyramid 4). Figure 3.21 shows the Pyramid 1 configuration.

3.7.4: Reverse Pyramid Blowing

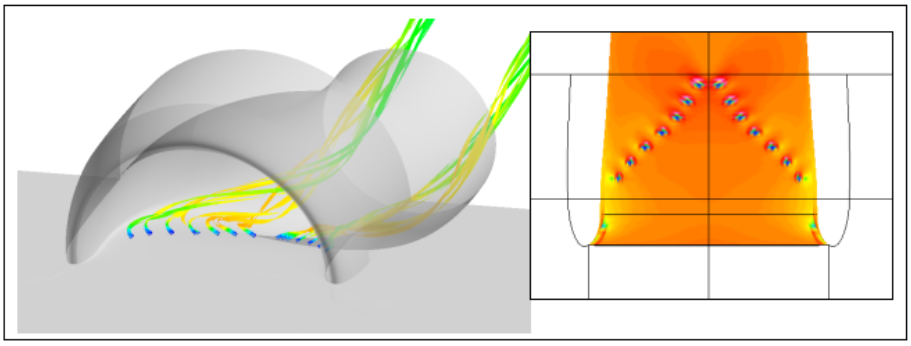

Figure 3.22: Reverse Pyramid blowing

Because the regular Pyramid often results in an additive effect creating a single large vortex on each side of the diffuser, the orientation of the jets was reversed so that the jets acted independently. This configuration aims to continually spread the low momentum fluid around the diffuser, while maintaining jet individuality. The configuration shown in Figure 3.22 was the only reverse pyramid scheme tested.

3.8: Suction Configurations

Suction investigations focused on two different configurations – suction at the inside corner of the nacelle lip, and across the inlet entrance as shown in Figure 3.23. The desired location of the suction was determined from the floor pressure distribution. The nominal suction mass flow rate was set to 1% to simulate ejector performance. The pressure specified for the inflow boundary conditions was held constant in order to simulate a constant suction pressure. Thus, mass flow rates throughout the suction system are not necessarily uniform due to differences in flow conditions outside the suction ports.

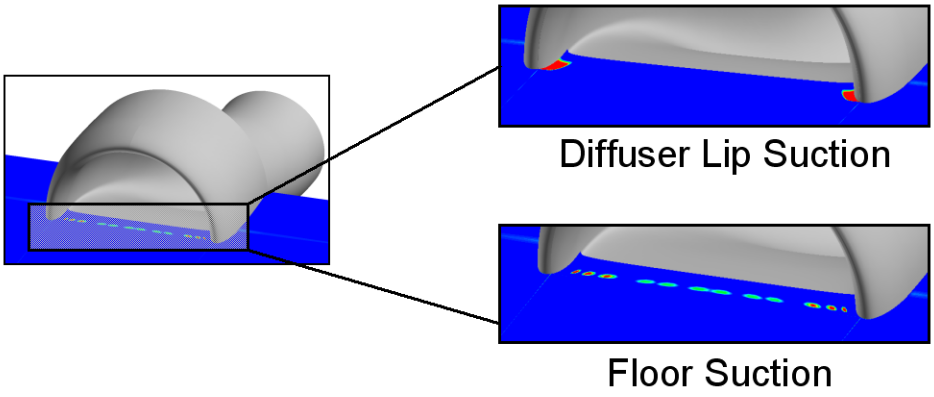

Figure 3.23: Lip and Floor Suction

The locations for the flow suction were placed based upon two basic concepts. The first approach examined the placement of suction near the inside of the diffuser inlet lip. This is an area of high pressure as it is the location of the flow stagnation streamline. As the ejector pump's performance is increased when taking advantage of existing pressure gradients, this would seem to be a promising location. In addition, there is an added benefit of ingesting part of the junction vortex which forms around the lip due to boundary layer flow interactions. This flow structure is believed to be contributing strength to the existing pressure gradients within the diffuser, in particular, reinforcing the secondary flow pattern that leads to a high flow distortion. The second configuration investigation focused on ingesting the low momentum fluid near the wall as the flow entered the duct. In this setup, the low momentum fluid along the "floor" of the diffuser is ingested. Additional benefit arises from the placement of the suction as it nicely complements the ejector pump setup, having the suction source closer to the jets. This

reduction in distance can influence ejector pump efficiency by reducing the fluidic losses as the ingested fluid moves through the pump tubing.

3.9: Modeling the Ejector Pump

3.9.1: Ejector Pump Implementation Considerations

One of the considerations for the blowing and suction configurations described to this point is their compatibility with the implementation of an ejector-pump based fluidic actuator. To implement a scheme similar to that shown in Figure 2.1, the suction and blowing locations should be relatively close together, with some space available for internal ducting to facilitate an efficient design with low frictional losses. Also, as mentioned previously, a favorable pressure gradient will help the ejector's suction to motive flow ratio to increase. All of the simulated ejector models examined meet these criteria.

3.9.2: Blowing and Suction Configuration Selection

To select the combination of suction and blowing cases for simulating the ejector pump, the most effective blowing configurations for the four blowing types (circumferential, axial, Pyramid, or reverse Pyramid) were combined and run with both of the suction types. These combinations are shown in Figure 3.24, with a representative sample of the cases shown in Figure 3.25.

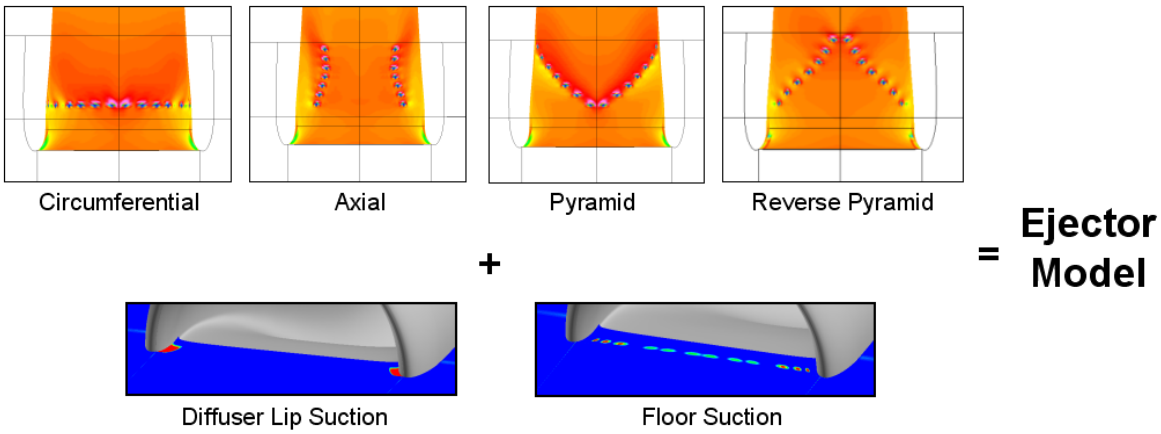

Figure 3.24: Cases Modeled Using Ejector Pump

It should be noted that when comparing the simulated ejector model versus the conventional blowing cases, the jet velocity ratio was maintained with the same supply pressure, while the hole area was reduced. This worked to decrease the blowing jet mass by 50%, while keeping the velocity ratio constant compared to the ejector pump cases.

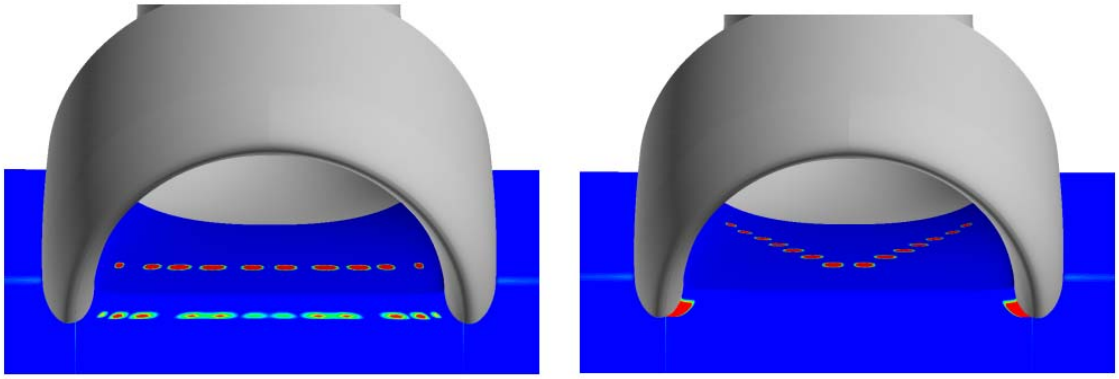

Figure 3.25: Sample Ejector Pump Models

Flow Control Results Summary

The flow control results for the most promising flow control cases are shown in Figure 3.29-Figure 3.30. The cases examined will compare the simulated ejector pump model to a "conventional" blowing scheme. As previously discussed, the simulated ejector pumps will utilize 2% of the total AIP mass flow for blowing and 1% AIP mass to simulate the ejector suction. The "conventional" blowing cases will utilize 1% AIP mass for blowing with no suction. These cases will be compared to the baseline (no flow control) solution, and will be denoted:

- **Baseline:** Baseline Solution - no flow control
- **Cir (1%):** Circumferential Blowing Scheme (Conventional)
- **Pyr1 (1%):** Pyramid 1 Blowing Scheme (Conventional)
- **FSCIR:** Floor suction combined with circumferential blowing scheme (Simulated ejector pump)
- **SP1:** Lip Suction combined with Pyramid 1 blowing scheme (Simulated ejector pump)

A complete description of all investigated flow control cases and their distortion values are discussed in Appendix G.

3.9.3: *Flow Control Results*

The flow is analyzed at the AIP for distortion using the descriptive parameters described in earlier sections.

The DC(60)pt distortion parameter examines the 'worst' (i.e. lowest total pressure) 60º sector of the flow non-dimensionalized by the average AIP total pressure. In addition to the DC(60)pt results, Figure 3.26 also presents the AIP total pressure contours to serve as a visual aid in showing the effects of the flow control. The DC(60)pt parameter yields a baseline value of approximately 0.12. As shown, all flow control scenarios examined reduced the total pressure distortion according to the DC(60)pt criterion. The conventional blowing scenarios (1% AIP total mass) were both successful in reducing the distortion, with the Pyramid 1 configuration yielding a 23% reduction, and the circumferential case yielding a 18% reduction. Significant improvement was achieved over and above these results when adopting the simulated ejector pump model. The Pyramid and lip suction model (SP1) achieved the largest reduction in total pressure distortion by reducing it 55% below baseline distortion levels. The circumferential case also achieved a significant reduction in decreasing AIP distortion by 50% below baseline. Visual contours suggest that the boundary layer fluid has been successfully redistributed. (Further examination of pressure contours are discussed in a later section.)

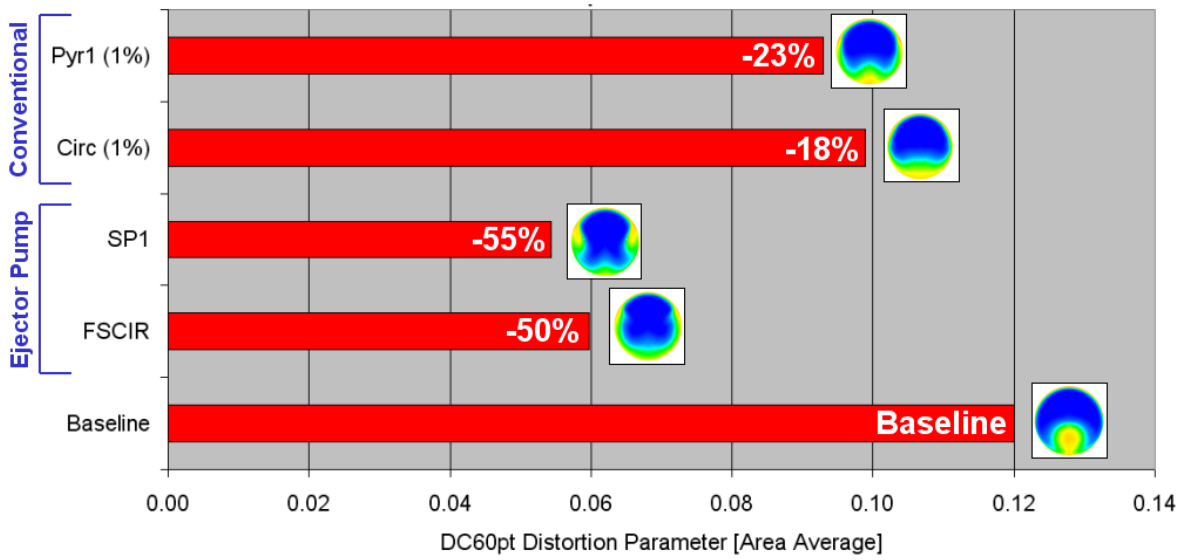

Figure 3.26: DC(60)pt Distortion Parameter Results

The distortion results of Figure 3.27 are quantified by the DC(60)q parameter, which non-dimensionalizes the total pressure distortion using the average dynamic pressure at the AIP, yielding a parameter that examines an average deficit of flow energy. This parameter shows the same trends as those obtained using the DC(60)pt parameter. However, this parameter indicates a maximum reduction in distortion of 75% for the SP1 case (DC(60)q = 0.157). Similar to the DC(60)pt metric, this parameter indicates a larger benefit in using the simulated ejector pump model. This difference is likely the result of the higher velocities associated with the formation of large vortices, which are more prevalent in the stronger flow control efforts. It should be noted that none of the tested models achieved the 'acceptable' distortion level of DC(60)q = 0.10. However, these systems were not optimized and additional work could likely yield a configuration that achieved the desired level of performance.

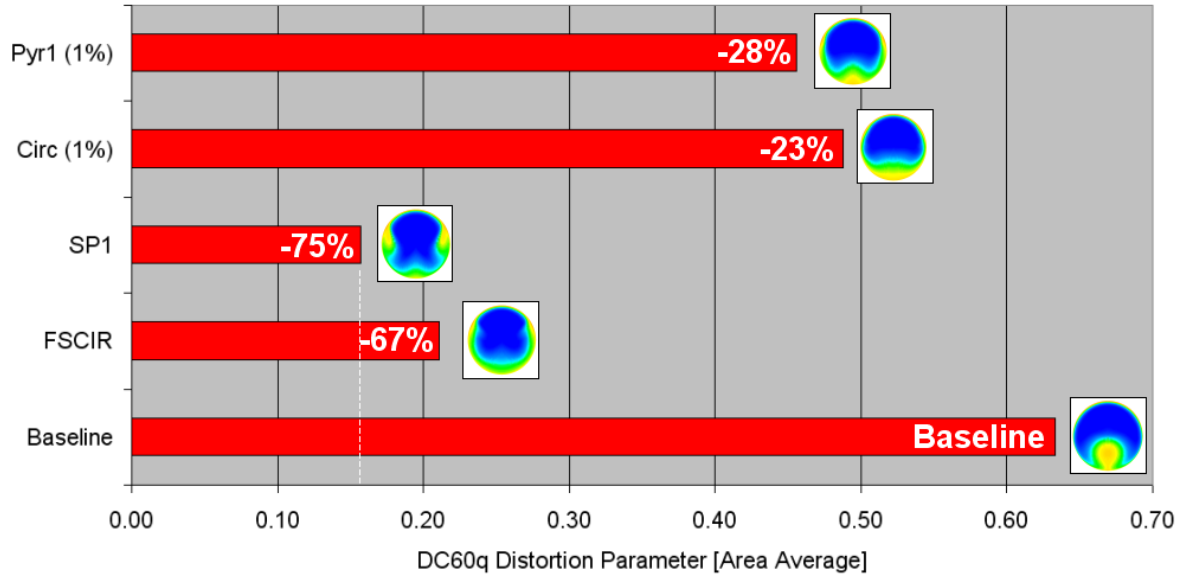

Figure 3.27: DC(60)q Distortion Parameter Results

The SAE distortion descriptor DPCPavg varies slightly in its perception of flow distortion at the AIP, as shown in Figure 3.28. In contrast to the DC(60) descriptors, the DPCPavg parameter reflects an average circumferential distortion for the whole AIP, as opposed to representing only the worst 60º sector of the flow. This parameter combines the circumferential distortions for each ring of the distortion rake and averages the individual results to serve as a more "global" descriptor. (Discussed in detail in Appendix

A) Although the distortion is significantly reduced by all flow control schemes, the circumferential ejector configuration is quantified as being more effective than the Pyramid 1 ejector configuration. The maximum reduction in distortion is achieved by the floor suction and circumferential (FSCIR) scheme in yielding a 71% reduction. The control mechanism shown by the total pressure contours suggests that although the circumferential ejector model does not have the 'best' 60° sectors, the distortion is more evenly distributed around the periphery of the duct. This result is consistent with the visual pressure contours shown. These results also suggest that the lowest distortion is achieved by the configurations in which the individual jets do not coalesce into a single vortex. The circumferential configuration has this feature, in contrast to the Pyramid 1 scheme that continually reinforces a single vortex that sweeps up the sides of the diffuser.

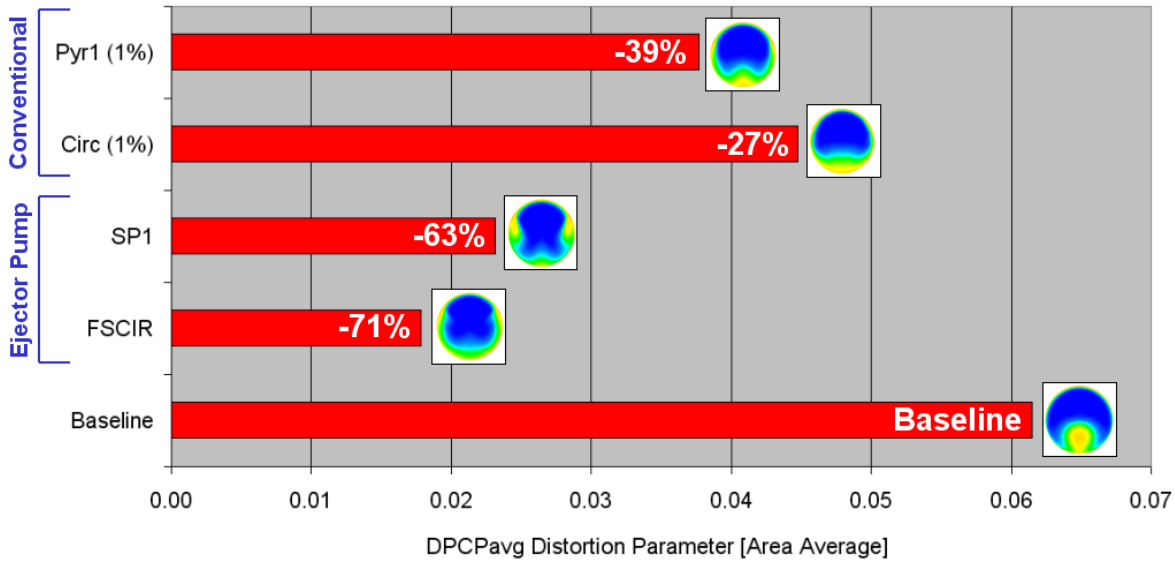

Figure 3.28: DPCPavg Distortion Parameter Results

Results from investigations using the SC(60) swirl parameter examine the relative strength of the secondary flow structures at the AIP. Values shown in Figure 3.29 represent the overall effectiveness of the flow control system to successfully counteract the formation of secondary flows within the diffuser and thus provide quality flow to the compressor. As can be seen, the circumferential schemes are by far the most effective in reducing swirl at the AIP. Due to the large-scale vortices created by the Pyramid blowing schemes, AIP swirl for Pyramid configurations is actually increased by a maximum of 64% over baseline swirl. These results again suggest that distortion is most effectively

managed with jets that do no coalesce into a single large vortex, but rather maintain their own scale and remain within the bounds of the low-momentum fluid.

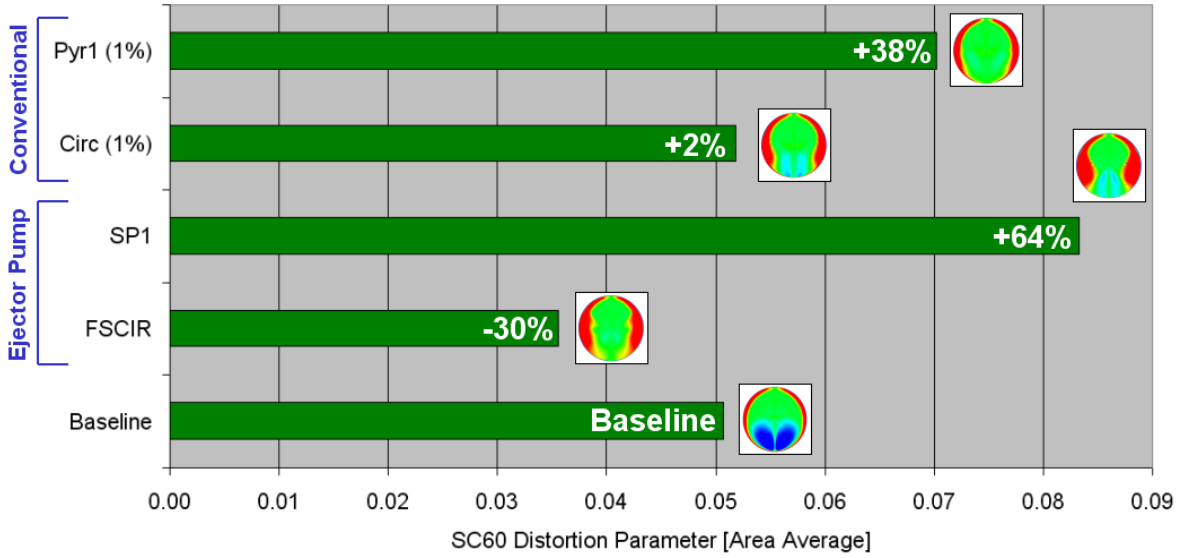

Figure 3.29: SC(60) Swirl Parameter Results with Streamwise Vorticity Contours

Investigations into the effect of flow control on diffuser total pressure recovery have shown that there is little to no benefit obtained by using fluidic actuators inside the diffuser. This is not particularly surprising since the goal of the flow control is merely to redistribute the low-momentum fluid to create a more uniform flow at the AIP. It should be noted however, that these minor effects are likely to be small in comparison to the losses typical of the large vane generators needed for high boundary layer ingestion.[12]

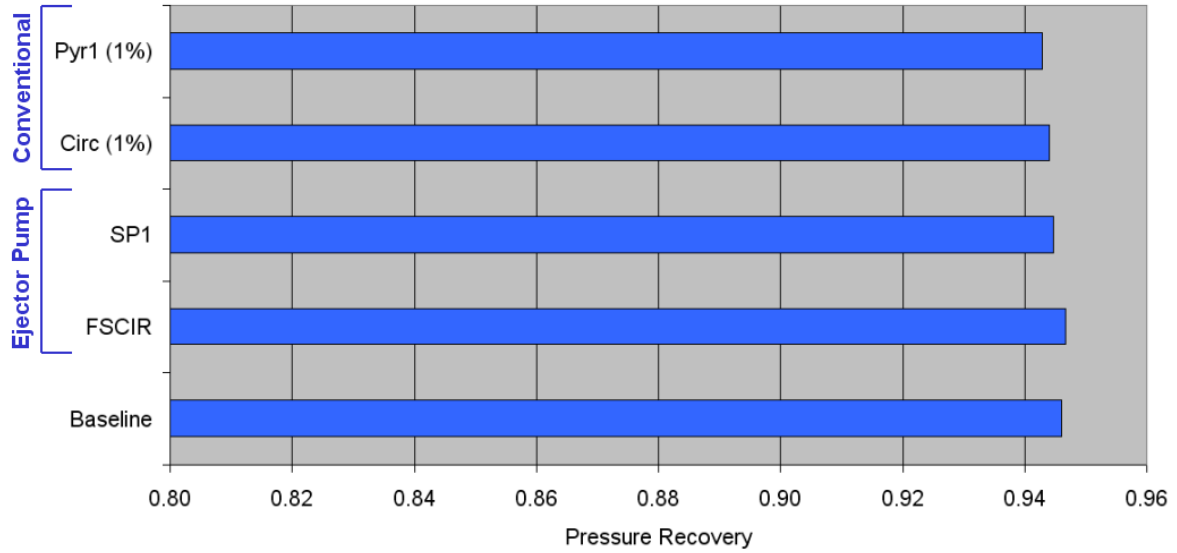

Figure 3.30: Total Pressure Recovery Results

The complete results for the ARP-1420 circumferential and radial distortion intensity descriptors are shown in Appendix G..

3.10: Flow Control Visualization/Summary

Further examination of the total pressure and vorticity contours of the flow control results at the AIP, allows for better understanding of how the flow control has affected the flow distortion. Examining a few of the best ejector-based flow control results and comparing them to a conventional blowing scheme of the same type can yield an understanding of the primary mechanisms that are the most productive in flow control. The schemes that will be examined in detail will be the floor suction and circumferential blowing (FSCIR), lip suction and Pyramid 1 blowing (SP1), and the comparative conventional blowing schemes Circumferential and Pyramid 1. These results will all be compared relative to the baseline case (no flow control). The total pressure contours of the aforementioned cases are shown in Figure 3.31, and their respective distortion values are listed in Table 1. For a complete listing of flow control results, refer to Appendix G.

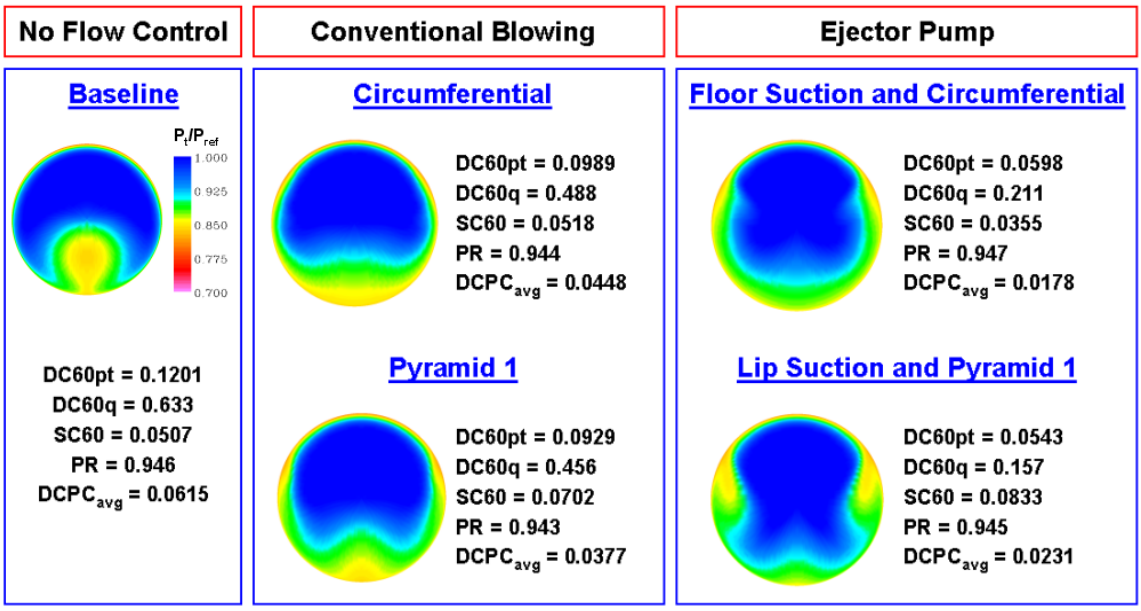

Figure 3.31: Conventional Blowing and Ejector Pump Total Pressure Contour Comparison

Table 1: Comparison of distortion reduction parameters for select cases.

Distortion Parameter	Distortion Parameter Value [% reduction from baseline]				
	Baseline	Circumfer.	**FSCIR**	Pyramid 1	**SP1**
DC(60)q	0.633	0.488 [23%]	**0.211 [67%]**	0.456 [28%]	**0.157 [75%]**
DC(60)pt	0.120	0.099 [18%]	**0.060 [50%]**	0.093 [23%]	**0.054 [55%]**
DPCPavg	0.062	0.045 [27%]	**0.018 [71%]**	0.038 [39%]	**0.023 [63%]**

The total pressure contours in Figure 3.31 clearly indicate the large effect flow control has had on the AIP distortion. The baseline configuration clearly shows a large region of low total pressure fluid in the lower portion of the AIP collected by the strong secondary flows within the diffuser. In first examining the total pressure contours for the conventional blowing cases (total jet mass equal to 1% of the mass through the AIP), it is evident that a large change in total pressure distortion has occurred. In both cases, the jets have significantly reduced the distortion at the AIP. As indicated in Table 1, the conventional circumferential blowing scheme reduced the DC(60)q distortion by 23% as compared to the baseline (no flow control) solution, and the Pyramid 1 configuration reduced the DC(60)q distortion by 28%. The contours displayed in Figure 3.31 show a redistribution of the low total pressure fluid around the periphery of the diffuser, with some residual areas of low total pressure fluid, particularly at the bottom of the AIP. As this is the original location for the "pooling" of the flow, it appears that the jets are not quite effective enough to counteract the formation of strong secondary flows within the diffuser. By implementing a simulated ejector-based series of fluidic actuators, the relative strength of the flow control jets was increased by providing additional mass flow (and hence momentum addition) in combination with some boundary layer suction.

The simulated ejector pump based flow control jets produced a significant improvement in the reduction of total pressure at the AIP as compared with the conventional blowing only scheme. As compared to the baseline configuration, the DC(60)q distortion parameter was reduced by 67% and 75% in the FSCIR and SP1 configurations respectively, almost reaching the operation DC(60)q of 0.10. It should be noted that the simulated ejector-based actuators obtained this further reduction with no additional increase in motive jet air, and thus had the same jet supply requirements. By

examining the total pressure contours it is clear that the low-momentum fluid from the ingested boundary layer, along with the low momentum fluid from boundary layer growth on the diffuser have been effectively redistributed away from the lower section of the AIP. Although the ejector-based circumferential case (FSCIR) has higher DC(60) distortion parameters than the Pyramid 1 ejector case (SP1), the DPCPavg calculation indicates that the average distortion in the FSCIR case is lower. This would seem to coincide with the visually more evenly distributed contours of the FSCIR case. The difference shown by the two DC(60) parameters indicates that in the "worst" 60-degree sector of the flow the SP1 case locally has a lower maximum distortion. Thus, although the parameters indicate that the SP1 case has a lower distortion in some cases, it is clear that some sensible qualification of these results must be examined at all times. There are, of course, many more types of flow distortion descriptors currently in use in both industry and academia, but they are in most cases much more complicated, and engine specific. However, by examining total pressure distortions in combination with local values of streamwise vorticity at the AIP, one can easily interpret the nuances of the flow distortions.

The secondary flow contours in Figure 3.32 show the solutions that have been examined in detail, and help to highlight the flow characteristics at the AIP. These flow patterns aid in discerning how the fluidic effectors have altered the secondary flows within the diffuser, which have been identified as one of the primary sources of engine-face flow distortion. In order to quantify the severity of the secondary flow, the flow contours can be correlated to the SC(60) swirl parameter. As noted previously, the baseline flow is characterized by two large counter-rotating vortices at the base of the AIP, with a SC(60) value of 0.0507. When examining the AIP secondary flow contours, the conventional blowing cases show a clear effect on secondary flow. These cases both show a net increase in flow swirl, although the circumferential case is almost at the same SC(60) value as the baseline. The simulated ejector pump cases also show a substantial change in the AIP secondary flow structure, and have eliminated the vortices created in the baseline flow. However, only the circumferential ejector case has reduced swirl below its original level. This decrease correlates well with the visual contours that suggest a symmetric distribution of secondary flows around the AIP.

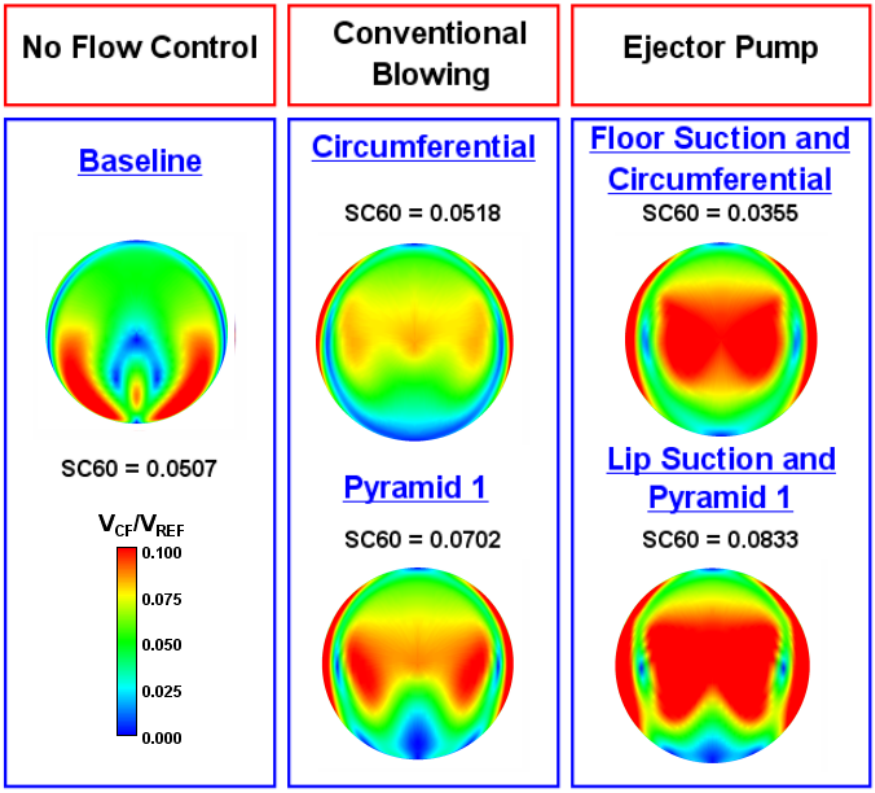

Figure 3.32: Streamwise Vorticity Contours

While both effective, the results for the circumferential blowing and Pyramid blowing cases at the AIP are quite different. In an attempt to better understand the dynamics of the flow for these cases, Figure 3.33 shows flow tracers used to track the fluid trajectories. Important elements to note are:

- The majority of the fluid in the distortion lobe at the AIP comes from the ingested boundary layer flow. This low-momentum fluid is collected into the center by the pressure gradients and resulting secondary flow.
- The spanwise spacing and relative location of the jets is important, and could be optimized with increased understanding of the flow physics. While the jets in the Pyramid 1 scheme are effective, they could be more effective if they were not located such that all streams coalesce into a single vortex. Predominantly spacing the jets spanwise as opposed to axially seemed to produce "better" AIP flow patterns (but not necessarily lower DC(60) results).

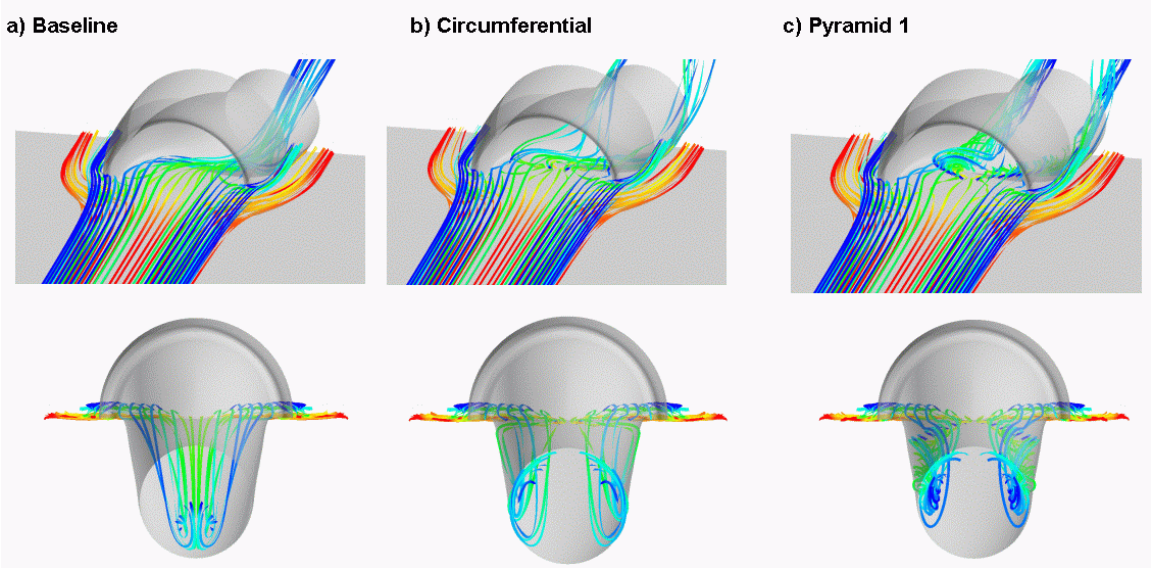

Figure 3.33: Boundary Layer Streamlines

Cross-examining the ingested boundary layer streamlines with the streamlines coming from the flow control jets also highlights the mechanisms in which the flow control was most effective.

The circumferential ejector case FSCIR is depicted in Figure 3.34. In this case, the individual jets remain distinct and separate throughout most of the diffuser, and are effective in "smearing" the low-momentum fluid around the periphery of the diffuser. This is apparent when examining the total pressure contours at the AIP (Figure 3.34 - far right).

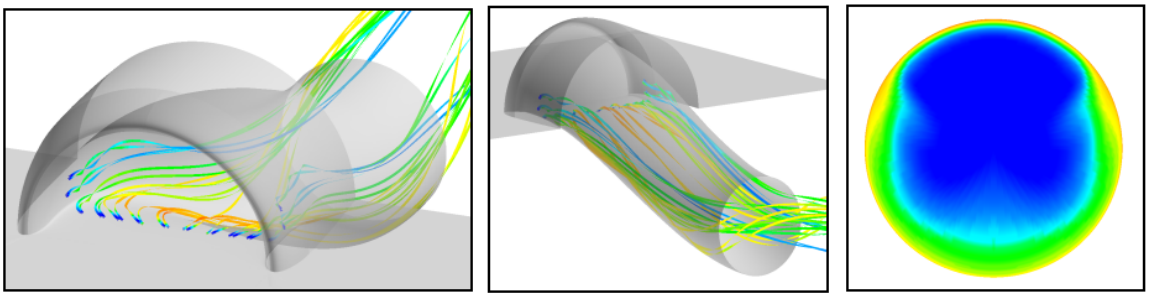

Figure 3.34: Jet Flow Streamlines – Circumferential Ejector (FSCIR)

Flow tracers for the Pyramid 1 ejector case SP1 are shown in Figure 3.35. Here it is apparent that the jets are located such that they coalesce into two counter-rotating vortices that "roll" up the sides of the diffuser, redistributing the low-momentum fluid along the way. When examining the AIP total pressure contours, (Figure 3.35 - far right)

it is clear that although the DC(60) parameter indicates a lower total pressure distortion, the flow appears to be less uniform in its appearance due to the presence of these vortices.

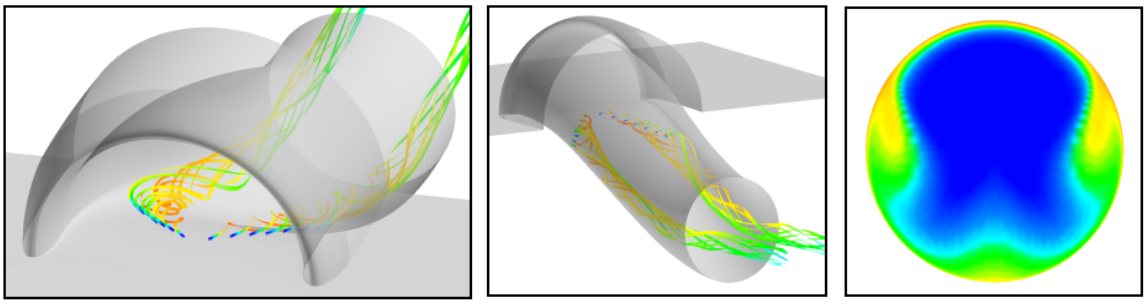

Figure 3.35: Jet Flow Streamlines - Pyramid 1 Ejector (SP1)

In summary, it is apparent that the reduction of total pressure by the current method suggests that the most effective spreading of low-momentum fluid resulted from jet configurations that kept the vortices produced by flow control separate. Therefore, when considering practical application of flow control jet configurations, the 'best' configuration to use would be the Circumferential simulated ejector scheme, as it was the only configuration to reduce both total pressure distortion and flow swirl at the AIP.

Chapter 4: Experimental Validation

In order to validate the results of the CFD BLI serpentine diffuser flow control scheme, an experimental investigation was undertaken. This was accomplished by designing and building a unique test section to function in combination with the Techsburg Ejector-driven wind tunnel facility. When combined, the setup was capable of matching the flight Mach number and altitude consistent with BWB cruise conditions.

4.1: Facility Overview

The tunnel operates by using a large ejector-pump to serve as a suction source for the tunnel test section; air from high-pressure tanks is driven through a nozzle contained in the ejector pump. The tunnel configuration for this experiment is represented in Figure 4.1. As shown, the low pressure created locally by a supersonic jet entrains air from its surroundings by drawing it through the test section. This draws high-speed, low-pressure, low temperature flow through the test section. This facility operates in contrast with conventional high-speed testing facilities, particularly when attempting to simulate low pressure, high altitude flight conditions. For conventional facilities to achieve high Mach number flows, one of several conditions typically applies: 1) small test sections not capable of simulating complex duct flows, 2) high costs associated with providing (blowing) a constant supply of air, or 3) the use of a cryogenic gas to simulate high-altitude conditions. Thus, the use of an ejector-based tunnel at Techsburg allows for the facility to provide the required test conditions at a minimum of complexity and cost associated with more conventional experimental facilities.

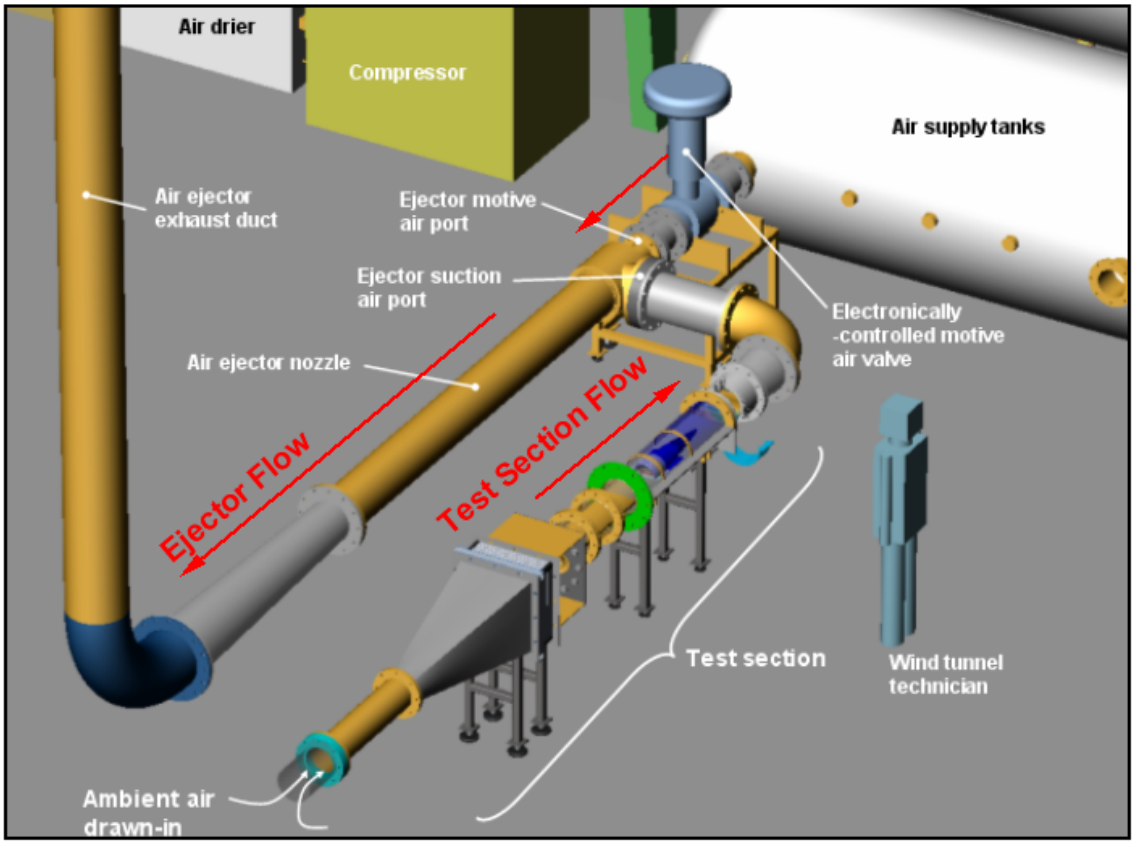

Figure 4.1: Techsburg Ejector-Pump Wind Tunnel Facility

A compartmental breakdown of the ejector-pump wind tunnel and a schematic of the operational elements are shown in Figure 4.2. As shown, the tunnel draws in ambient air through valve #1 at the lower left corner of Figure 4.1. Referring to Figure 4.2, the flow passes through a long pressure drop section designed to decrease flow total pressure to levels indicative of high altitude. The drop is achieved through friction losses in combination with the losses associated with an upstream valve and screens located in between the pipe junctions. The flow is then expanded and passes through a series of flow conditioning and honeycomb screens to facilitate flow straightening. Flow then enters a plenum chamber and is drawn into the semi-circular boundary layer growth region through a bellmouth entrance. Once in the growth region, the boundary layer is naturally 'grown' up to the target boundary layer thickness of 30% of the inlet height.

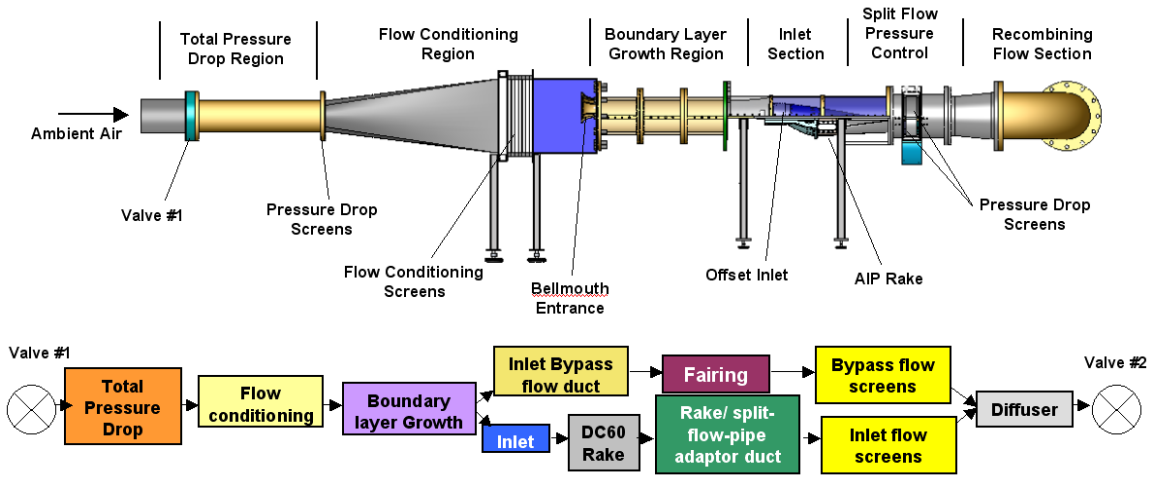

Figure 4.2: Ejector-Pump Tunnel Section

As shown in Figure 4.2, in the inlet section the flow is split into bypass and diffuser (duct) sections. The bypass region is used to simulate external flow over the engine nacelle and also ingests corner flows that have developed over the growth region. The diffuser (duct) represents the boundary layer ingesting serpentine diffuser. Located at the aft end of the diffuser is the six-arm total pressure distortion rake. After passing through a series of variable pressure drop screens, the flow is recombined and enters the suction port of the main tunnel ejector.

A more detailed explanation and description of the key tunnel components will now be discussed. Complete details of the setup are outlined in the Techsburg Wind Tunnel Design Report.[23]

4.1.1: Boundary Layer Growth Region

The boundary layer growth region is composed of a series of pipes that incorporated machined aluminum plates to represent the aircraft's upper surface, as depicted in Figure 4.3. These plates were tapered to account for boundary layer growth throughout this section. By accounting for the displacement thickness of the boundary layer, the axial pressure gradient was reduced to a minimal effect so that the flow throughout this region would remain effectively constant in velocity, and the boundary layer profile would be relatively unaffected. (The experimental measurements of this gradient are shown in Appendix J.) The bellmouth at the beginning of this section was

designed to draw flow from the plenum chamber with a low level of turbulence. Prior to entering the test section, the walls near the inlet diffuse to allow for the natural compression associated with ram effects of the inlet, and to allow smooth passage of flow streamlines into the bypass flow over the engine nacelle. The curvature of the wall was obtained by extracting the coordinates of a flow streamline obtained from CFD analysis at the design condition.

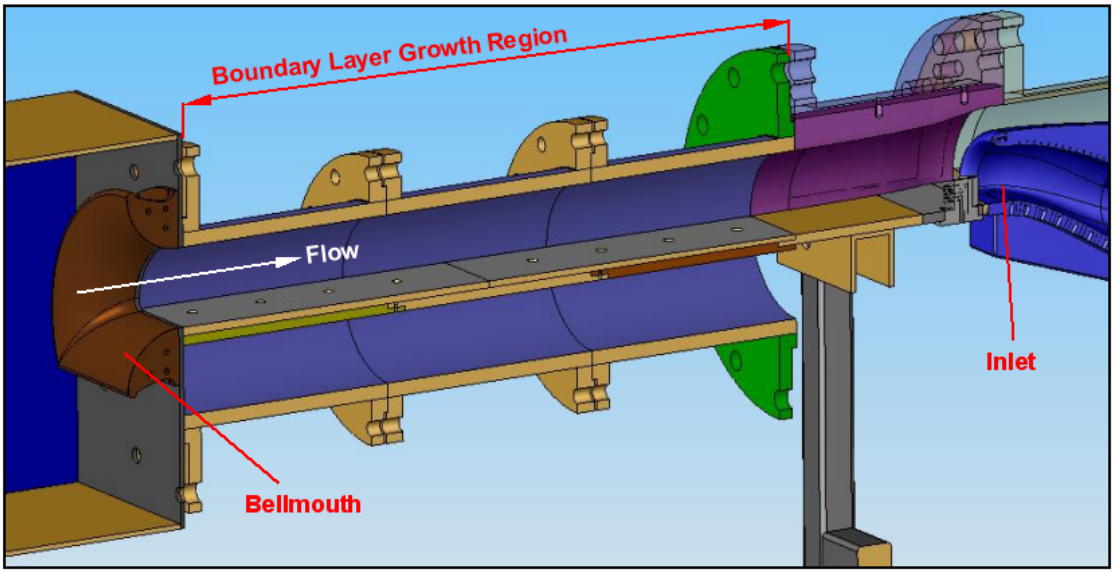

Figure 4.3: Boundary Layer Growth Region

4.1.2: Inlet test Section

Once the flow passes into the inlet test section, it is split into two separate flows. Some of the flow is ingested into the BLI diffuser, and the remainder of the flow is diverted around the outside of the inlet to simulate freestream flow around the engine nacelle. This flow division is shown in Figure 4.4.

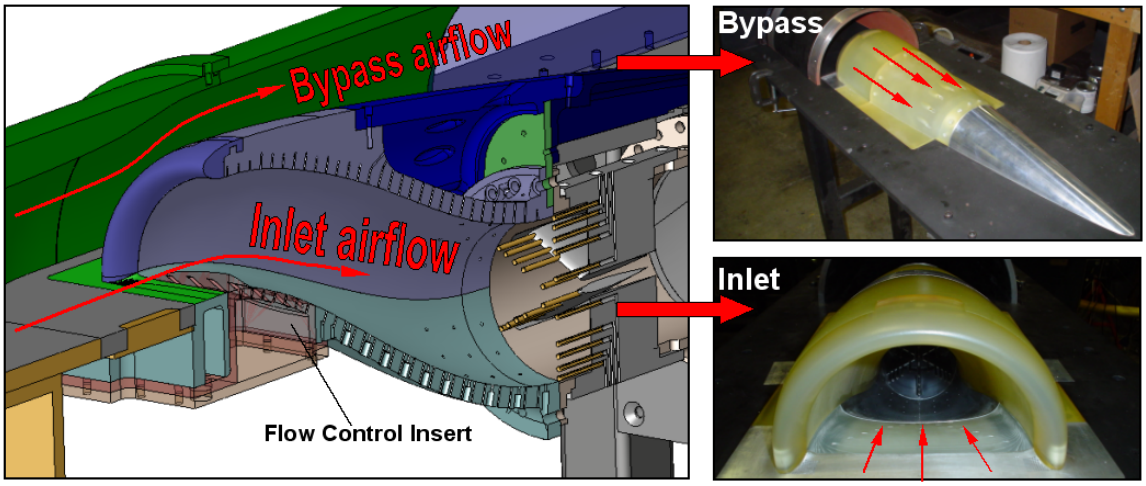

Figure 4.4: Inlet Test Section

By inserting differential screens into the flow at a downstream location, the capture area of the inlet was effectively altered. (To be discussed in further detail in a later section.) The inlet flow passes through the BLI diffuser, over the flow control insert, and through the distortion rake which measures the effects of the flow control.

The diffuser itself is composed of several major components. The upper half of the diffuser is made using stereo-lithography (SLA) techniques. A removable cover in the bypass flow allows for access to pressure instrumentation located throughout the diffuser. For safety purposes, the lower inlet section is machined from aluminum and supports the pressure differential between operation tunnel conditions and atmosphere, a difference of approximately 10psi. A large slot is cut out of the diffuser to allow for installation of a flow control insert specific to the blowing configuration to be tested. In addition, the floor of the lower inlet has several holes drilled near the nacelle lip location to facilitate flow suction to be used in flow-control ejector pump modeling.

4.1.3: Flow Control Inserts

As flow passes into the diffuser, it passes over the test configuration flow control insert. The inserts were made using SLA, and represent variations of the circumferential and reverse Pyramid configurations studied in the CFD flow control analysis. The jet configurations are shown in Figure 4.5. The blowing angles of the jets are the same as those used in the CFD analysis, and draw air through a plenum incorporated into the insert. As will be noted in a later section, the motive pressure is obtained through regulated control of the pressure differential between tunnel and atmospheric conditions. The size of the flow control jet holes are scaled equivalents in cross-sectional area to those used in the CFD analysis. (The test configuration is slightly larger in size than the CFD solutions.) In contrast to the jets modeled in CFD using cell boundary conditions, these jets have a round cross-section and incorporate a significant length to diameter ratio (~10:1) to facilitate a developed jet flow.

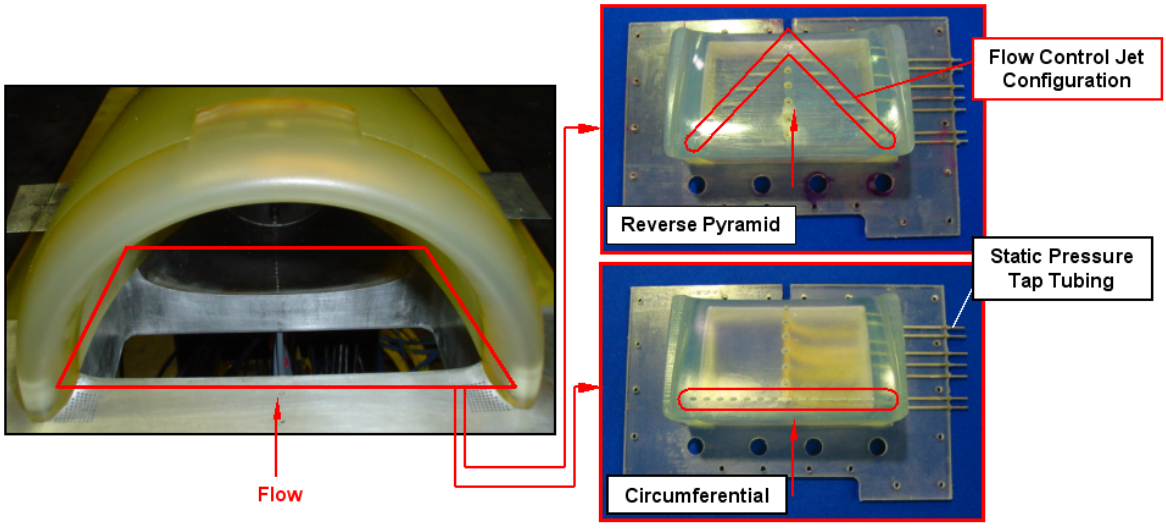

Figure 4.5: Flow Control Inserts

4.1.4: Distortion Rake

The distortion rake is a standard six-arm design that measures inlet face (AIP) total pressure, and correlates the data according to the DC(60) distortion parameters. A cross-section and photo of the rake are shown in Figure 4.6. The pressure probes are located such that all measurements represent an equal area-averaged segment of the AIP total pressure. The total pressure probe tips are located directly at the AIP to measure the flow at the virtual engine face. The probes extend 1.25" upstream from the airfoil-shaped struts on which they are mounted in an attempt to minimize the potential effects of the struts. In addition, the probe tips have a 40º internal conically tapered head to accept flow vectors that are not aligned with the axial flow direction by as much as 28°.[24] The rake airfoils use a NACA 0010 airfoil section and are designed to create a minimum flow blockage of approximately 20% in terms of frontal area. The curvature of the rake walls also incorporates a slight area increase to offset flow blockage effects due to the airfoils and associated boundary layer growth. In addition to the 30 total pressure probes, 6 static pressure measurements are located on the wall between the rake blades, and allow for the approximate calculation of dynamic pressure at the AIP.

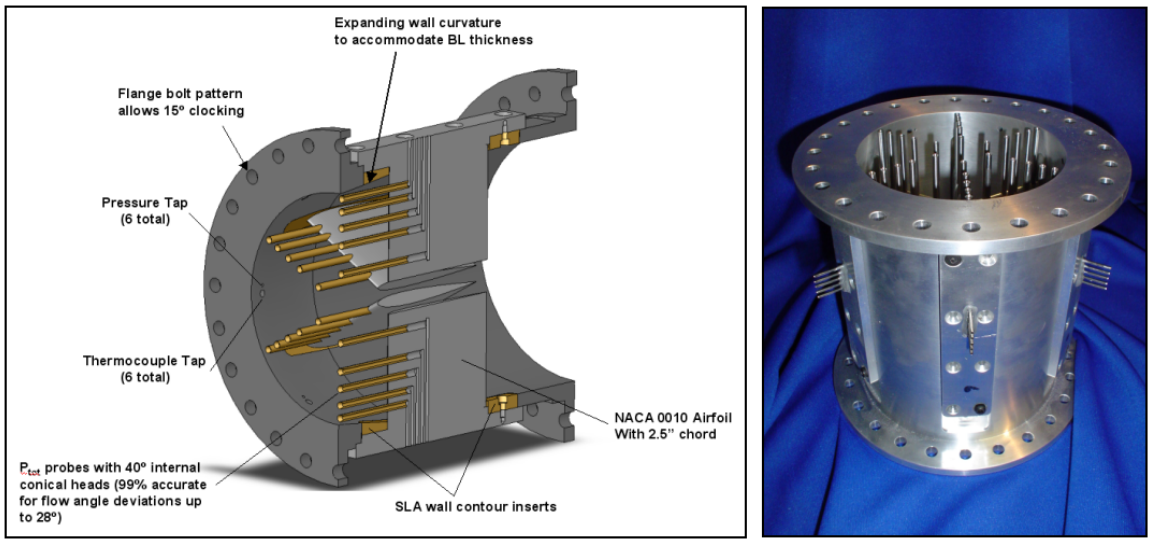

a) Distortion Rake Section Rendering

b) Experimental Distortion Rake

Figure 4.6: Six-Arm Total Pressure Distortion Rake

4.1.5: Pressure Drop Screens

As previously noted, the inlet capture area is controlled through the use of screens at a location downstream of the test section. At this location, the inlet and bypass flows are still separate. The pressure drop section is shown in Figure 4.7. A differential blockage is achieved through the installation or removal of a series of screens in the upper and lower flows. The pressure loss associated with an installed screen was used to create a pressure differential between the upper (bypass) and lower (inlet) sections. A total of four upper and four lower screens could be installed by opening an access hatch in the side of the tunnel. Fine-tuning of desired mass flows could be achieved through the installation of duct tape on top of the screens. At the aft end of this component, the upper and lower flows are slightly diffused and recombined prior to entering the suction port of the ejector.

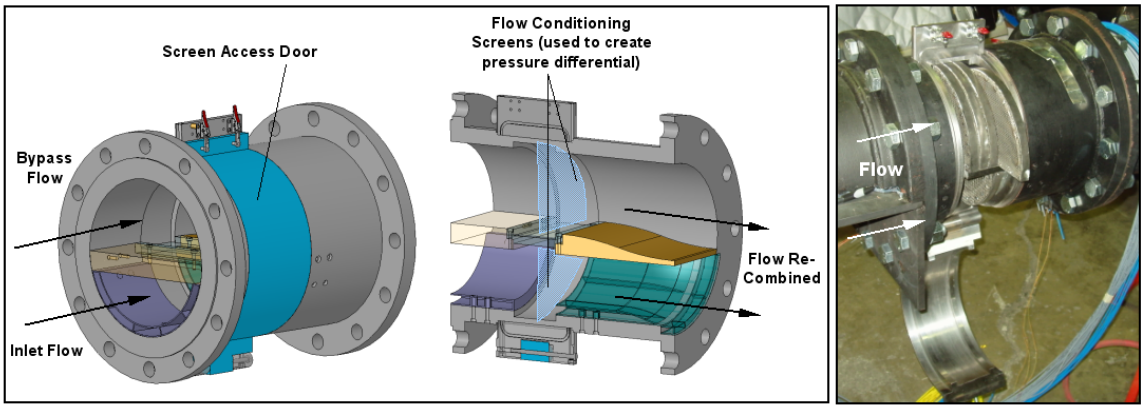

a) Pressure Drop Section Rendering b) Experimental Section

Figure 4.7: Pressure Drop Section

4.1.6: Flow Control: Blowing

As depicted in the schematic and photo shown in Figure 4.8, the blowing element of the flow control was achieved through valve control of atmospheric air into the test section. By adjusting the valve position, the plenum pressure of the flow control insert was adjusted, thereby altering the mass flow through the flow control jets. The total mass flow of the jets was measured through the use of an orifice plate.

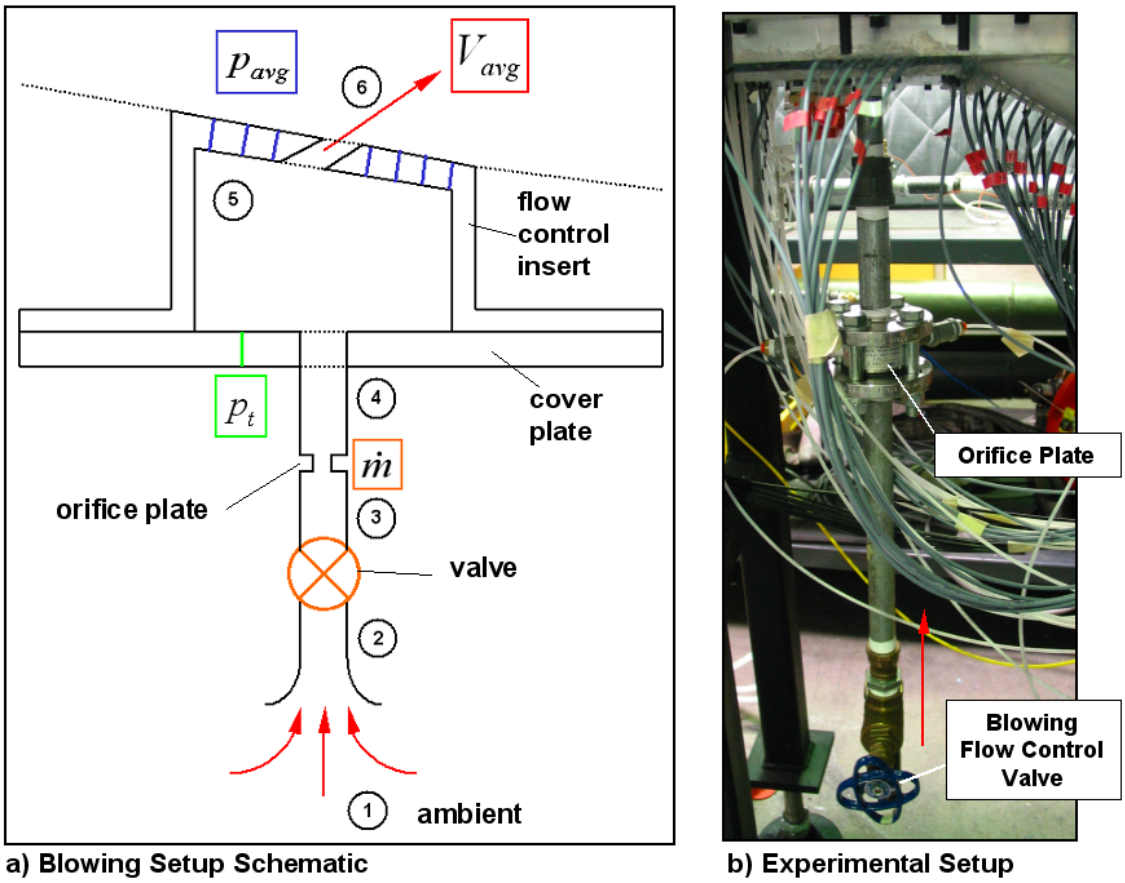

Figure 4.8: Flow Control - Blowing Apparatus

4.1.7: Flow Control – Suction

To achieve the required suction rates to simulate an ejector-pump based flow control system, a Vaccon VDF-550 ejector pump was used in conjunction with a laminar flow element (LFE). The Vaccon ejector-pump used the 210 psi motive air from the main tunnel ejector to draw air through the suction holes located in the lower inlet section. The suction schematic and system are shown in Figure 4.9. The suction mass flow rate was measured using the LFE, which incorporated a low pressure-drop measurement. The motive and suction flows were recombined inside the Vaccon ejector and drawn into the tunnel flow upstream of the main tunnel ejector suction port. The Vaccon ejector could also be adjusted to entrain different suction mass flows, thereby adjusting the amount of suction used in the tunnel model.

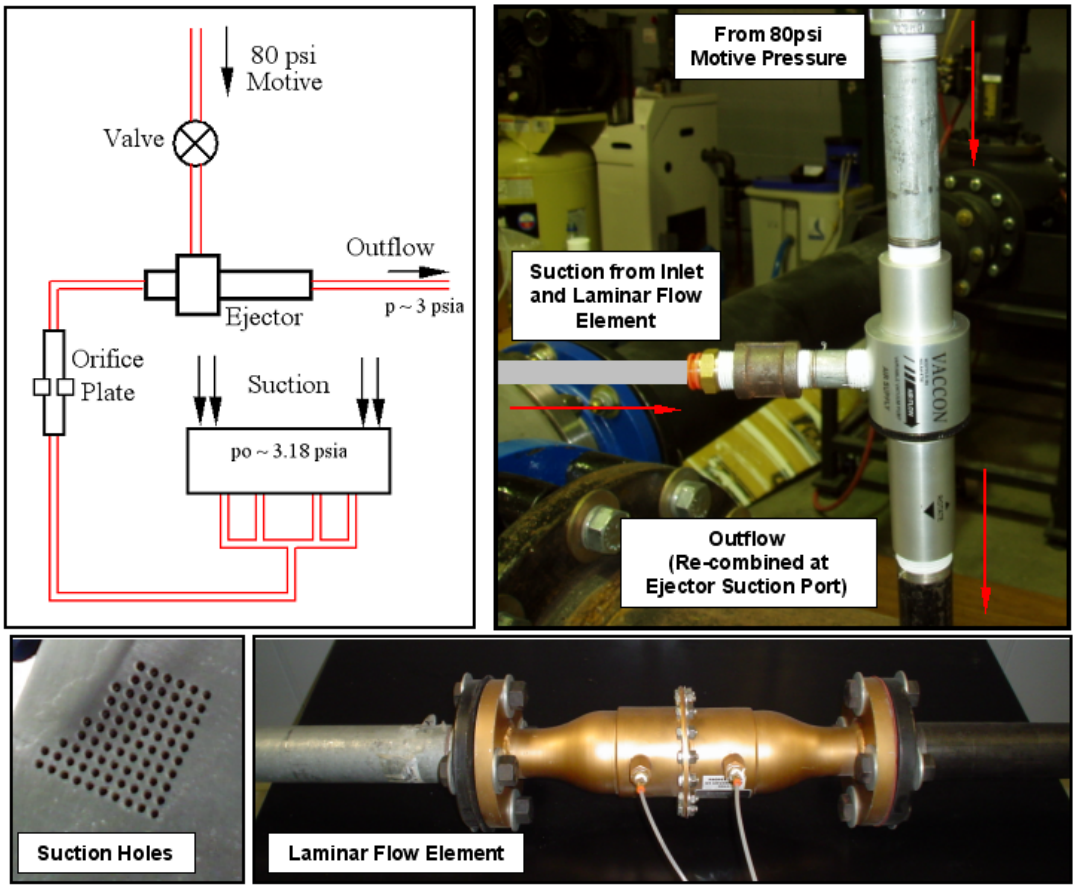

Figure 4.9: Flow Control - Suction Apparatus

4.2: Wind Tunnel Instrumentation

The wind tunnel setup was heavily instrumented with a variety of pressure measurements. Static pressure measurements were located axially throughout the boundary layer growth region and also in a transverse direction immediately in front of the inlet. Freestream total pressure was measured using two 1/8" diameter keel probes located immediately upstream of the flow diffusion in front of the inlet. The boundary layer velocity profile was measured using a six-probe boundary layer rake located 2" upstream of the inlet throat, as shown in Figure 4.10.

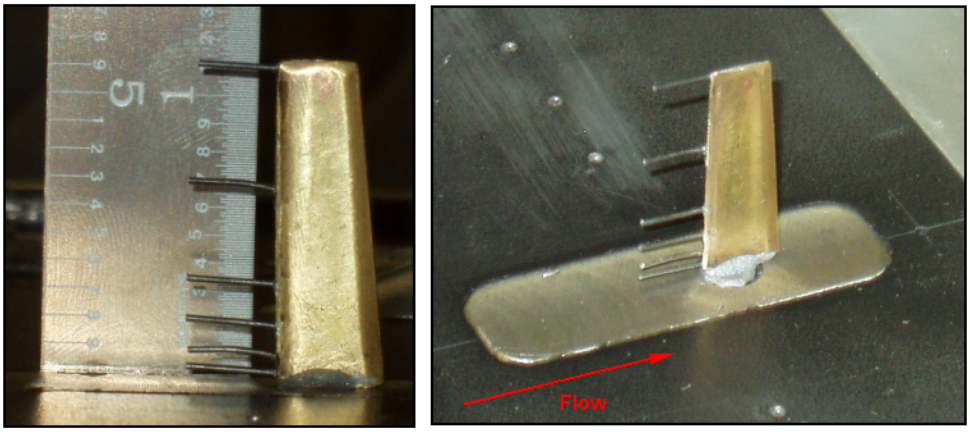

Figure 4.10: Boundary Layer Rake

The inlet itself is heavily instrumented on both the upper and lower sections. The upper and lower inlets each house 30 static pressure taps along the inlet centerline. The setup is shown in Figure 4.11 with the access cover removed from the upper inlet section. All AIP instrumentation is installed in the distortion rake, which incorporates 30 total pressure measurements and six static pressure measurements.

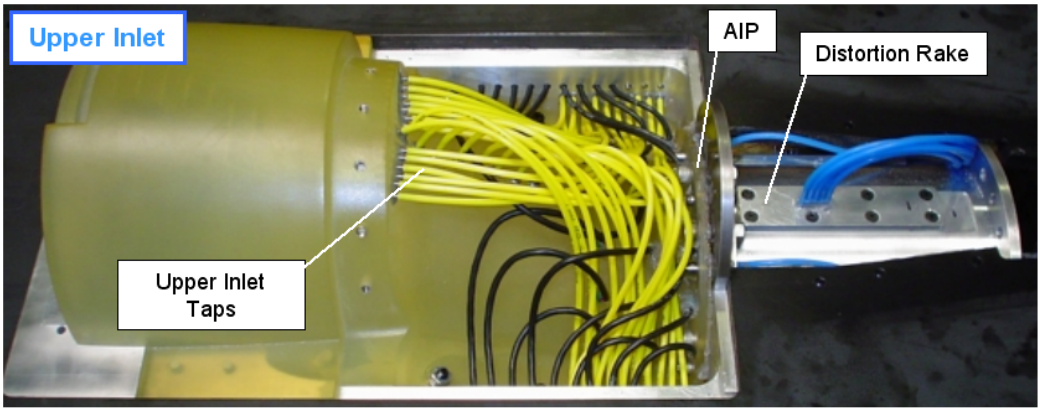

a) Upper Inlet Instrumentation

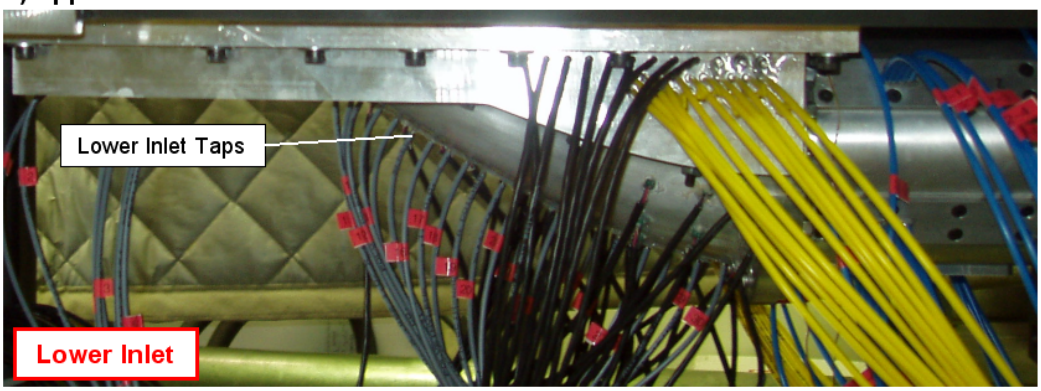

b) Lower Inlet Instrumentation

Figure 4.11: Inlet Instrumentation

4.2.1: Pressure Transducers and Data Acquisition

Tunnel data was collected using a variety of analog and digital pressure transducers:

- Scanivalve DSA Pressure Modules:
  - 8 channels, 0-30 psid
  - 24 channels, 0-5 psid
- PSI System Digitizer
  - 32 channels, 0-15 psid
- Scanivalve ZOC Pressure Modules
  - 8 channels, 0-15 psid
  - 40 channels, 0-5 psid

All data acquisition was collected through the use of National Instruments Lab View software. The data acquisition system is shown in Figure 4.12.

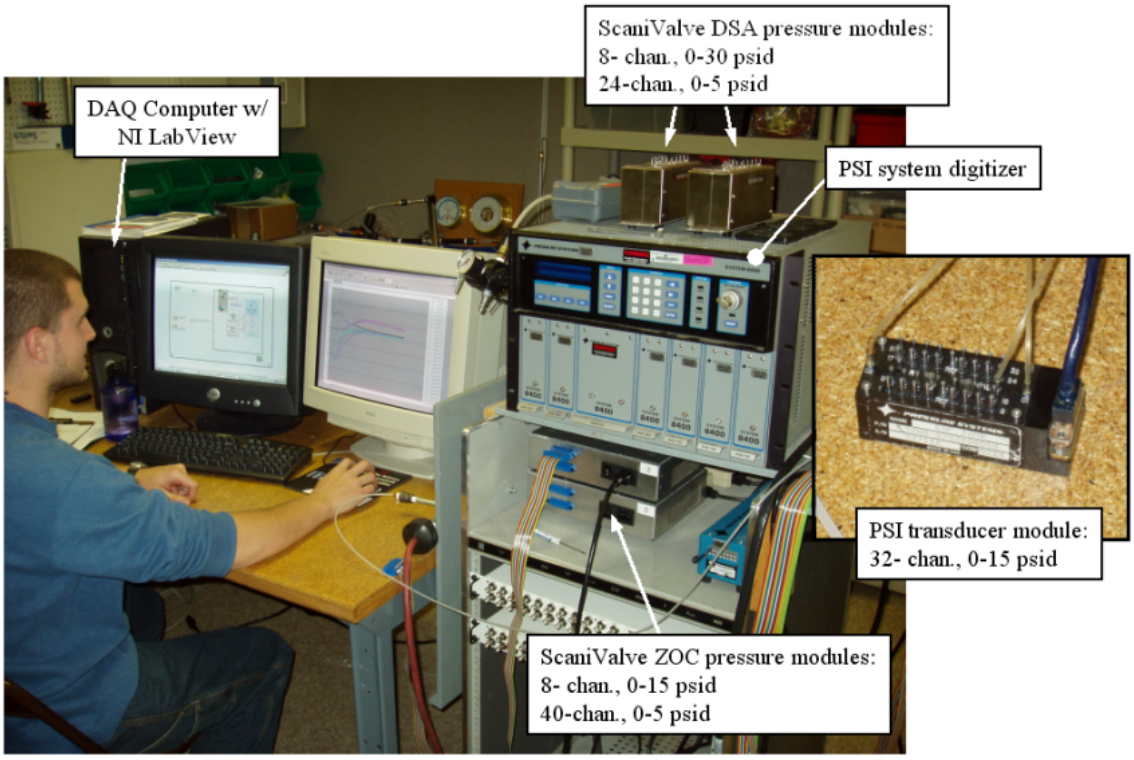

Figure 4.12: Data Acquisition System

4.3: Wind Tunnel CFD

As a predictive measure, the wind tunnel configuration was modeled and analyzed with CFD to determine any possible undesirable flow qualities resulting from the test configuration. Results obtained from wind tunnel modeling suggest that the boundary layer from the outer tunnel walls will not be ingested into the inlet at the desired operational flow conditions, and thus will not affect the diffuser flow. Figure 4.13 shows the centerline Mach number contours of the modified wind tunnel design. Also, the corner flows that extend along the length of the boundary layer growth section are sufficiently diverted around the inlet into the bypass flow section. The boundary layer growth section of the wind tunnel is designed to increase in area to account for boundary layer growth through this section. The goal of this area expansion is to eliminate or at least reduce the magnitude of any axial pressure gradients that may affect boundary layer growth. In addition, the AIP distortion pattern remained essentially unaltered for the test configuration. Investigations of engine mass flow and the effect on distortion are noted in Appendix D.

Figure 4.13: Wind Tunnel Mach Number Contours

4.4: Experimental Results

During the preliminary wind tunnel development, the relative flow quality and characteristics were investigated. Perhaps the most important flow characteristic to be determined was the boundary layer thickness and velocity profile, as CFD predictions showed that inlet performance was very sensitive to changes in the boundary layer profile. A complete discussion of the tunnel flow quality investigations may be found in Appendix J. Evaluation of experimental uncertainties for all results are based upon the Kline-McClintock relation[25], with further discussion in Section 4.4.5, and detailed calculations shown in Appendix H.

4.4.1: Ingested Boundary Layer Profile

The tunnel boundary layer profile was measured using the boundary layer rake described in Section 4.2, which was positioned approximately two inches upstream of the inlet throat. The measured profile was then compared with CFD predictions of the tunnel behavior, as shown in Figure 4.14. From the measured profile, the experimental points collected by the rake match closely with the computationally predicted profile. Since the experimental points appear to match, it is believed that the ingested boundary layer is of appropriate thickness. The boundary layer profile was calculated by obtaining the flow Mach number in the boundary layer from measured total pressures (rake), and local wall static pressure and using the local total temperature to calculate the freestream velocity. Both the CFD and experimental velocities were non-dimensionalized by the freestream velocity (Uref) from the location of an upstream keel probe. The upstream velocity U_{ref} (calculated from total pressure, local static pressure and temperature) was used to non-dimensionalize the velocity profile since the effects of the engine ram make it difficult to determine a the local freestream velocity. As noted in Appendix H, the uncertainty in experimental velocity values was ± 1.5 m/s

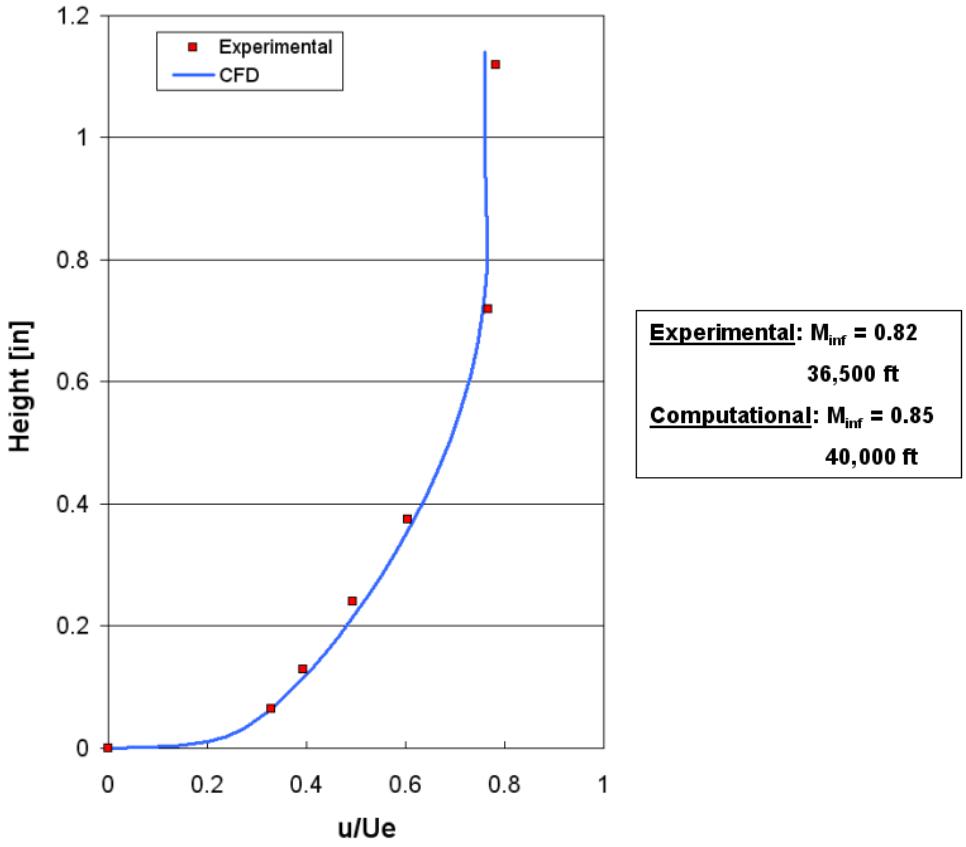

Figure 4.14: Wind Tunnel Boundary Layer Velocity Profile at x/h = -1.0 from Throat

4.4.2: Baseline Distortion Contours

Prior to application of flow control to the inlet, baseline flow measurements were performed as a means for comparison with the CFD results. In order to validate the CFD flow control design tool, the baseline CFD flow predictions needed to match well with the experimentally measured quantities. Because the distortion rake takes finite area-averaged measurements, CFD values were interpolated onto a 'virtual rake' to simulate how the contours would appear if obtained by the experimental rake. The baseline contours are shown in Figure 4.15. As shown, the baseline distortion contours are captured well during the experiment. CFD contours are based upon a freestream Mach number of M = 0.85. However, freestream values achieved during experimental work were slightly lower. (M ≈ 0.82) In addition, the altitude conditions during testing were also lower than computationally modeled due to insufficient upstream pressure drop. Actual modeled altitude during tunnel testing was approximately 36,500 ft, as opposed to the CFD simulated altitude of ~39,000 ft. The reduction in Mach number combined with

the altitude difference accounts for some of the disparity in distortion intensity between the experimental and CFD cases.

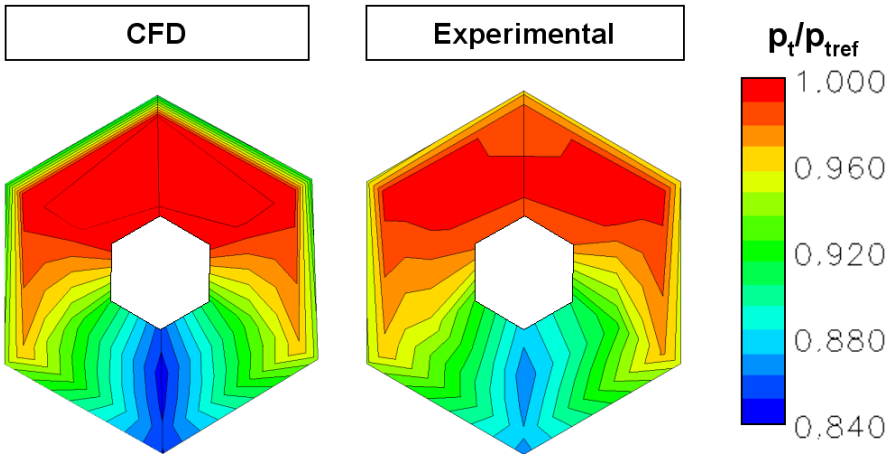

Figure 4.15: Baseline Solution distortion Contours (No flow control)

4.4.3: Effects of DC(60)

Due to the physical constraints of wind tunnel modeling, it was not possible to measure AIP distortion with the fidelity obtainable using CFD. Thus, some limitations are imposed upon the results obtainable during experimental work. These limits focus on the finite nature of the distortion rake, and most in particular to the determination of the DC(60)q distortion parameter which uses the average dynamic pressure at the AIP as a non-dimensionalizing factor.

This difficulty is primarily due to the need to estimate both AIP average static and total pressures based on finite measurements when calculating DC(60)q. The average total pressure is computed using the 30 rake measurements from within the flow field at the AIP. However, the average static pressure is calculated from wall measurements at select locations around the AIP. This can lead to a substantial error in estimation of the face dynamic pressure, and thus contributes to error in the DC(60)q metric. By examining the CFD interpolated results and comparing them to the CFD finite measurements used in this experiment by way of a "simulated" rake, this estimation can result in a DC(60)q uncertainty of ± 0.038. (As determined in Appendix H.) The reason for this variation is

apparent when examining the AIP static pressure contours of Figure 4.16, and the significant variation in static pressure across the engine face.

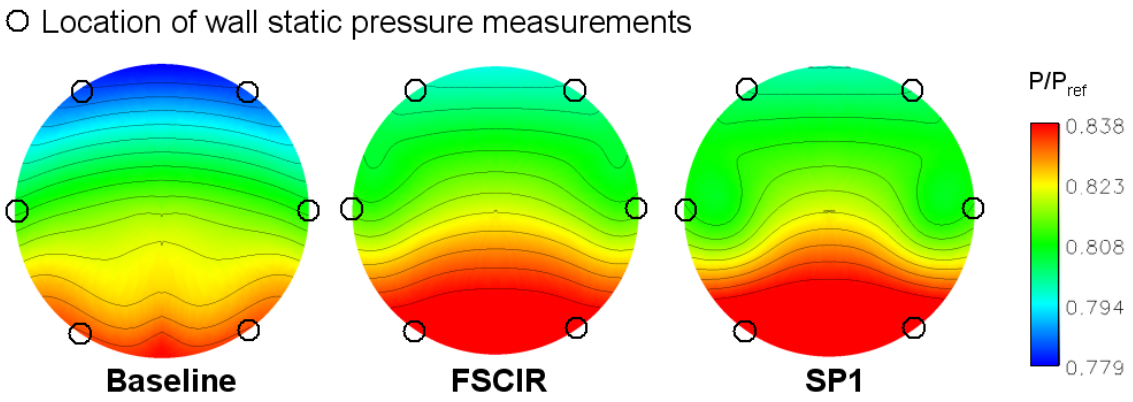

Figure 4.16: AIP Static Pressure Contours

Because of these inaccuracies, any calculation based upon the face dynamic pressure will inherently have high error. For this reason, it seems much more practical to use the DC(60)pt parameter to describe results. Results obtained in this study also highlight an increased accuracy when comparing to predicted DC(60)pt values, in addition to being a more robust parameter capable of collapsing results for different flow rates and duct sizes.[4] Ultimately, engine companies have distortion descriptors that are more complicated, more costly, and tailored to the specific performance characteristics of their particular engine capabilities. For further discussion, refer to Appendix M.

4.4.4: DC(60) Distortion Results – Reverse Pyramid Flow Control

The first configuration tested utilized the reverse flow control scheme. Due to the small confines of the scaled-down test inlet and complexity constraints, it was not possible to create a working ejector pump model. Thus, the ejector concept was simulated using separate blowing and suction mechanisms as described earlier. Experimental investigations examined both blowing only and the simulated ejector.

Insight can be gained by examining the AIP total pressure contours of the experimental values and comparing them to values predicted by CFD. The CFD simulated rake data is compared to experimental data for similar blowing rates in Figure 4.17. Distortion values are also shown. The three cases represent small, medium, and large blowing flow rates (efforts). Qualitatively, the pressure contours show that the experimental and computational rake values capture the same flow structures. Small magnitude differences are apparent due to variation in flow Mach number. Experimental flow contours show reasonable (although not perfect) symmetry. In general it is apparent that CFD tends to over-predict distortion for low blowing efforts. This is consistent with observations by Allan[14], and is likely the result of a lower predicted minimum total pressure value, and a total pressure maximum that can at times exceed unity. Quantitatively the distortion results match very closely, with CFD distortion values slightly higher than obtained in experiment.

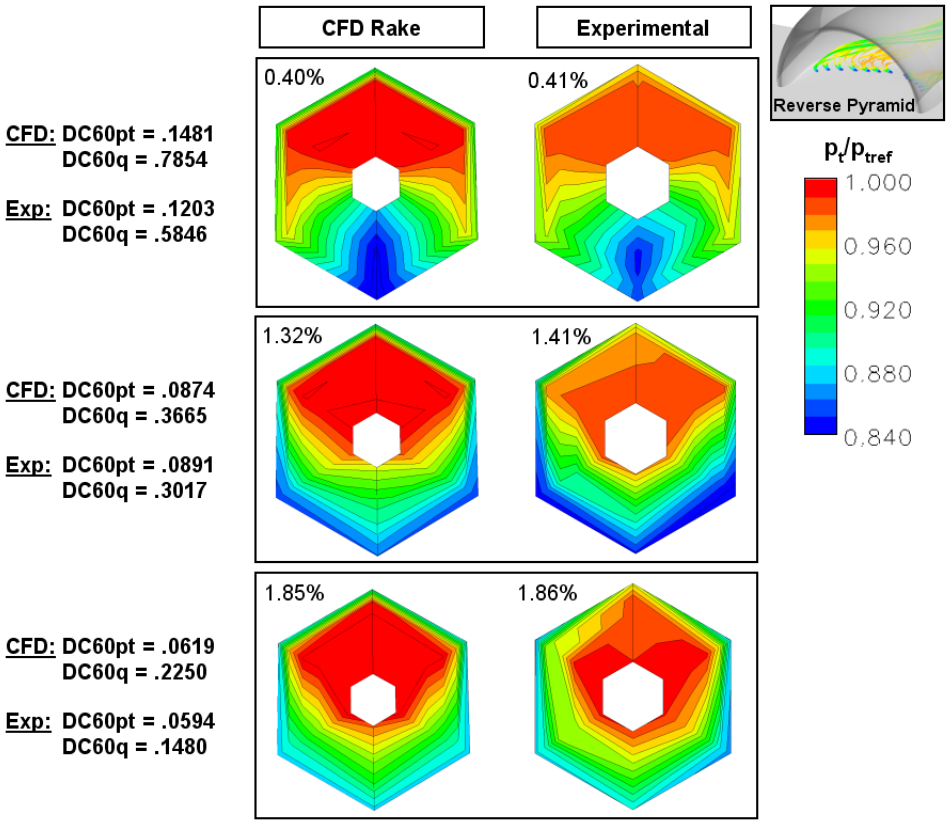

Figure 4.17: Reverse Pyramid Blowing Total Pressure Contours

The experimental results in Figure 4.18 show distortion investigations of the reverse Pyramid flow control configuration as characterized by the DC(60)q parameter. The distortion parameters shown represent investigations of the effect of blowing rate only, and as such do not use simulated suction. These results are compared with CFD results that simulate the same conditions. From Figure 4.18 it is apparent that the experimental investigations were successful in predicting the trends associated with the application of flow control. Predictions for lower rates (or effort) of flow control were less accurate as compared with computational values, although the presence of jet holes may have had a small effect on the flow, particularly for low (or zero) flow control efforts. This over-prediction can also be associated with the turbulence model used in the CFD analysis, which can affect the strength of large vortex structures, particularly those that are present in the low flow control effort solutions. This over-prediction is also subject to the difficulties expressed previously when trying to measure the AIP dynamic

pressure. In addition, the over-prediction is consistent with results obtained by Allan[14] in similar computational investigations of active flow control.

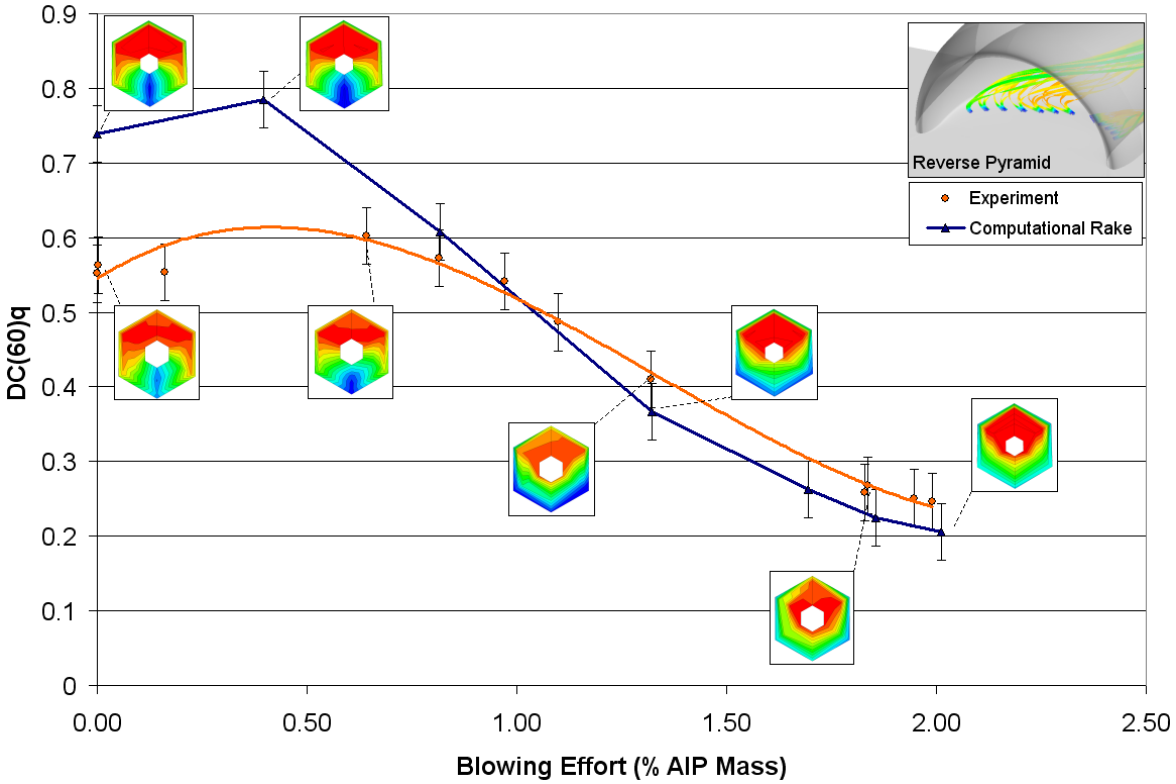

Figure 4.18: DC(60)q Experimental Distortion Results - Reverse Pyramid Blowing

As shown, the visual flow contours agree very well in form between experimental and computational depictions. All data sets obtained show a small rise in distortion for low flow control efforts. This behavior is not uncommon when using jets to control distortion; the addition of fluid with less total pressure than freestream values increases the flow distortion at first when the jets are not effective in countering the secondary flows present within the flow. However, once the jets begin to become more effective, the distortion begins to decrease. Using this configuration, for blowing efforts of greater than 1.5% AIP mass there are diminishing returns for flow control, although the distortion continues to decrease. However, the 'acceptable' DC(60)q distortion value of 0.1 is not quite achieved. It seems realistic that a more thorough system optimization could result in values at or below this mark.

Computational DC(60)pt values are closer in their prediction to experimental values, as shown in Figure 4.19. The trends for this parameter are very similar to those seen in the DC(60)q parameter, showing the same initial rise in distortion as well as a slight decrease in effectiveness for blowing mass flows of greater than 1.5% AIP mass. This figure also shows a slight over-prediction in distortion as measured by a simulated CFD rake. This difference is the most likely the result of a discrepancy in the severity of the distortion at the AIP due to the CFD turbulence model.[21] This discrepancy is accentuated by the difference in freestream Mach number between experimental and computational investigations.

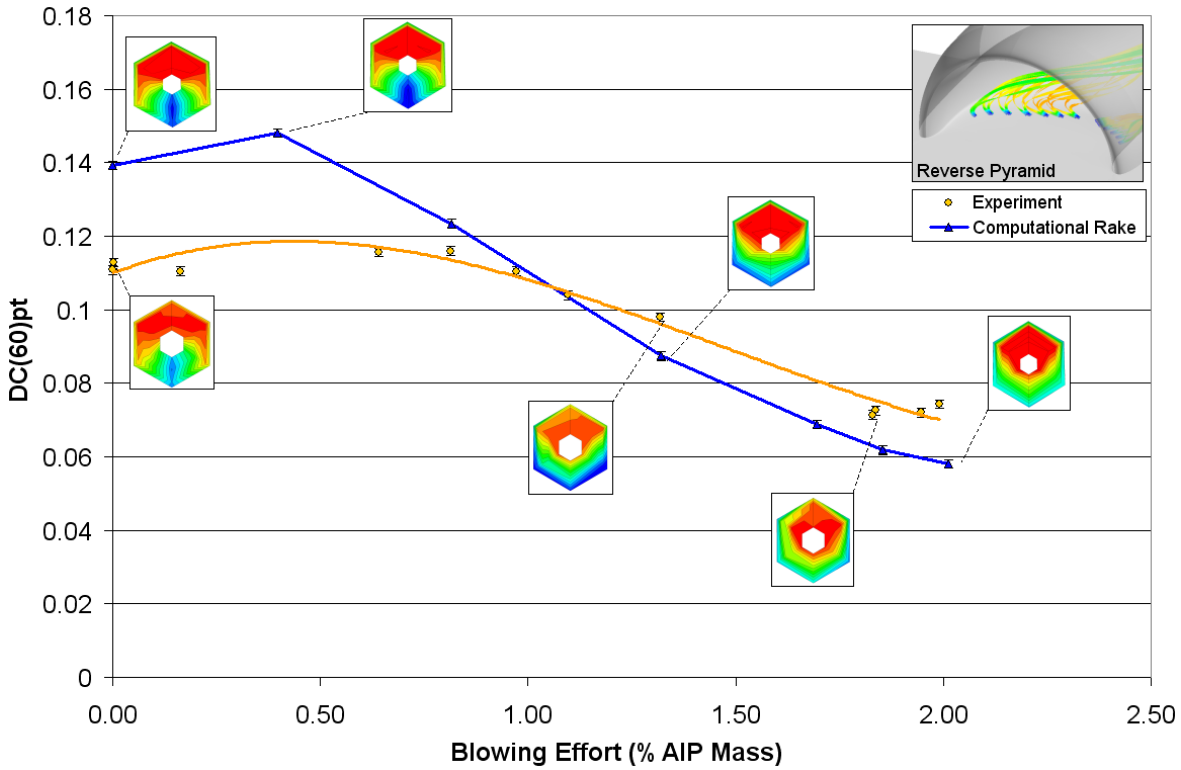

Figure 4.19: DC(60)pt Experimental Distortion Results - Reverse Pyramid Blowing

The AIP total pressure recovery values as referenced to freestream total pressure are shown in Figure 4.20. The spread in the results shown is strongly influenced by slight differences in freestream Mach number from run to run. In addition, the referenced total pressure does not represent the average total pressure of all flow ingested into the inlet as it does not account for the presence of the boundary layer, which biases the experimental estimates of the inlet pressure recovery towards lower values.

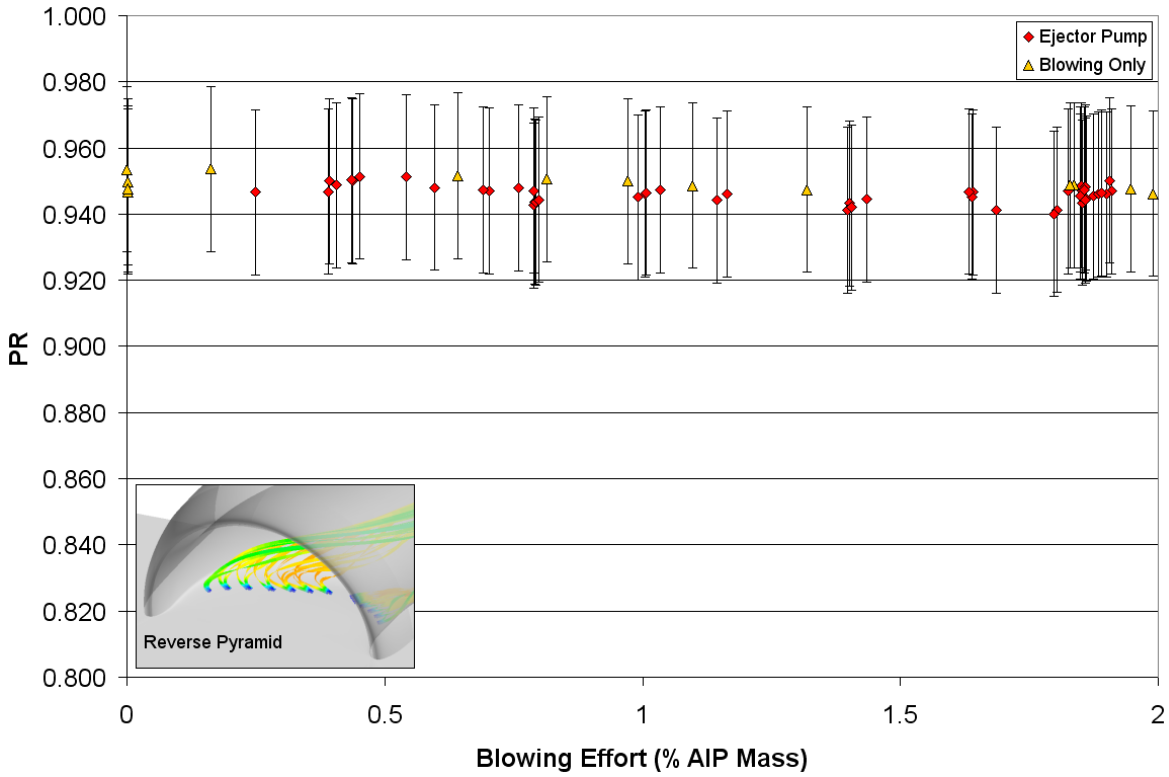

Figure 4.20: Pressure Recovery Experimental Results - Reverse Pyramid Blowing

4.4.5: DC(60) Distortion Results – Circumferential Flow Control

Due to the physical constraints associated with the wind tunnel setup, the circumferential blowing case selected was not identical to the configuration tested in initial flow control CFD investigations. The primary difference was that in the experimental setup no jets could be placed on the diffuser sidewall. Thus, all jets in this configuration are mounted on the floor. This limitation is a result of the small scale associated with the test, and could be more easily applied in tests at a larger scale. However, CFD predictions of the experimental setup were conducted with only a reasonably small variation in jet configuration.

The total pressure contours from CFD and experiment for the circumferential blowing case are compared in Figure 4.21. Contours are non-dimensionalized by the freestream total pressure, with the blowing effort expressed as a percentage of total AIP mass.

As noted in previous sections, CFD tends to over-predict the flow distortion for small flow control efforts. This over-prediction decreases as the blowing effort increases. As noted before, this is likely the result of the turbulence modeling of the vortex behavior; as the scale of the large disturbance is decreased, predictions become more accurate. Over-prediction of distortion is also the result of a variation in freestream Mach number. (Experiment 0.03 Mach lower.)

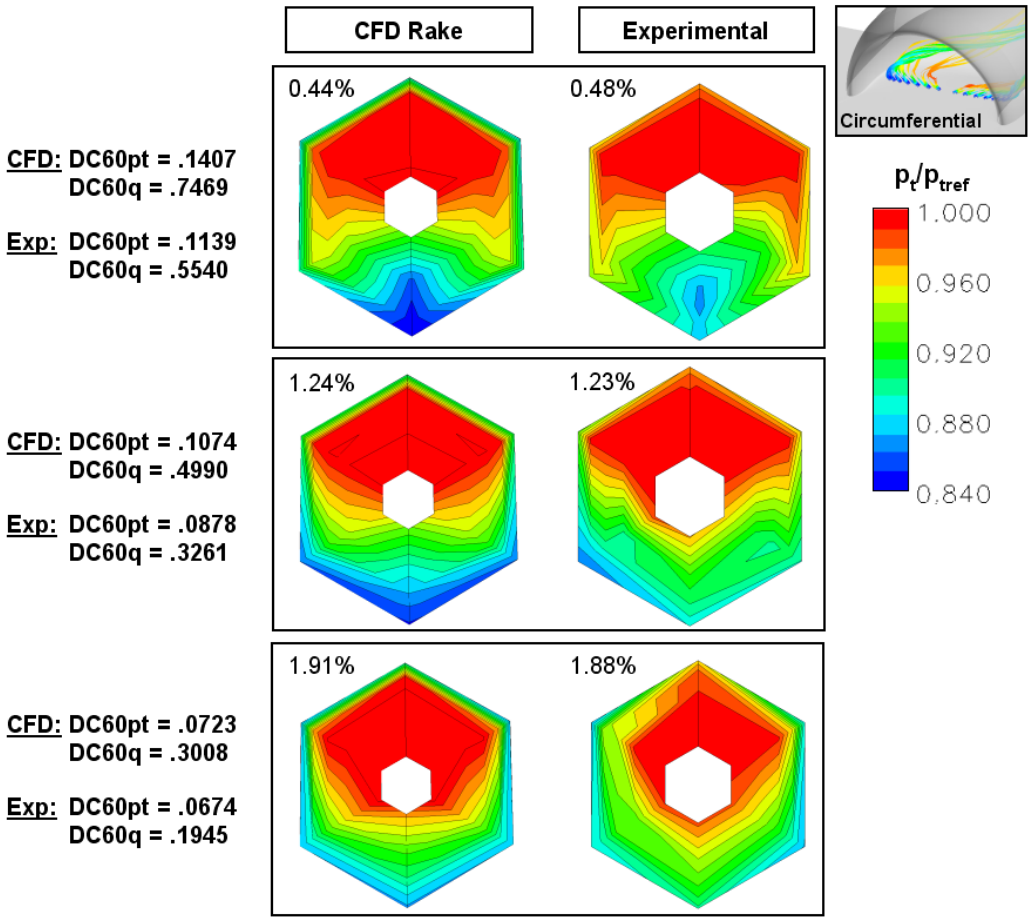

Figure 4.21: Circumferential Blowing Total Pressure Contours

These predictions are compared to the obtained experimental DC(60)q values in Figure 4.22 for various flow control rates/efforts. Investigations of the circumferential insert yielded similar trends to those obtained in the reverse Pyramid blowing investigation. As before, the distortion shows a slight rise for little (or no) blowing effort. Experimental baseline (no flow control) values for the circumferential insert are also lower than previous values. This is likely the result of the flow control jets being located

in a less sensitive (upstream) location, along with the possibility of a slightly different flow control insert fit.

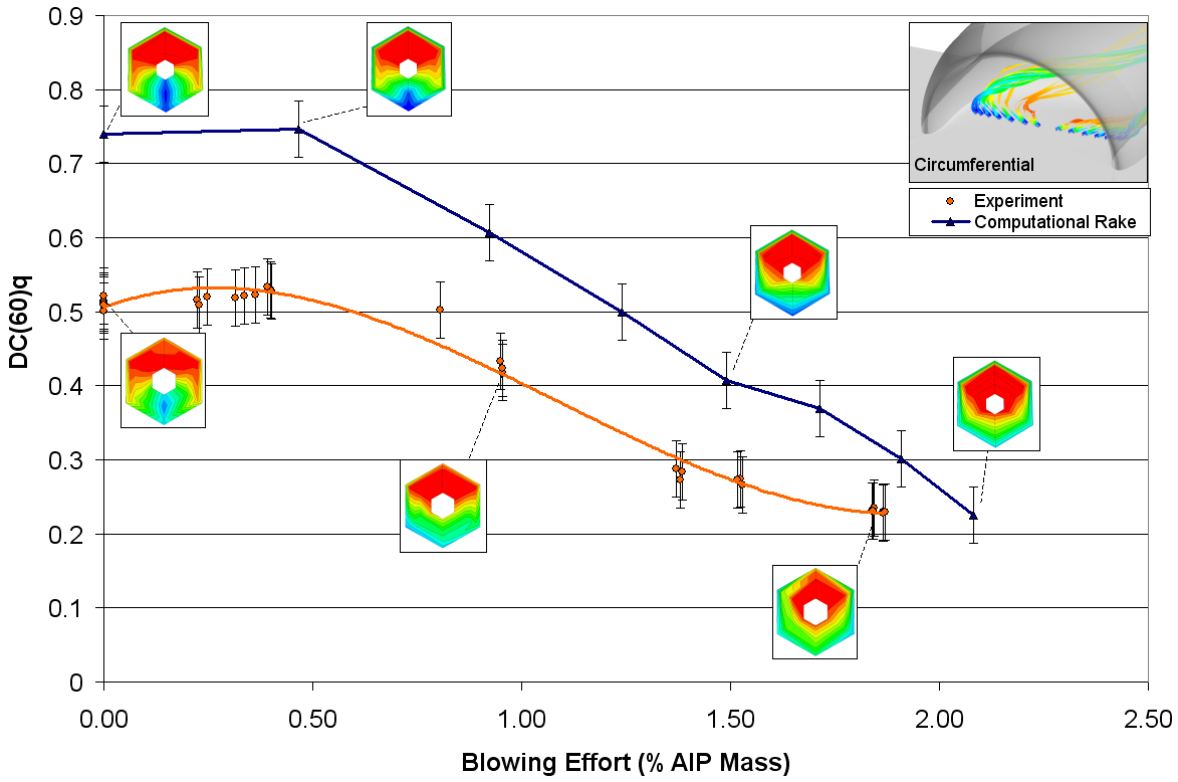

Figure 4.22: DC(60)q Experimental Distortion Results - Circumferential Blowing

The DC(60)pt results for the circumferential flow insert are shown in Figure 4.23. As before, the DC(60)pt computational results compare much more closely with the obtained data. A similar trend is observed in the experimental data with a slight initial rise in distortion coupled with a rate of 'diminishing returns'. CFD also predicts a sudden increase in jet effectiveness for blowing mass flows greater than 2% AIP mass. However, the experimental facility did not prove capable of achieving these mass flows. CFD analysis shows that for mass flows slightly over 2% AIP mass the jets become choked. However, altering the plenum supply pressure should still result in an increase in jet mass, and thus an increase in jet momentum.

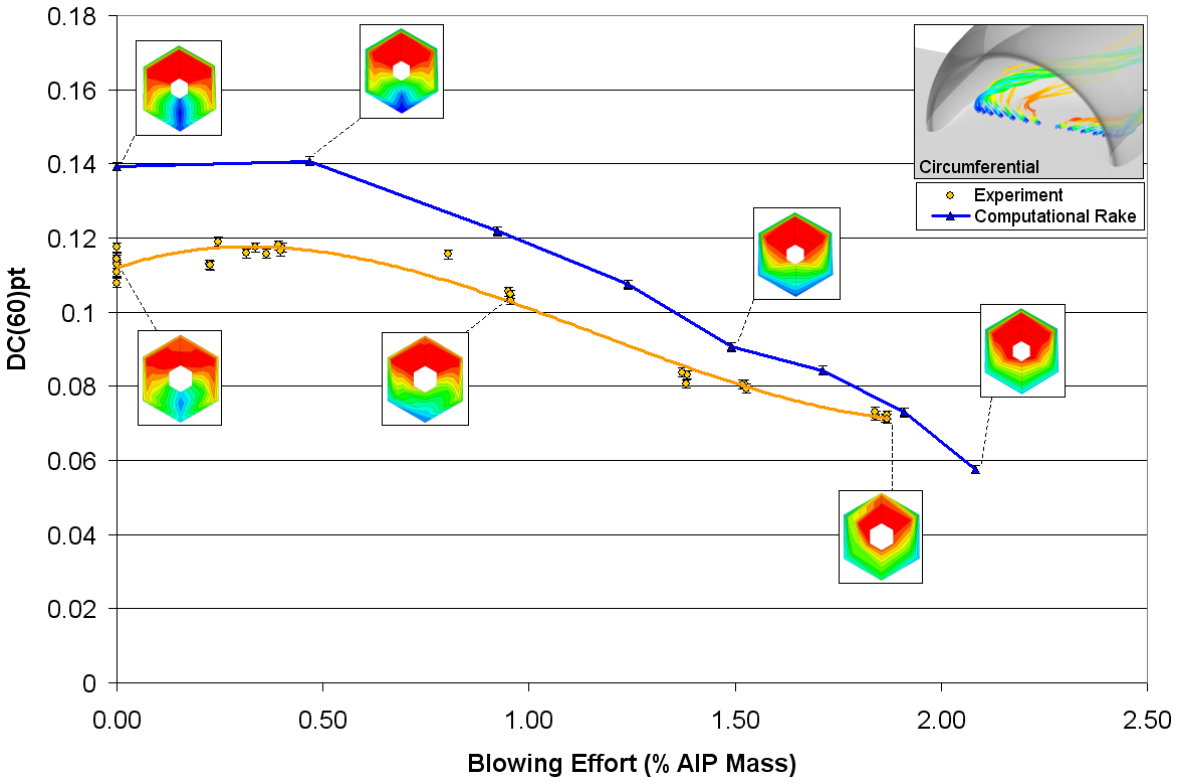

Figure 4.23: DC(60)pt Experimental Distortion Results - Circumferential Blowing

The circumferential insert pressure recovery values are shown in Figure 4.24. As can been seen, there is not a large impact on inlet pressure recovery resulting from the application of flow control.

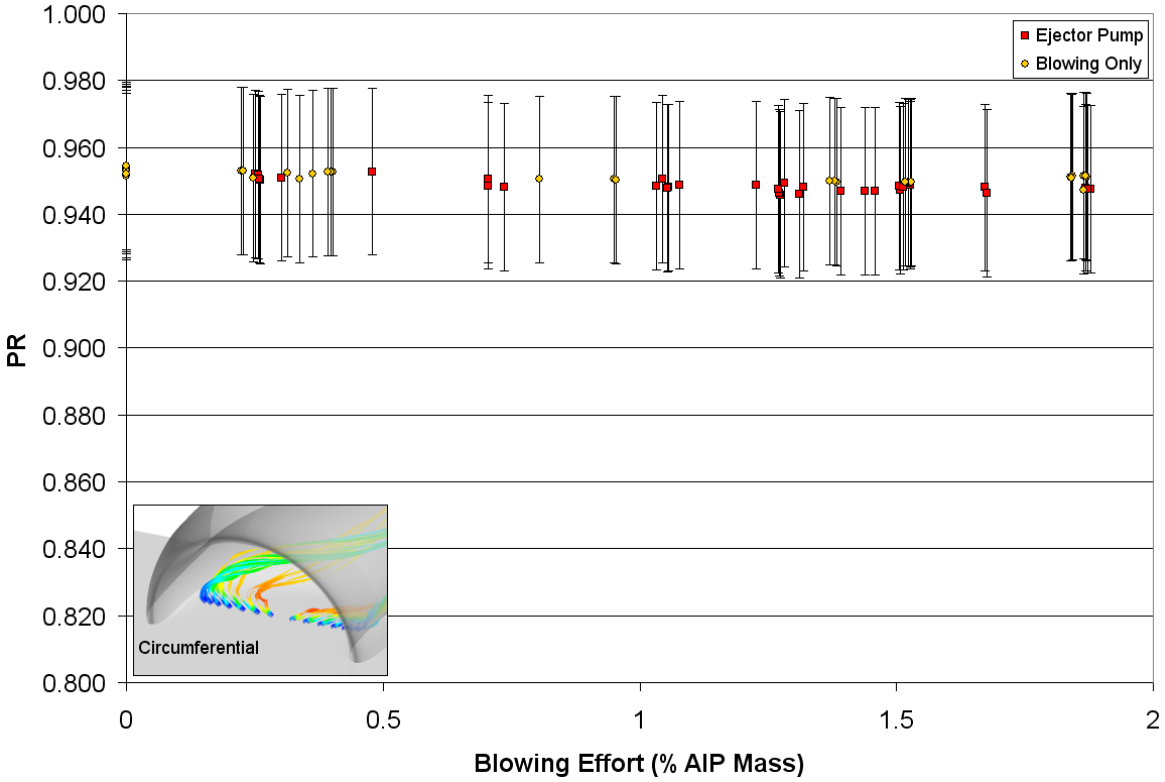

Figure 4.24: Inlet Pressure Recovery Experimental Results - Circumferential Blowing

Conclusions

In order to realize the substantial performance benefits of serpentine BLI diffusers, this study investigated the use of enabling active flow control methods to reduce engine-face distortion. A simulated ejector-pump based system of fluidic actuators was used to directly manage the diffuser secondary flows. This system was modeled computationally using a boundary condition flow control model, and tested in the Techsburg ejector-driven wind tunnel facility.

Active flow control offers substantial performance benefits over passive methods by providing a wide range of flexible, and adaptable control. This control system can achieve significant reductions in engine-face distortion while virtually eliminating the viscous losses created by vane-type vortex generators. Because active flow control systems typically draw motive pressure from the engine compressor, the performance penalties of using compressor bleed air for flow control purposes can limit the amount of air available. Thus, it is necessary to augment jet performance as much as possible. This augmentation was accomplished herein by employing the use of a simulated flow control ejector-pump based system of fluidic actuators that effectively increased jet mass flow with no net increase in required motive air. The performance of these jets was evaluated to identify some of the driving parameters that govern the effectiveness of active flow control methods in serpentine BLI diffusers.

The computational methods and flow control modeling techniques used allowed for rapid, accurate analysis of flow control geometries. By utilizing mesh boundary conditions to model the fluidic actuators, extensive gains were made in terms of the number of configurations tested, as well as the accompanying grid construction and computational processing time. These methods contrast with previous studies that have often focused on individual actuator modeling (whether vane or jet-type), or the introduction of vorticity source-terms to the flow field in order to simulate the physical effects of vortex generators: processes that are both time-consuming and cost prohibitive.

Results of the computational analysis confirmed the large potential benefit of adopting fluidic actuators to control flow distortion in serpentine BLI inlets, showing a maximum 71% reduction in flow distortion at the AIP through the use of the Pyramid 1 simulated ejector scheme, and a 68% reduction using the Circumferential simulated

ejector scheme. However, further investigations suggested that achieving practically desirable engine inlet flow conditions is not merely a function of total pressure distortion; the introduction of the flow control effectors also had a profound impact on the amount of flow swirl present at the AIP. The Circumferential simulated ejector scheme successfully reduced the flow swirl by 30%, while the Pyramid 1 simulated ejector scheme increased swirl by 64%. This result suggests that not all flow control configurations will produce desirable engine inlet flow conditions regardless of their effect on total pressure distortion. Upon further examination, it was determined that the critical factor in successfully reducing both total pressure distortion and swirl was the requirement of maintaining jet individuality, and avoiding the creation of large vortices. By using jet configurations that kept the jet flows separate, the flow control was able to redistribute the low momentum fluid around the duct periphery with the most efficiency. And, for this reason, the Circumferential simulated ejector flow control scheme was determined to be the 'best' configuration as it was the only configuration successful in reducing both total pressure distortion and swirl.

Computational results were validated by designing and testing a representative BWB BLI diffuser test section for the Techsburg ejector-based wind tunnel. This facility was capable of simulating the high-altitude, high subsonic Mach number conditions representative of BWB cruise conditions, while substantially reducing the cost and complexity associated with typical tunnel configurations. When the computational and experimental elements were combined, this resulted in the creation of a system capable of investigating the fundamental mechanisms of flow control effectiveness in BLI serpentine diffusers at a fraction of the time and expense required by previous investigations.

The experimental results showed that the computational analysis slightly over-predicts the flow distortion. However, the trends are accurately predicted despite slight variances in freestream Mach number between runs and a slightly lower tested altitude. Although these configurations have not been optimized, with additional work they could likely reduce flow distortion and swirl to within acceptable limits.

References

[1] Liebeck, R. H. "Design of the Blended-Wing-Body Subsonic Transport". AIAA-2002-0002. 2002 Wright Brothers Lecture.

[2] Gridley, M.C., and Walker, S.H.. "Inlet and Nozzle Technology for 21st Century Fighter Aircraft". ASME 96-GT-244, International Gas Turbine and Aeroengine Congress, Brimingham, UK, June 1996.

[3] Smith Jr., L. H. "Wake Ingestion Propulsion Benefit". AIAA Journal of Propulsion and Power. Vol. 9. No. 1. Jan-Feb-1993.

[4] Seddon, J., Goldsmith, E. L.. *Intake Aerodynamics*. 2nd Edition. AIAA Education Series. Reston, VA. 1999.

[5] Guo R. W., Seddon, J.. "Swirl Characteristics of an S-shaped Air Intake with both Horizontal and Vertical Offsets". *Aeronautical Quarterly*, May 1983.

[6] Vakili, A.,Wu, J., Bhat, M., Liver, P.. "Compressible Flow in a Diffusing S-Duct with Flow Separation". Heat transfer and fluid flow in rotating machinery; Proceedings of the First International Symposium on Transport Phenomena, Honolulu, HI, Apr. 28-May 3, 1985.

[7] Bauermeister, W., Roseburg, C., Ip, H.. "727 Airplane Engine Inlet Development". AIAA 1968-0595. 4th Propulsion Joint Specialist Conference. Cleveland, OH. June 10-14, 1968.

[8] Vakili, A., Wu, J., Liver, P.. "Flow Control in a Diffusing S-Duct". AIAA 1985-0524. AIAA Shear Flow Control Conference. Boulder, CO. March 12-14, 1985.

[9] Reichert, B., Wendt, B.. "An Experimental Investigation of S-Duct Flow Control Using Arrays of Low-Profile Vortex Generators". AIAA 1993-0018. AIAA 31nd Aerospace Sciences Meeting and Exhibit. Reno, NV. January 1993.

[10] Anderson, B., Huang, P., Paschal, W., Cavatorta, E.. "A Study on Vortex Flow Control of Inlet Distortion on the Re-Engined 727-100 Center Inlet Duct Using Computational Fluid Dynamics". AIAA 1992-0152. 30th Aerospace Sciences Meeting and Exhibit. Reno, NV. January 6-9, 1992.

[11] Reichert, B., Wendt, B.. "Improving Diffusing S-Duct Performance by Secondary Flow Control". AIAA 1994-0365. AIAA 32nd Aerospace Sciences Meeting and exhibit. Reno, NV. January 1994.

[12] Anabtawi, A., Blackwelder, R., Lissaman, P., Liebeck, R.. "An Experimental Study of Vortex Generators in Boundary Layer Ingesting Diffusers with a Centerline Offset". AIAA 1999-2110. 35th AIAA Joint Propulsion Conference and Exhibit. June 20-24, 1999. Los Angeles, CA.

[13] Gorton, S., Owens, L., Jenkins, L., Allan, B., Schuster, E.. "Active Flow Control on a Boundary-Layer-Ingesting Inlet". AIAA 2004-1203. 42nd AIAA Aerospace Sciences Meeting and Exhibit. January 5-8, 2004. Reno, NV.

[14] Allan, B., Owens, L., Berrier, B.. "Numerical Modeling of Active Flow Control in a Boundary Layer Ingesting Offset Inlet". AIAA 2004-2318. AIAA 2nd Flow Control Conference. June 28, 2004. Portland, Oregon.

[15] Berrier, B., Allan, B.. "Experimental and Computational Evaluation of Flush-Mounted, S-Duct Inlets". AIAA 2004-0764. 42nd Aerospace Sciences Meeting and Exhibit. January 5-8, 2004. Reno, NV.

[16] Der, Jr., J.. "Improved Methods of Characterizing Ejector Pumping Performance". AIAA 1998-0008. 27th Aerospace Sciences Meeting, Reno, NV, January 8-10, 1989.

[17] Anon. SAE-ARP-1420 Revision B. *Gas Turbine Engine Inlet Flow Distortion Guidelines*. January 11, 2001.

[18] *Gridgen*, Software package, Version 15.00 Release 1, Pointwise Inc., Bedford, TX, 2003.

[19] Hall, E., Heidegger, N., Delaney, R.. *ADPAC v.1.0 – User's Manual*. Allison Engine Company, Indianapolis, IN. NASA/CR-1999-206600. February 1999.

[20] Schetz, J.. *Boundary Layer Analysis*. Prentice Hall Inc., Englewood Cliffs, New Jersey, 1993.

[21] Allan, B., Yao, C., Lin, J.. "Numerical Simulations of Vortex Generator Vanes and Jets on a Flat Plate". AIAA 2002-3160. AIAA 1st Flow Control Conference. June 24-26, 2002. St. Louis, Missouri.

[22] Anderson, B., Gibb, J.. "Study on Vortex Generating Flow Control for the Management of Inlet Distortion". *Journal of Propulsion and Power*. Vol. 9, No. 3. May-June 1993.

[23] Fleming, J.. "Wind Tunnel Design Report". Techsburg, Inc. Interim Report, NASA Contract NAS1-03066, April 2005.

[24] Gracey, W.."Wind Tunnel Investigation of a Number of Total-Pressure Tubes at High Angles of Attack Subsonic, Transonic, and Supersonic Speeds". Report 1303 – National Advisory Committee for Aeronautics, Langley Field, Virginia., January 17, 1956.

[25] Figliola, R., Beasley, D.. *Theory and Design for Mechanical Measurements, 3rd Edition*. John Wiley and Sons, Inc. New York, 1991.

Appendix A: Distortion Descriptors

Several distortion descriptors are common throughout the aircraft industry. Many of these descriptors have been in use for several decades and were created long before computational methods were commonplace. Thus, these descriptors were created based on experimental methods. Both of the methods described herein are based upon a standard six arm 30 probe distortion rake, which uses pressure transducers located on arms at various radii corresponding to area-averaged flow sections.

DC(60) and SC(60)

The DC(60) distortion parameters use total pressure data from the rake to calculate a maximum distortion value for a given flow condition. Each rake arm represents a 60° sector of the flow at the AIP. Additional distortion descriptors exist that use both smaller and large angles at which to place rake arms, such as the DC(45), DC(90), and DC(120) parameters. However, in experimental work, each rake arm also represents a blockage in the flow area. Thus, the angle selected is often based upon acceptable resolution at a minimum of flow blockage. In most cases, the DC(60) and DC(45) parameters are adopted.

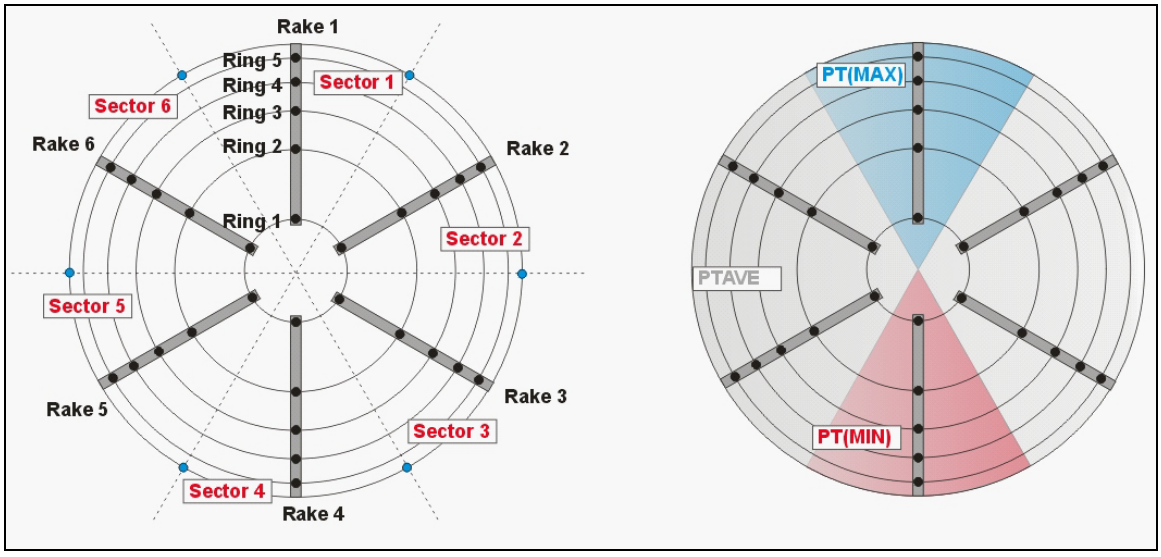

Figure A.0.1: DC(60) Distortion Rake

For total pressure distortions, the rake is used to obtain the average total pressure for each sector, and is then compared to the maximum and minimum sector values. This yields a maximum total pressure distortion that a blade of the compressor would be subjected to

during a complete revolution. However, some variation exists in these descriptors; some groups prefer to non-dimensionalize the pressure difference by the average total pressure at the AIP, and some prefer to non-dimensionalize by the average dynamic pressure. There are advantages and disadvantages to each formulation. By using the AIP average total pressure, the descriptor is less sensitive to changes in flow rate and duct area. However, by using the average AIP dynamic pressure, the distortion values examine an average deficit of flow energy. In this study, both values are calculated.

$$DC(60)_{PT} = \frac{PT_{MAX} - PT_{MIN}}{PT_{AVE}} \tag{A-1}$$

$$DC(60)_{q} = \frac{PT_{AVE} - PT_{MIN}}{q_{AVE}} \tag{A-2}$$

Where PT_{AVE} is the average total pressure at the AIP, PT_{MAX} is the maximum average total pressure over a 60° sector, PT_{MIN} is the minimum average total pressure over a 60-degree sector, and q_{AVE} is the average flow dynamic pressure at the AIP.

The swirl counterpart for the DC(60) distortion coefficient is the SC(60) swirl coefficient. The relationship between total pressure and flow swirl was quantified by Guo[5], who formulated a descriptor in order to correlate the two distortion values. This factor evaluates the severity of the cross-flow velocities at the AIP. These velocities are equivalent to the secondary flows developed within the duct. The SC(60) swirl coefficient is calculated according to:

$$SC(60) = \frac{V_{CF\_MAX} - V_{CF\_MIN}}{V_{AVE}}\ , \tag{A-3}$$

where V_{CF_MAX} represents the maximum average secondary flow over a 60° sector, V_{CF_MIN} represents the minimum average secondary flow over a 60° sector, and V_{AVE} represents the average flow velocity at the AIP. This parameter can be used to highlight the possible severity of local non-axial flow vectors, and thereby highlight the possibility of compressor blade stall.

SAE-ARP1420

The ARP1420 distortion descriptor was originally designed to minimize the risk of inlet and engine compatibility problems arising from total pressure distortion.[17] The standard examines both circumferential and radial distortion and is used to characterize the type of flow distortion, including distortion extent and intensity.

Circumferential Distortion Extent

The circumferential distortion extent (θ_i^-) is defined by the sector of flow (in degrees) that has a total pressure less than the ring average total pressure. Extend is calculated by:

$$Extent = \theta_i^- = \theta_{2i} - \theta_{1i} \qquad \text{(A-4)}$$

as referenced in Figure A.0.2. Where $(PAV)_i$ is the ring averaged total pressure, $(PAVLOW)_i$ is the ring average total pressure of the low pressure extent, and $\theta_{2i,1i}$ are the circumferential location in degrees.

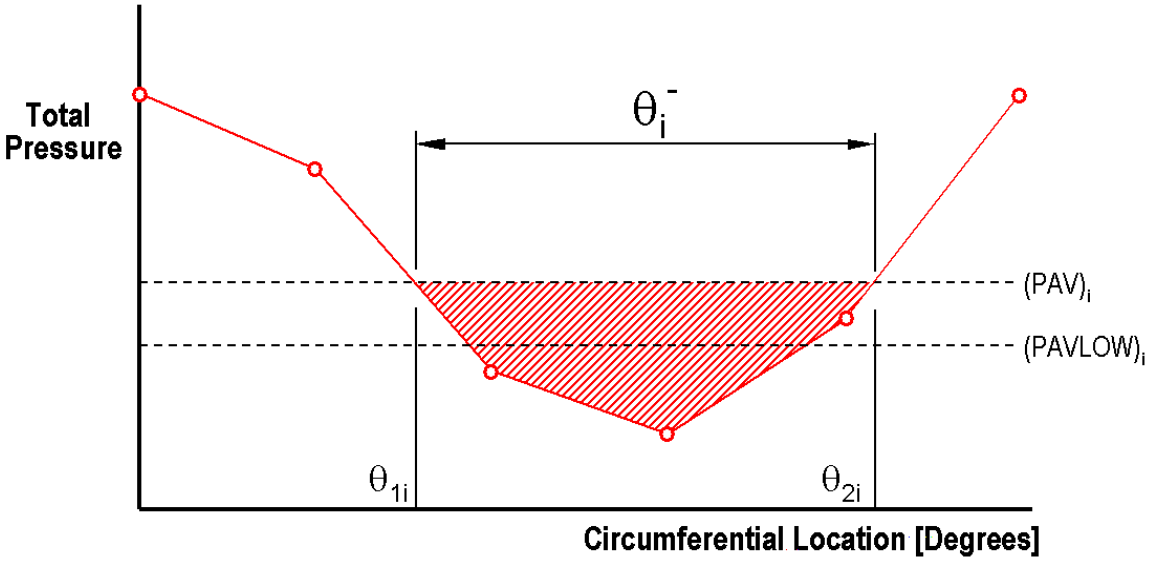

Figure A.0.2: Ring Circumferential Distortion Extent (One-per-Revolution)

Circumferential Distortion Intensity

The circumferential distortion intensity represents the average total pressure difference of each individual ring non-dimensionalized by the ring averaged total pressure. It also gives an indication of the radial location at which the distortion is a maximum.

$$Intensity = \left(\frac{\Delta PC}{P} \right)_{Ring\ i} = \frac{PAV_{Ring\ i} - PAVLOW_{Ring\ i}}{PAV_{Ring\ i}} \qquad \text{(A-5)}$$

Circumferential Distortion Extent: Multiple per Revolution

In many cases, flow distortion is not confined to a singular disturbance within the duct. A typical military configuration utilizes twin serpentine inlets mounted on either side of the fuselage. In such situations it is not uncommon for multiple low energy regions to form.

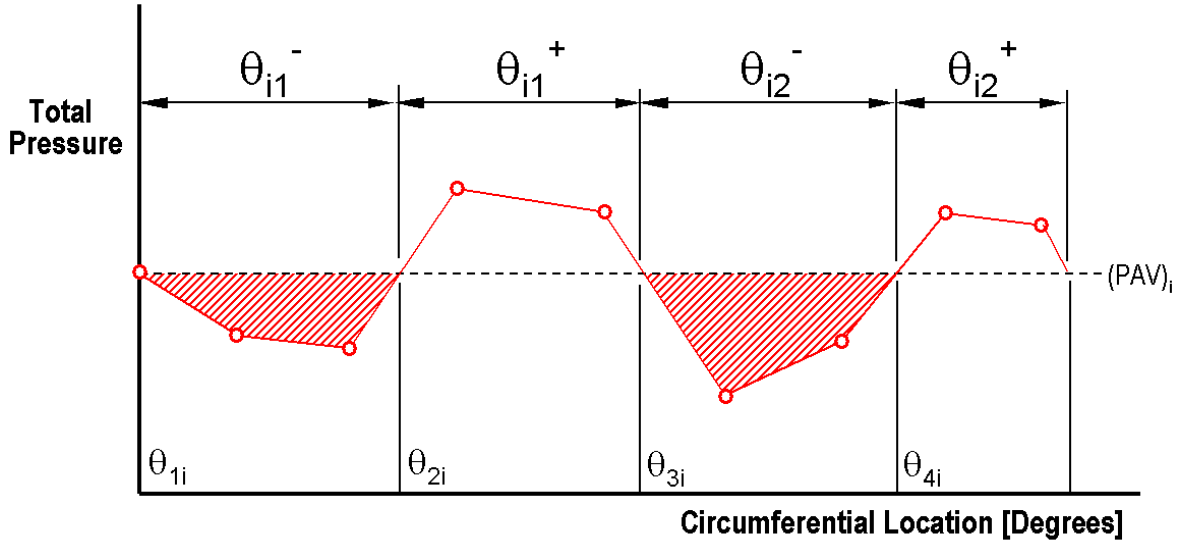

Figure A.0.3: Ring Circumferential Distortion Extent (Multiple-per-Revolution)

The analytical expressions are thus altered to account for the k^{th} low pressure region for Q low-pressure regions per ring, yielding:

$$Extent = \theta_i^- = \sum_{k=1}^{Q} \theta_{ik}^- \qquad \text{(A-6)}$$

$$Intensity = \left(\frac{\Delta PC}{P} \right)_{Ring\ i} = \frac{\sum_{k=1}^{Q} \left[\left(\frac{\Delta PC}{P} \right)_{ik} \theta_{ik}^- \right]}{\sum_{k=1}^{Q} \theta_{ik}^-} \qquad \text{(A-7)}$$

It should be noted however, that if the low-pressure regions are not separated by more than 25 degrees, they should be treated as a one-per-revolution distortion.

Radial Distortion Intensity

The radial distortion intensity represents the total pressure distortion in a direction aligned with the spanwise length of a compressor blade. A typical distribution is shown in Figure A.0.4, and is calculated from:

$$Intensity = \left(\frac{\Delta PR}{P} \right)_{Ring\ i} = \frac{PFAV - PAV_{Ring\ i}}{PFAV} \qquad \text{(A-8)}$$

Where $PAV_{Ring\ i}$ is the ring-averaged total pressure, and PFAV is the area-weighted face-average total pressure.

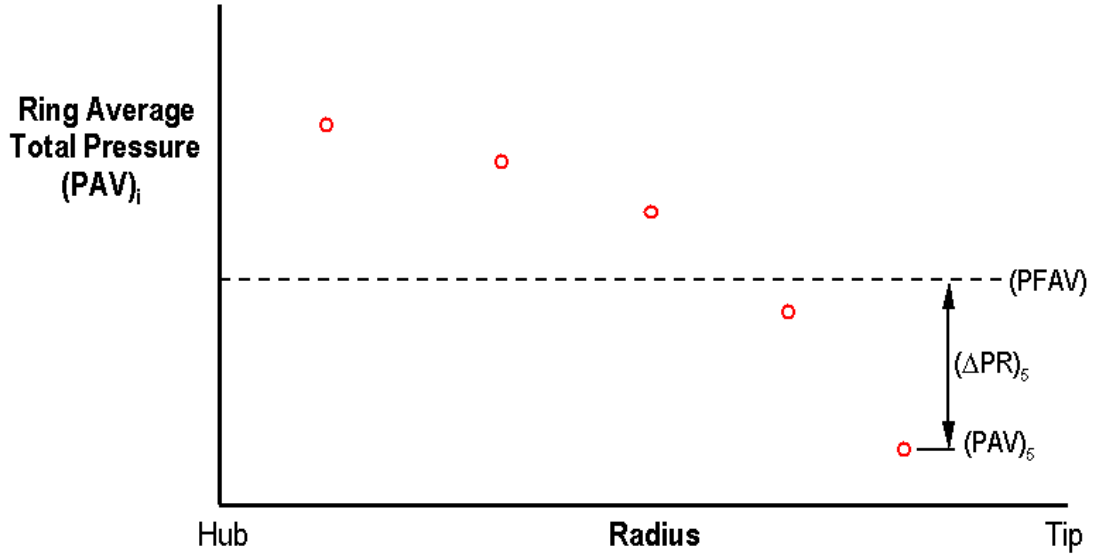

Figure A.0.4: Radial Distortion

Average Distortion Intensity: DPCP

Average distortion intensity ($DPCP_{avg}$) can be defined by averaging the ARP1420 circumferential distortion results according to:

$$DPCP_{avg} = Intensity_{avg} = \sum_{i=1}^{5} \frac{PAV_{Ring\ i} - PAVLOW_{Ring\ i}}{PAV_{Ring\ i}} \qquad \text{(A-9)}$$

This gives an overall area-weighted value for the AIP circumferential distortion intensity that can then be compared to other engine or duct configurations.

Inlet Pressure Recovery

The inlet diffuser represents an integral part of the engine system design. Because the engine needs to accept relatively low velocity, high-pressure flow, the efficiency of the diffuser has a profound impact on overall propulsive efficiency. Inlet pressure recovery is generally considered to represent the efficiency of the diffuser in providing flow to the AIP by accounting for losses incurred from the freestream condition.[4]

$$PR = \frac{AIP\ Total\ \ pressure}{Freestream\ Total\ \ pressure} \tag{A-10}$$

The implication of increasingly complex serpentine diffusers has had an impact on diffuser pressure recovery. Since stealth observability has come to the forefront of the design process, there has been a corresponding decrease in the importance of diffuser pressure recovery. Although it is important to maintain high pressure recovery, the necessity of hiding the aircraft from detection is generally considered more important as it has a substantial impact on aircraft survivability as well as operational life-cycle cost. Although the effect of flow control on diffuser pressure recovery will be examined, it does not represent the focus of this study.

Appendix B: Geometry

The diffuser geometry used throughout this study was defined through joint NASA/Boeing investigations. A standard model was chosen by NASA and Boeing from several generic geometries in order to represent a typical boundary layer ingesting serpentine inlet that exhibited the characteristic flow feature, namely, a high flow distortion. This model would then be used as a generic representation in all subsequent flow analyses. The configuration chosen was inlet configuration 'A', represented in Figure B.0.1.

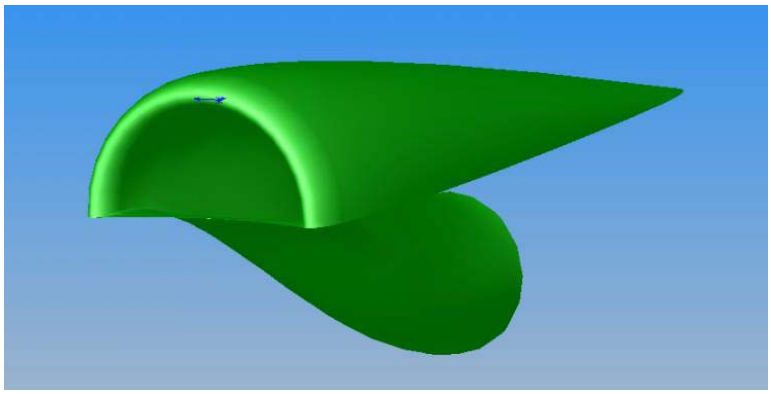

Figure B.0.1: NASA/Boeing BLI Inlet Configuration 'A'

The geometry of the chosen configuration, dimensions, and the critical design parameters of the inlet are outlined in Figure B.0.2 and Figure B.0.3.

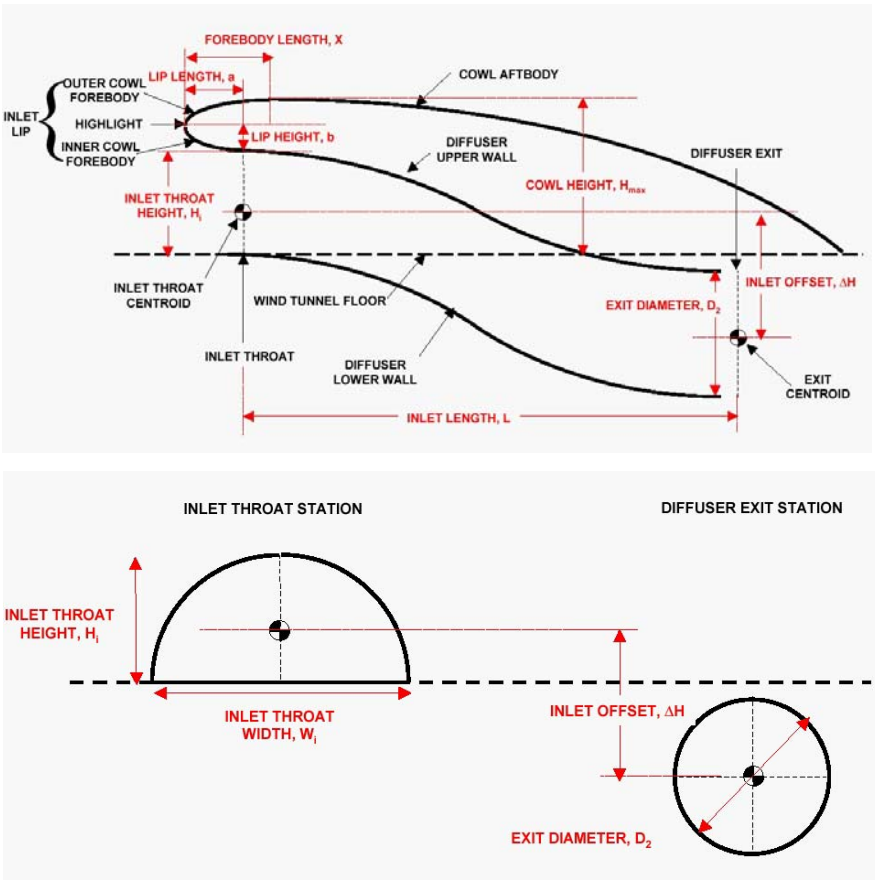

NASA Inlet "A" geometry:

- Diffuser Exit to Inlet Area $A_2/A_i = 1.069$
- Diffuser Length to Exit Diameter Ratio $L/D_2 = 5.97$
- Rounded nacelle lip (length/thickness = 2)

Figure B.0.2: NASA Configuration 'A' Diffuser Geometry

As can be seen above, the diffuser has an aggressive inlet offset height, which will cause strong transverse pressure gradients across the duct's cross section, and thus strong secondary flows to form. The severity of the diffuser curvature will also lead to a boundary layer that could be prone to separation in regions of strong adverse pressure gradients. The diffuser also has a low exit to inlet area ratio due to the decreased necessity for diffusion as a result of a large amount of ingested low-energy fluid.

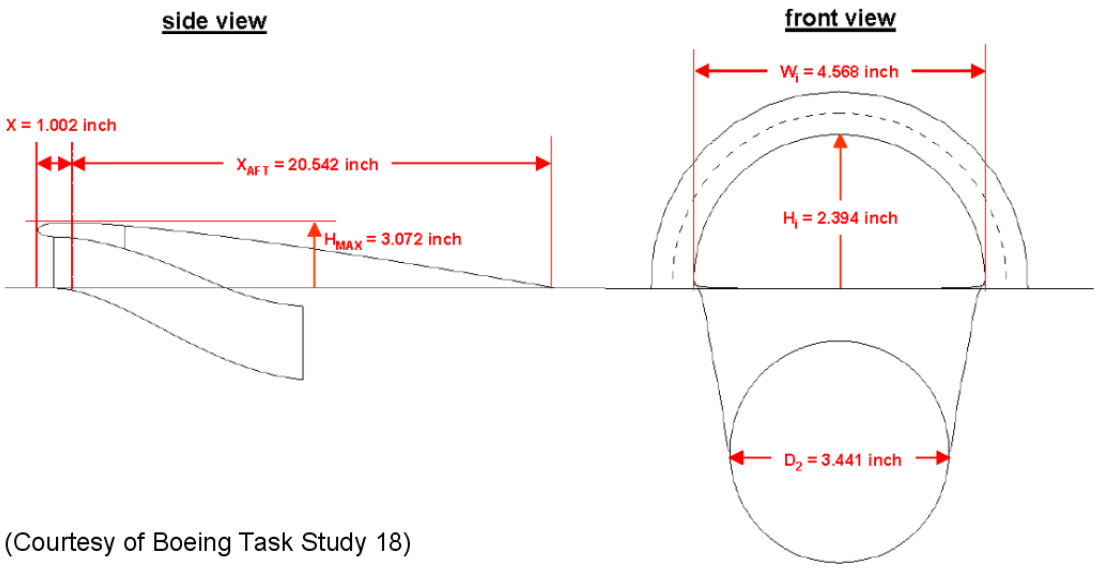

(Courtesy of Boeing Task Study 18)

Figure B.0.3: NASA/Boeing Configuration 'A' Dimensions

The above dimensions represent the size and configuration of the nacelle used in a NASA cryogenic wind tunnel test at the Basic Aerodynamics Research Facility (BART) at NASA Langley.[13] All subsequent representations of the diffuser are in accordance with the above geometry.

Appendix C: Grid Resolution Study

A grid resolution study was conducted on the baseline CFD solution by examining the solution dependency on the mesh size. Three different mesh densities: fine, medium, and coarse were generated. Each successive coarsening resulted in a reduction of the number of cells by ½ in each direction. Therefore, the number of cells for the fine, medium, and coarse meshes span roughly two orders of magnitude (1, 1/8, and 1/64). The distortion parameters were monitored for all three cases and compared for a measure of the grid independence.

Agreement was seen for most flow data between the medium and fine grids, indicating that some measure of grid independence had been achieved. The values for the calculated quantities (DC(60) values, etc.) agreed very closely between the medium and fine mesh cases, as did the total pressure contour results. Sample results for the average total pressure along the inlet for the different mesh densities are given in Figure C.0.1, again displaying very good agreement between the medium and fine grid cases.

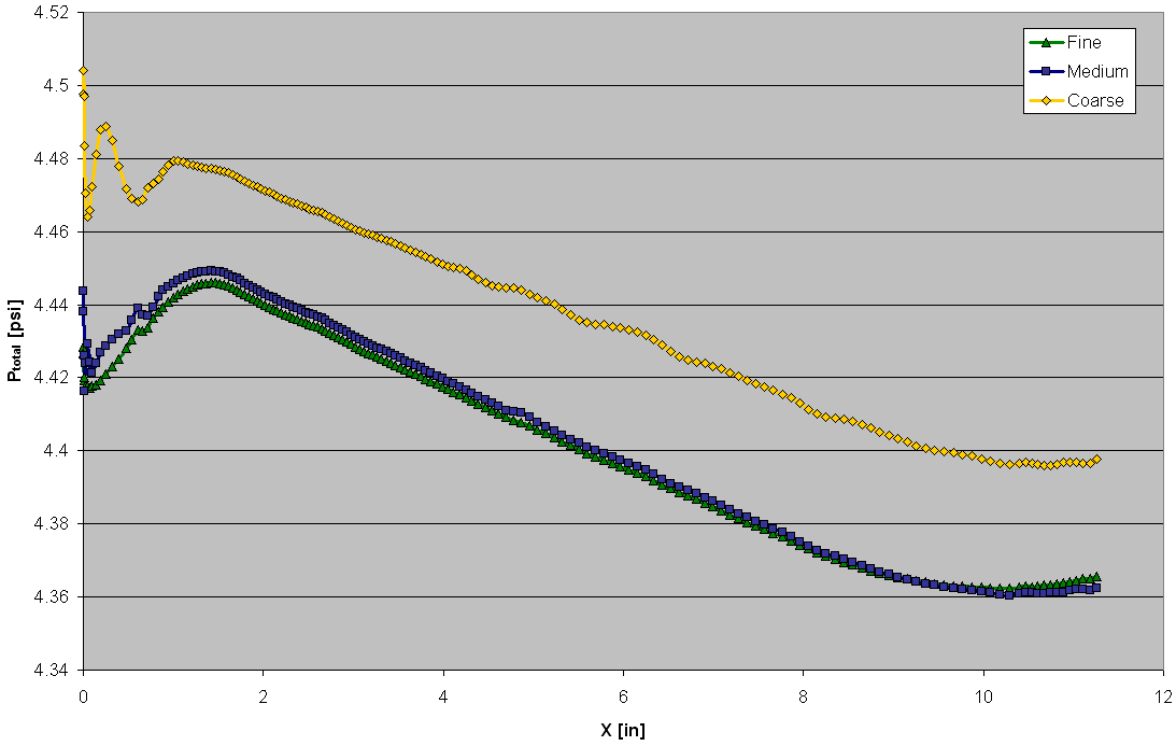

Figure C.0.1: Grid Resolution Study - Baseline Total Pressure Distribution

Figure C.0.2 and Figure C.0.3 show convergence results for the DC(60) and DPCPavg parameters respectively. These parameters are correlated according to the inverse of the number of cells. Thus, it was possible to project what the distortion result would be for an infinite number of cells. As seen in these figures, an increase in the number of cells is not likely to create a large difference in solution accuracy. The leveling out of the distortion numbers also suggests that the possible increase in accuracy will be very small compared to the large increase in required computational time associated with an increase in mesh resolution.

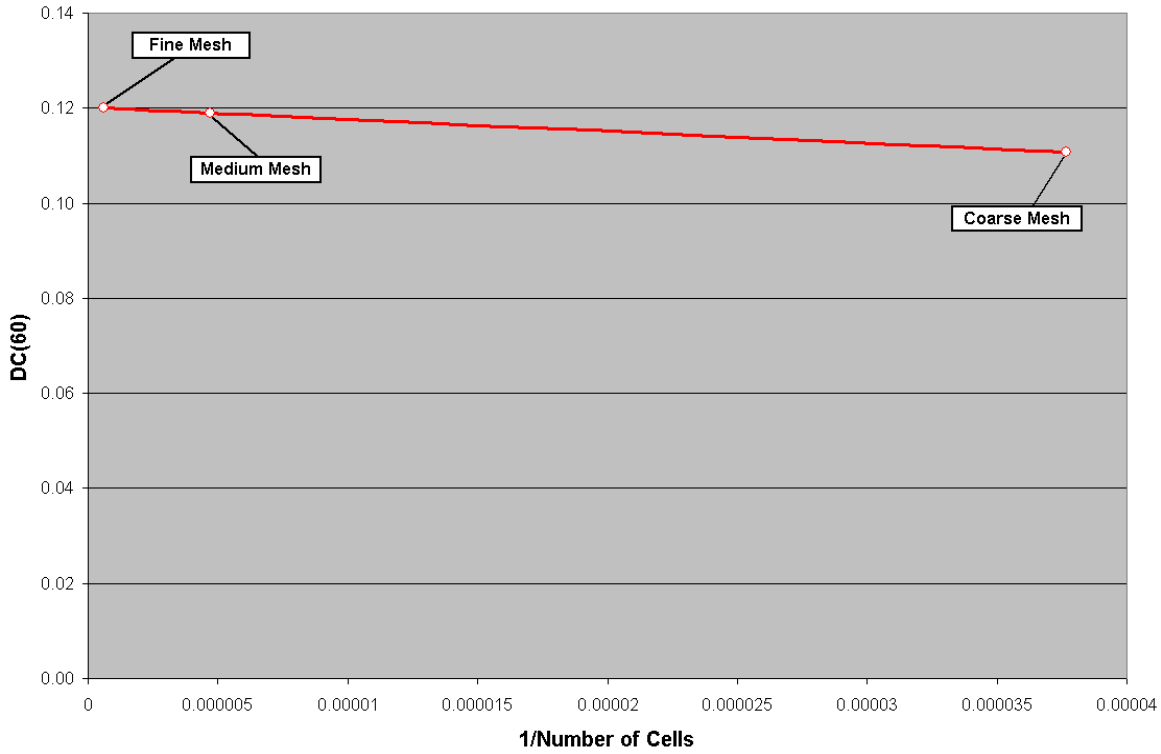

Figure C.0.2: Grid Resolution Study - Baseline DC(60) Convergence

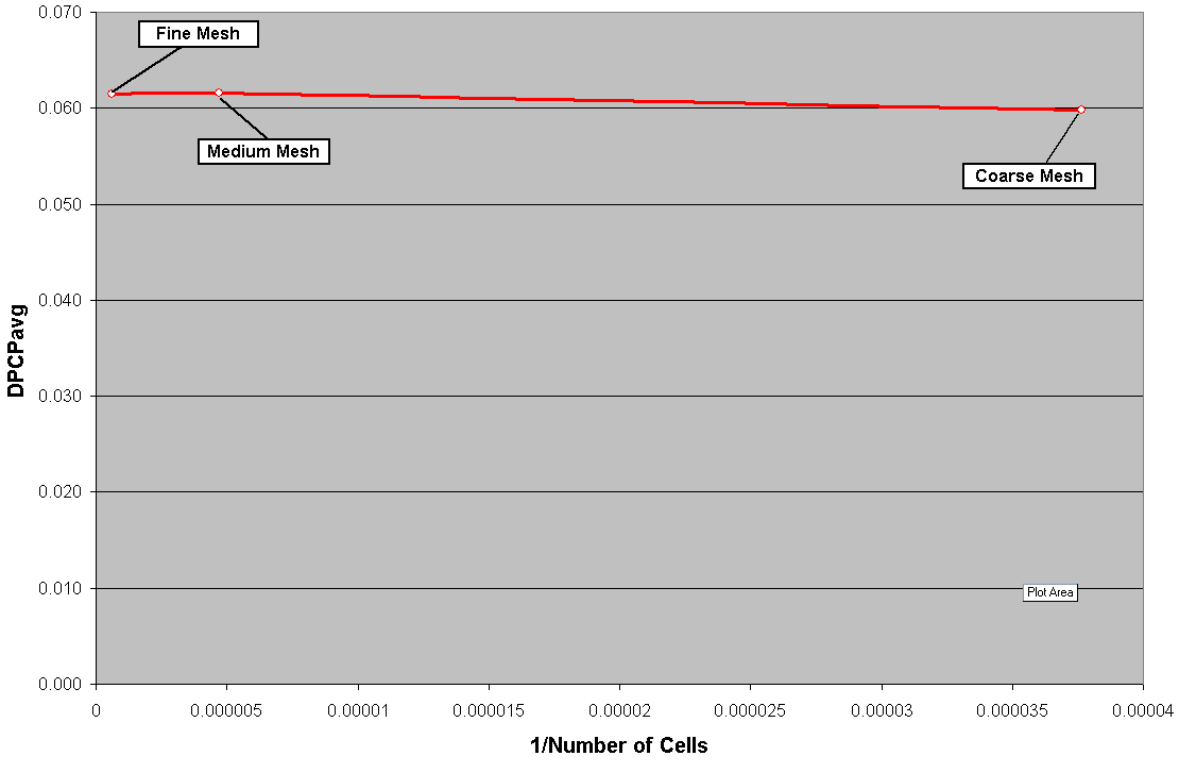

Figure C.0.3: Grid Resolution Study - Baseline DPCPavg Convergence

Figure C.0.4 and Figure C.0.5 examine the grid resolution study results based upon the ARP1420 circumferential and radial intensity distortion results. Results of these studies indicate a significant difference between the fine and coarse results. The medium and fine densities show reasonable agreement and predict the same trends. Results from the DPCPavg which are based upon the circumferential distortion intensities shows good converge as noted in Figure C.0.3. Results therefore suggest that little benefit will be gained by adopting a finer mesh density.

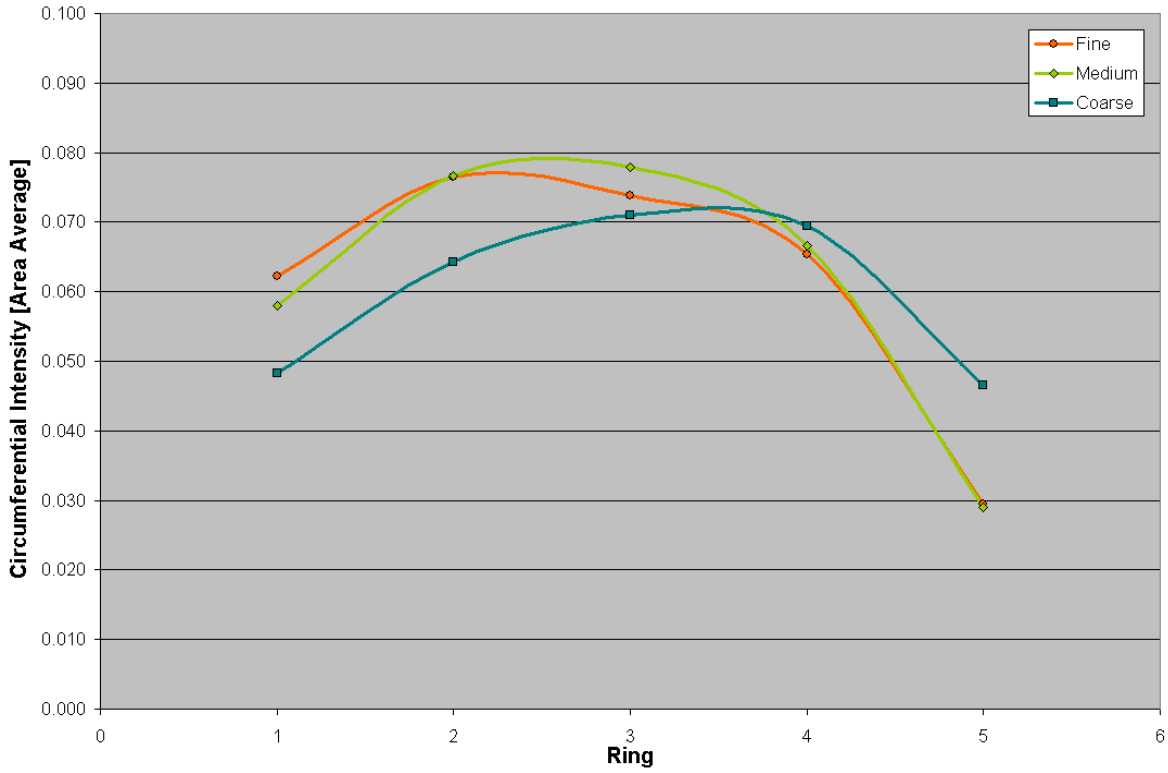

Figure C.0.4: Grid Resolution Study - Baseline Circumferential Distortion Intensity

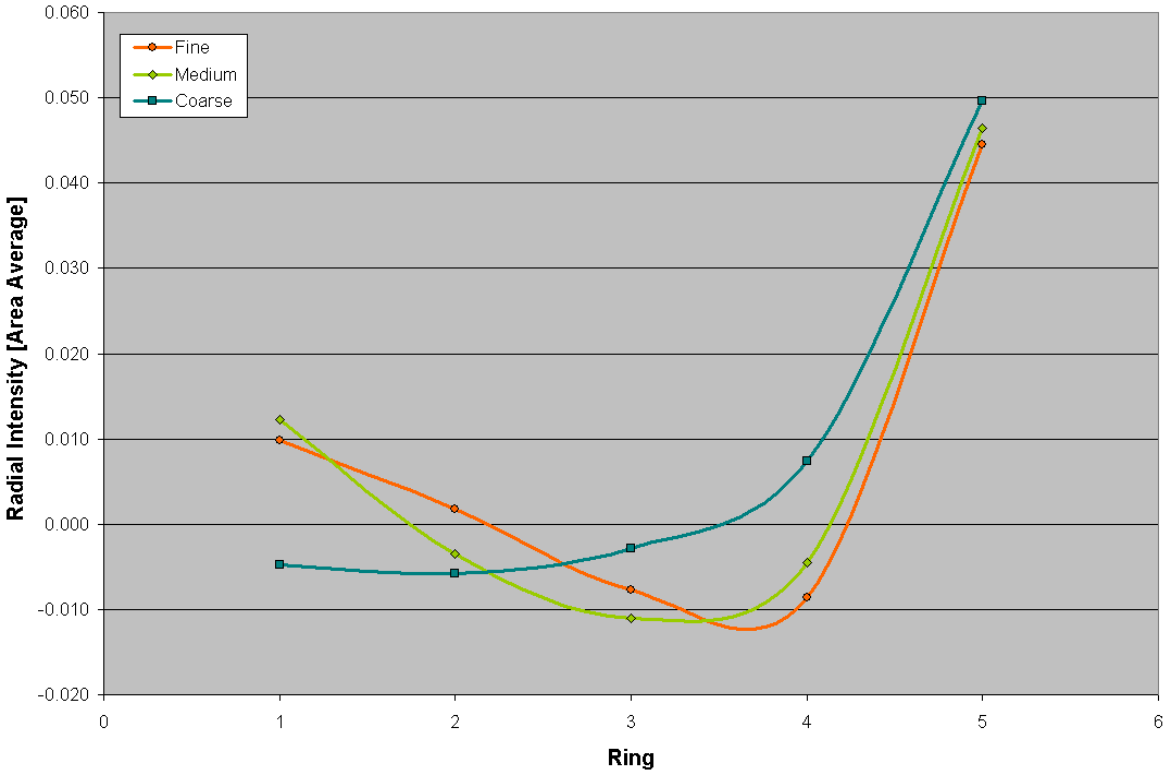

Figure C.0.5: Grid Resolution Study - Baseline Radial Distortion Intensity

Appendix D: Impact of Diffuser Mass Flow on AIP Distortion

In order to facilitate better comparison with results provided by NASA, computational models were run for various engine mass flows. Since the dimensions of the diffuser may vary from test to test, a non-dimensional mass flow value $C\dot{m}$ was used to compare the solutions. This value can be roughly correlated to diffuser capture area, and represents the percentage of freestream air that enters the inlet. The value of the non-dimensional mass flow is calculated by dividing the AIP mass flow by the freestream mass flow through an area equal to the AIP total area:

$$C\dot{m} = \frac{\dot{m}}{\rho_\infty A_{AIP} V_\infty} \qquad \text{(D-1)}$$

The evaluated CFD cases examined six $C\dot{m}$ values ranging from 0.524 to 0.796. The results for these tests are shown below:

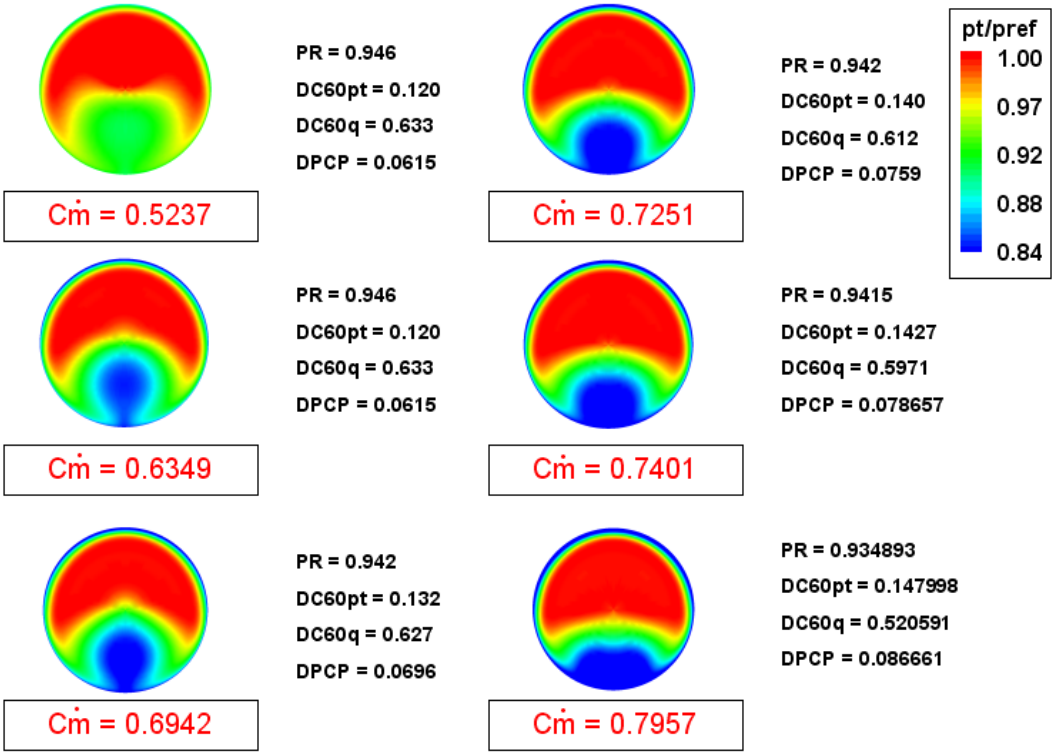

Figure D.0.1: Effect of Variation in AIP Mass Flow

It can be seen that as the mass flow increases (and hence inlet Mach number), the severity of the total pressure distortion also increases. This is demonstrated by the continual increase in DC(60) with increasing mass flow. The total pressure contours show a continually growing region of low momentum fluid buildup along the bottom of the

diffuser. As the AIP mass flow increases, the severity of the total pressure distortion also increases, leading to a greater differential between the high and low momentum fluid regions. In addition, as the engine mass flow increases, the total pressure recovery of the engine decreases.

Results from NASA compare reasonably well with the Techsburg results. Results deviate slightly as expected due to the use of different turbulence models in the CFD analysis. Techsburg solutions used the 1-equation Spalart-Allmaras (S-A) turbulence model while NASA computations used the 2-equation Menter Shear Stress Transport (SST) model. In addition, the NASA mesh used an overset grid topology and over 8 million nodes to model the flow field. Techsburg does not currently have the computational resources to replicate this approach, and thus used a traditional structured grid with no more than 2.6 million nodes. The overall goal of the study was to predict the flow's behavioral trends, and the effect of varying mass flow in the unaltered diffuser. The trends obtained in this study are believed to be accurate in predicting the overall flow behavior. The total pressure contours match well for similar $C\dot{m}$ values as highlighted in Figure D.0.2.

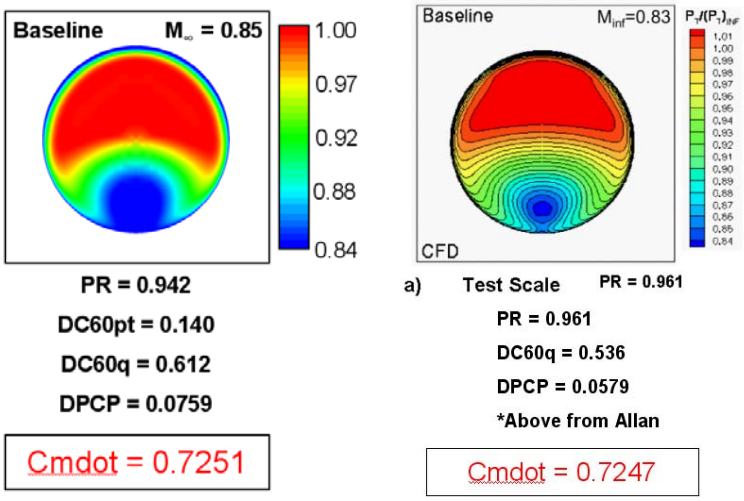

Figure D.0.2: Baseline Comparative Mass Flow Solutions

Appendix E: Flow Control Axial Location

In order to better understand the driving parameters of flow control effectiveness, the flow control array was located in a variety of axial locations. This was accomplished by varying the streamwise (axial) location of the circumferential jet configuration. Jet arrays were located at axial stations of x/L = 0.010, 0.126, 0.170, 0.177, 0.292 as shown in Figure E.0.1.

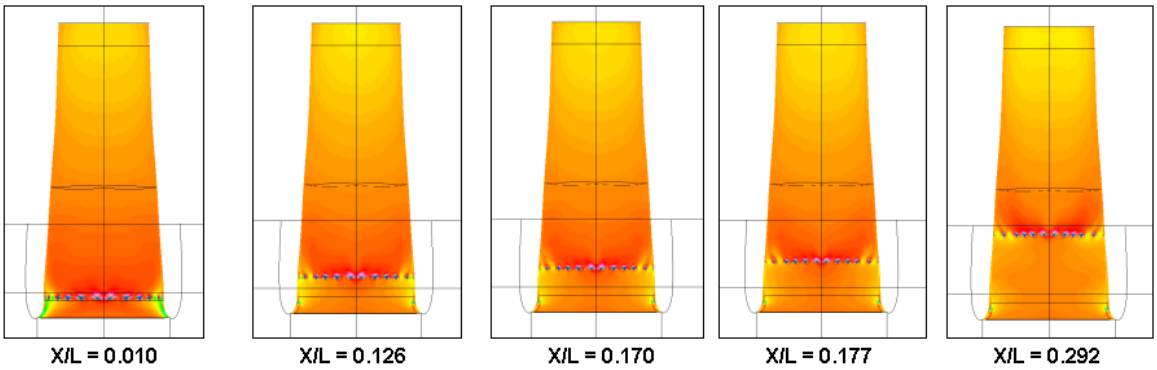

Figure E.0.1: Flow Control Axial Location

At upstream locations, the boundary layer is thinner and the secondary flows are not yet established within the diffuser. As the flow progresses down the diffuser, the centrifugal forces establish a pressure gradient across the flow due to differences in the momentum of the boundary layer and flow of near freestream velocity. These gradients set up the secondary flow patterns commonly associated with offset diffusers. In the case of boundary layer ingesting inlets, the strength of the counter-rotating vortices are further enhanced by the addition of a junction vortex formed by the interaction of the boundary layer with the engine nacelle. Because these vortices have the same sense of rotation as the established secondary flows, the severity of the flow distortion is increased.

Several considerations should be weighed when locating flow control effectors. Logic would dictate that locating flow control at an upstream location would allow the effectors to combat secondary flows before they are established with a minimum of effort. However, studies by Reichert et al.[9] have shown that locating effectors at upstream locations incurs a slight performance penalty, but this penalty is comparatively smaller than the penalty associated with locating effectors too close to flow disturbances. If the effectors are too close to flow disturbances (such as flow separation), they become almost completely ineffective. It should be noted that the specific goal of Reichert's study was to

prevent flow separation in serpentine diffusers, and although the methodology differs from that adopted in this study, the reasoning may still be applicable. In consideration of the ejector pump model, it should be noted that maximum performance of the effectors will be gained if the suction is located in a region of comparatively high pressure and the jets in a region of low pressure. This pressure differential is essential in establishing the maximum benefit of the flow effectors. By placing the suction source at the stagnation point of the nacelle highlight, the maximum benefit may be gained. Also, considerable benefit is gained by locating the jets as near to the suction source as possible, as excessive distances result in high-pressure drop associated with pipe friction losses.

Through judicious placement of the flow control effectors, the overall effectiveness of the jets was investigated. Results shown in Figure E.0.2 suggest that there is an optimum axial location near x/L = 0.17. It is likely the locations farther upstream of this point are not effective due to their proximity to the inlet throat, while downstream locations appear to be less effective due to the increasing strength of secondary flow patterns. These results confirm the findings of Reichert et al.[9], and reinforce the design strategy of managing secondary flows early in the diffuser for maximum effectiveness.

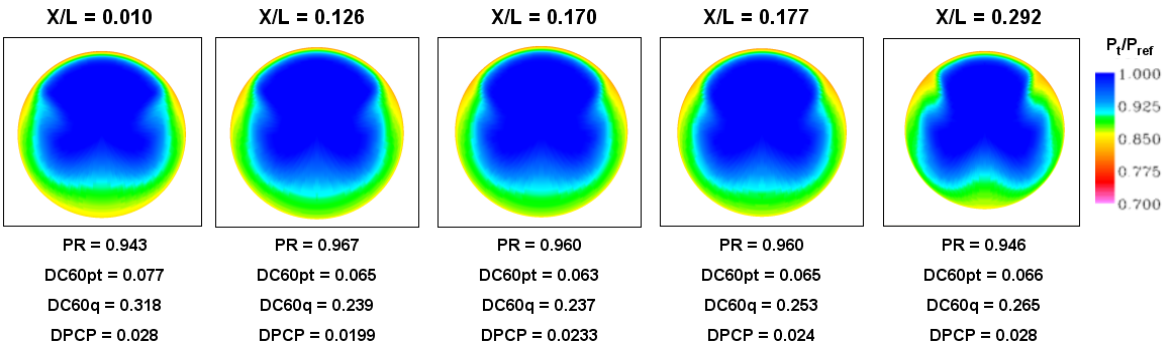

Figure E.0.2: Effect of Axial Jet Location - Total Pressure Contours

Appendix F: Flow Control Spanwise Spacing

Results from the original flow control study showed a performance variation between the circumferential and Pyramid 4 case which had very similar jet configurations. The major variation between these cases was the spanwise jet spacing. The variation in the resulting distortion highlighted the importance of jet interaction, and implied that the circumferential jet spacing had a profound effect on overall configuration performance. Thus, variations in spanwise jet spacing and its effect on AIP distortion was further investigated.

Configurations examined ranged from a very tightly spaced configuration to a well-dispersed configuration. The configuration with the smallest spanwise spacing was located on the diffuser "floor" starting near the duct centerline. (Narrow) The most dispersed configuration had jets spanning a large portion of the diffuser circumference (Wide). In all cases, the total jet array mass was held constant, as was the jet supply pressure; this allowed for a reasonable comparison between obtained results. The examined configurations are shown in Figure F.0.1 with the jet locations indicated.

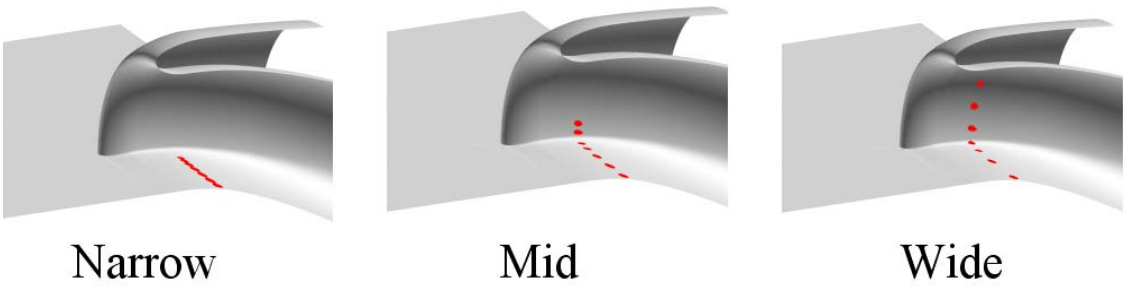

Figure F.0.1: Spanwise Jet Configurations

As seen in Figure F.0.2, altering the spanwise spacing has a strong effect on the management of total pressure distortion at the AIP. For both of the examined DC(60) parameters, the distortion decreased with each subsequent reduction in spanwise jet separation. Thus, the "Narrow" configuration produced the best results in terms of a reduction in the maximum "worst-case" sector distortion.

The DPCPavg parameter suggests that the average distortion intensity is relatively constant until the jets are no longer effect in counteracting the secondary flows. The difference between values from the Mid and Wide configurations is much greater than differences between the Narrow and Mid configurations. However, the general trend is the same as predicted by the DC(60) parameters.

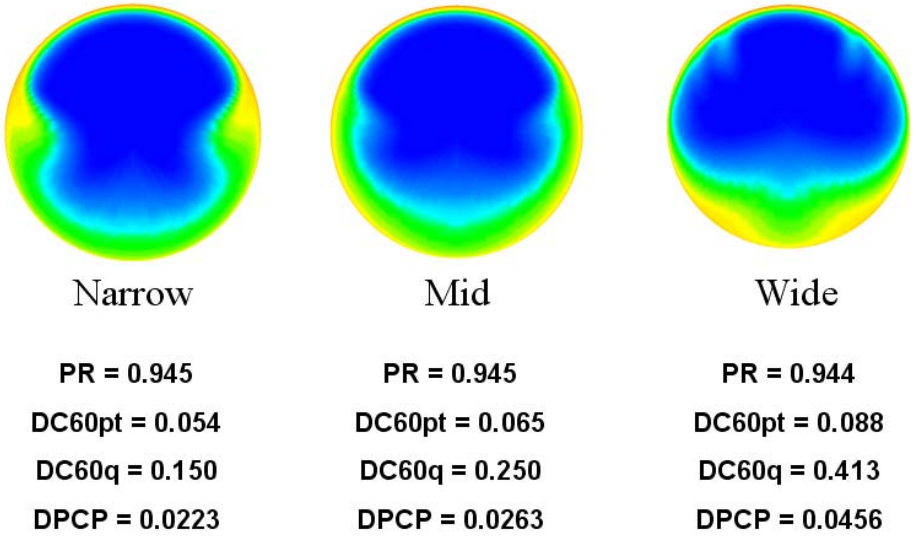

Figure F.0.2: Effect of Jet Circumferential Spacing

Figure F.0.3 shows the streamwise vorticity contours at the AIP for the investigated spanwise spacing flows. Here it can been seen that for the most closely-spaced jet configurations, the resultant vorticity at the AIP is much more concentrated than for the most dispersed jet cases. Visual contours suggest that the jets in the Narrow configuration produced a single vortex of higher strength, while more spaced configurations produced several vortices of lower magnitude. (Vortices resulting from the upper wall jets can be seen in the Wide configuration.) Trends suggested by visual contours are confirmed by the SC(60) swirl parameter, which suggests an increase in AIP swirl proportional to a decrease in jet spacing. The induced swirl can be highly detrimental to engine performance as it can lead to local stalling of compressor blades and eventually to engine surge. Thus, selection of an appropriate flow control solution for each specific case should be based upon engine performance requirements; engines that

can tolerate a larger swirl velocity can obtain increased benefit from a further decrease in total pressure distortion. In reality, the increased vorticity is likely to result in the acceptance of a slight penalty in total pressure distortion in order to obtain acceptable levels of swirl. Thus, for an individual engine, an optimal configuration can be determined for a given jet total pressure.

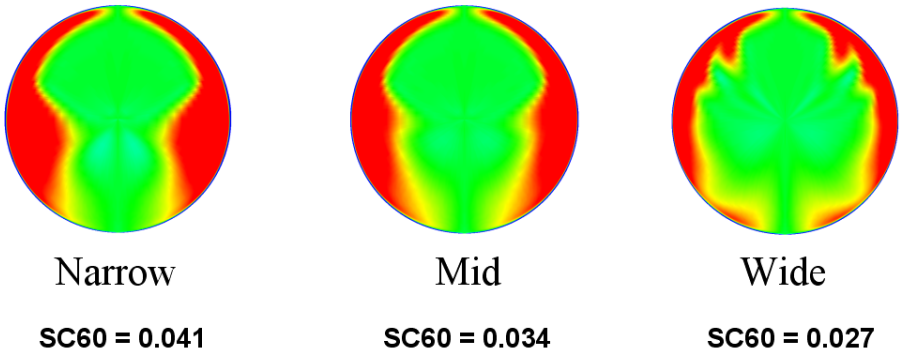

Figure F.0.3: AIP Streamwise Vorticity - Effect of Spanwise Jet Spacing

Appendix G: Complete CFD Results

The section details the results for all investigated flow control cases, and presents AIP total pressure contours and distortion parameters for obtained solutions.

Baseline ARP1420 Distortion Parameter Results

In examining the AIP distortion descriptors, it was seen that the regions with the highest circumferential distortion intensities were rings 2 and 3, located near the hub of the engine (Figure G.0.1). These center circumferential rings encapsulate both the center of the vortex formed by secondary flows and a section of the undisrupted high momentum core flow. The maximum intensity is due to the large difference in total pressure between the upper duct "core" flow and the low momentum region at the bottom half of the duct.

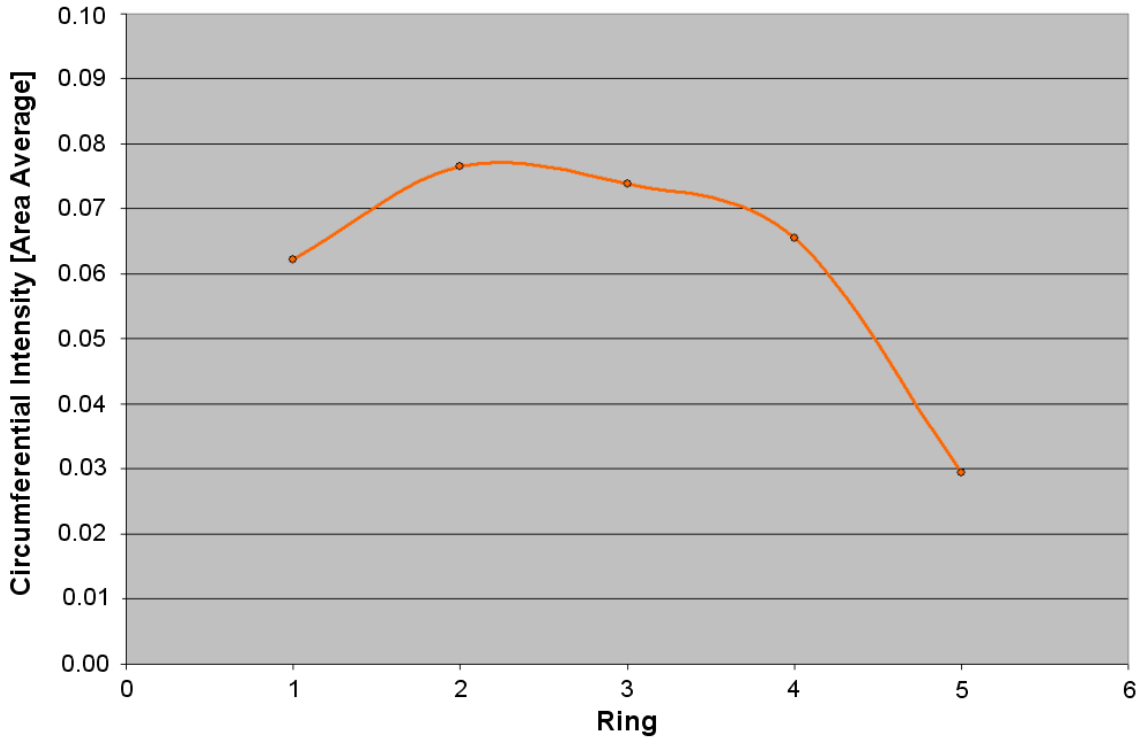

Figure G.0.1: Circumferential Distortion Intensity – Baseline

The largest radial distortion results were for ring 5, at the outer edge of the AIP (Figure G.0.2). This is expected due to the inlet wall boundary layer growth at the AIP.

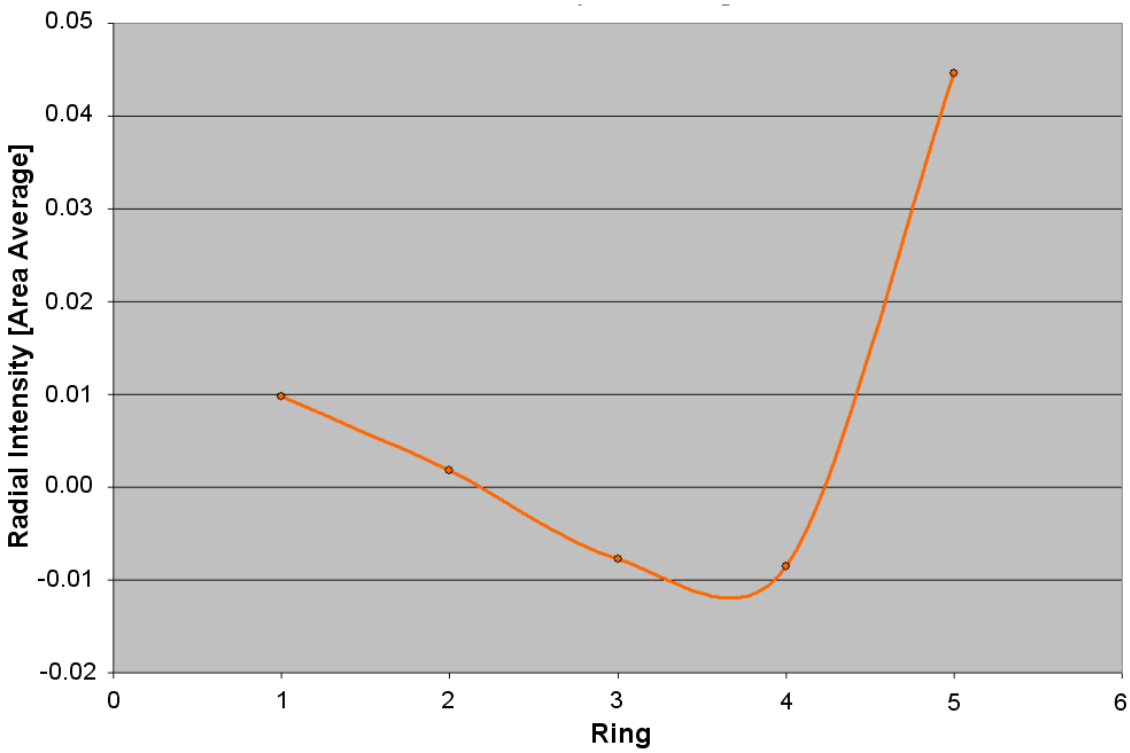

Figure G.0.2: Radial Distortion Intensity – Baseline

Flow Control Case Descriptions

- **Baseline:** Baseline Solution - no flow control

Blowing Only ('Traditional' Configuration, Jet mass flow ~1% AIP total):

- **Cir (1%):** Circumferential Blowing Scheme
- **Pyr1 (1%):** Pyramid 1 Blowing Scheme

Blowing Only (Jet mass flow ~2% AIP total):

- **Circ. Blow:** Circumferential jet arrangement
- **Axial 1:** Jets arranged in an axial (streamwise) line near outer edge of diffuser 'floor'
- **Axial 2:** Jets arranged in an axial line (streamwise) near center of diffuser 'floor'
- **Pyramid 1:** Jets arranged in a row at an angle to the oncoming flow (most acute angle)

- **Pyramid 2:** Jets arranged in a row at an angle to the oncoming flow (intermediate angle)
- **Pyramid 3:** Jets arranged in a row at an angle to the oncoming flow (intermediate angle)
- **Pyramid 4:** Jets arranged in a row at an angle to the oncoming flow (almost perpendicular)

Suction Only (Suction mass flow ~1% AIP total):

- **Suction:** 'Lip' suction - suction located at stagnation point on inlet lip and diffuser 'floor'
- **Suction2:** 'floor' suction - located along diffuser floor in line with diffuser highlight

Ejector Pump Models (Jet mass flow ~2%, suction mass flow ~1% AIP total):

- **FSCIR:** Floor suction combined with circumferential blowing scheme
- **FSA2:** Floor suction combined with axial 2 blowing scheme
- **FSP1:** Floor suction combined with Pyramid 1 blowing scheme
- **FSRP:** Floor Suction combined with the 'reversed' Pyramid 1
- **SRP:** Lip Suction combined with a 'reversed' Pyramid 1 arrangement
- **SCIR:** Lip Suction combined with circumferential blowing scheme
- **SP1:** Lip Suction combined with Pyramid 1 blowing scheme
- **SA2:** Lip Suction combined with Axial 2 blowing scheme

Flow Control ARP1420 Distortion Results

As can be seen in Figure G.0.3, the baseline case (no flow control) has the highest circumferential distortion for each ring of the distortion rake as compared to all examined cases. The conventional blowing schemes show a clear reduction in circumferential distortion, with the Pyramid1 case showing the largest reduction. However, it should be noted that although the values for the Pyramid 1 case are lower than the circumferential case, the relative change in distortion between circumferential locations is more localized along the blade radius. The circumferential case, although displaying a higher distortion, is more even in its distribution for different rings, which is more likely to produce a more uniform distortion distribution.

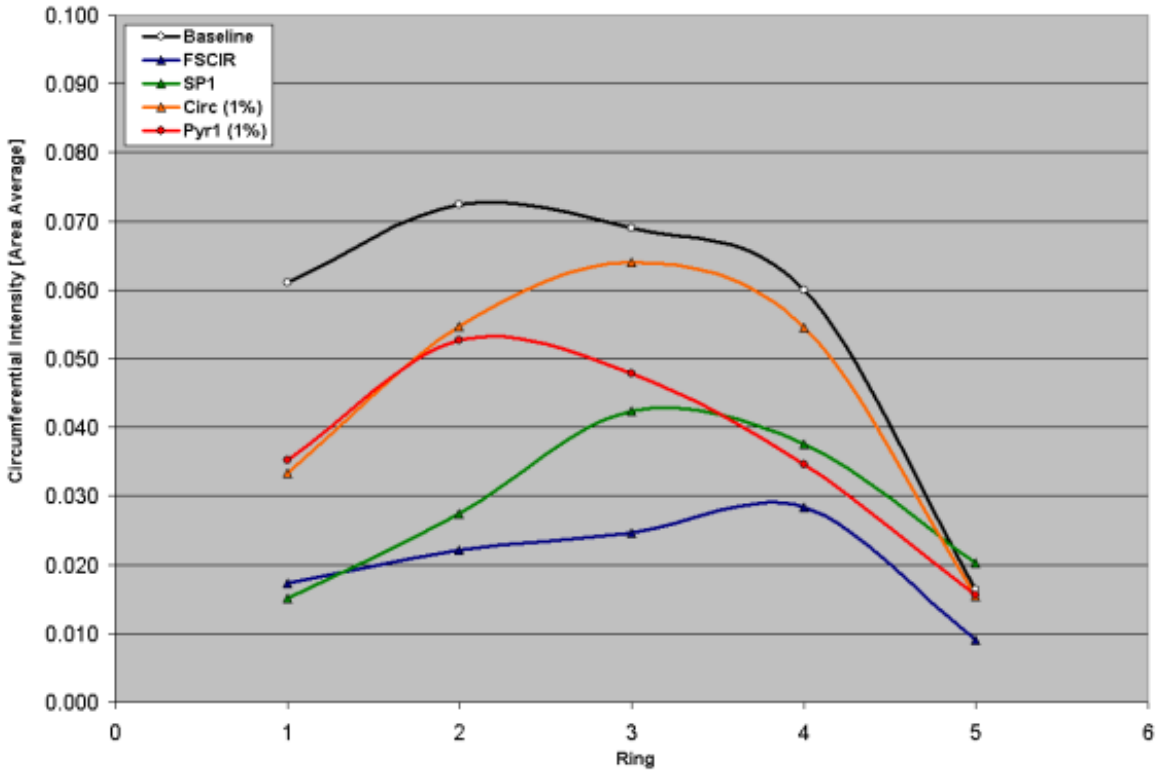

Figure G.0.3: ARP1420 Circumferential Distortion Intensity (Selected Cases)

The radial distortion plot shows a baseline with a very large distortion that changes quickly in the radial direction. All other cases in Figure G.0.4 show a much more gradual distortion profile in the radial direction. This gradual change is a good indicator

that the flow distortion has been distributed, and is likely to produce more steady engine operation. However, note that the conventional blowing cases (Circ (1%) and Pyr1 (1%)) are not as even in their distribution of the distortion; the ejector based models (FSCIR and SP1) show a near-linear distribution in the radial direction.

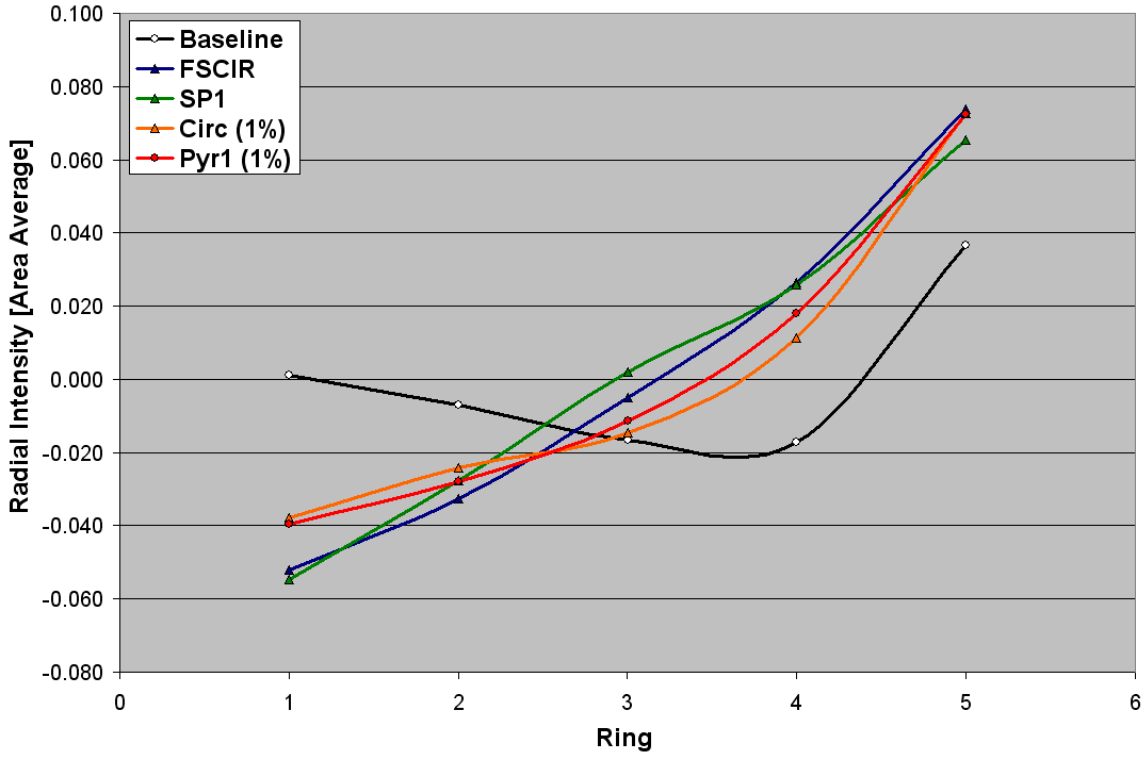

Figure G.0.4: ARP1420 Radial Distortion Intensity

Flow Control Solution Contours

This section shows contour plots for all obtained flow control solutions. Contours from left to right are AIP total pressure, secondary flow magnitude, and streamwise vorticity.

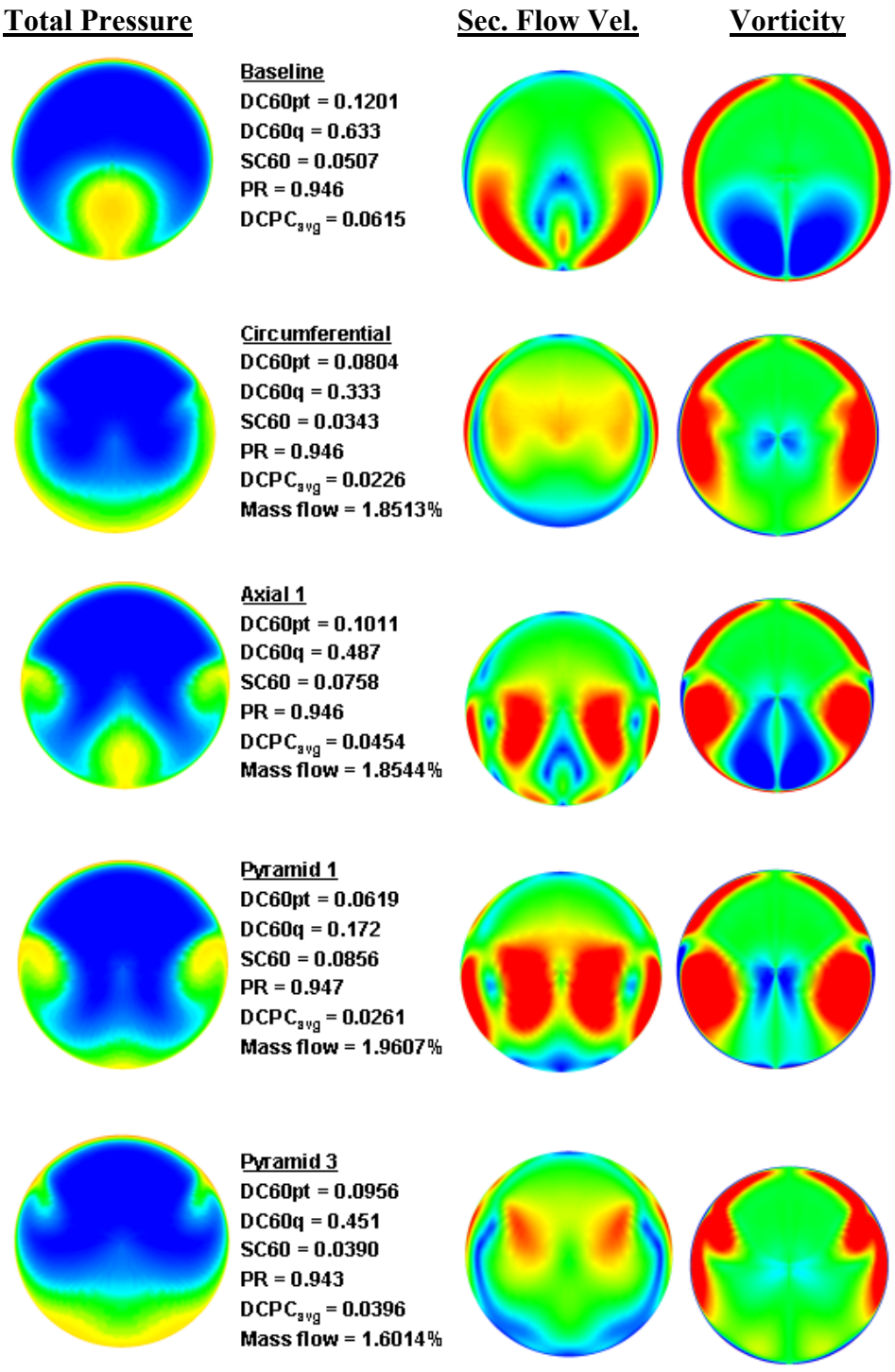

Total Pressure		Sec. Flow Vel.	Vorticity
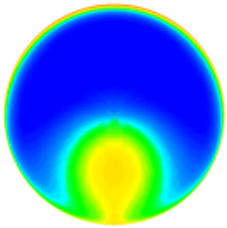	**Suction** DC60pt = 0.1187 DC60q = 0.631 SC60 = 0.0506 PR = 0.947 $DCPC_{avg}$ = 0.0613 Mass flow = 1.0175%	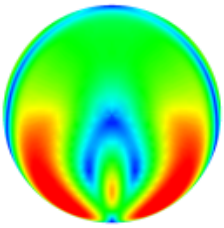	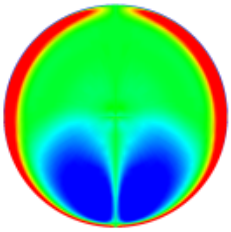
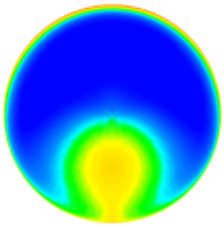	**Floor Suction** DC60pt = 0.1189 DC60q = 0.632 SC60 = 0.0506 PR = 0.947 $DCPC_{avg}$ = 0.0622 Mass flow = 0.25%	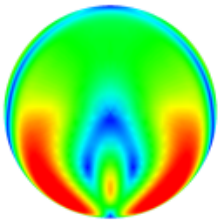	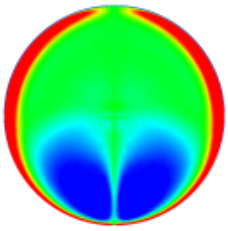
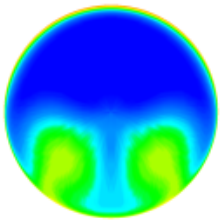	**Axial 2** DC60pt = 0.0860 DC60q = 0.342 SC60 = 0.0600 PR = 0.945 $DCPC_{avg}$ = 0.0368 Mass flow = 2.0374%	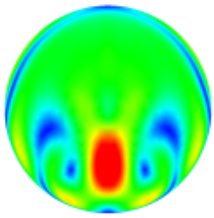	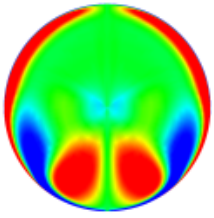
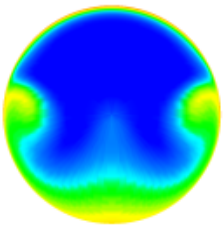	**Pyramid 2** DC60pt = 0.0862 DC60q = 0.375 SC60 = 0.0761 PR = 0.947 $DCPC_{avg}$ = 0.0325 Mass flow = 1.6612%	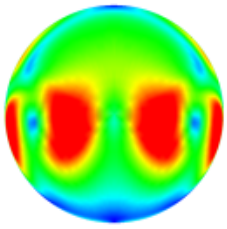	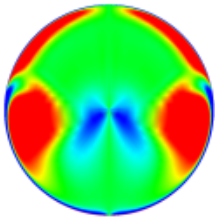
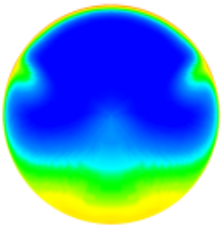	**Pyramid 4** DC60pt = 0.1017 DC60q = 0.494 SC60 = 0.0378 PR = 0.946 $DCPC_{avg}$ = 0.0440 Mass flow = 1.4774%	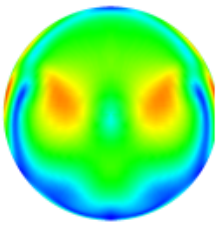	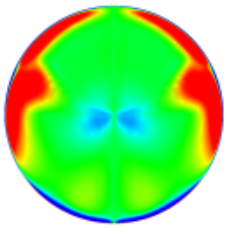

Total Pressure **Sec. Flow Vel.** **Vorticity**

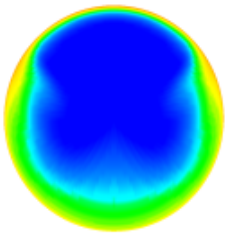

SCIR
DC60pt = 0.0651
DC60q = 0.239
SC60 = 0.0398
PR = 0.947
$DCPC_{avg}$ = 0.0199
Mass flow = 1.8559%

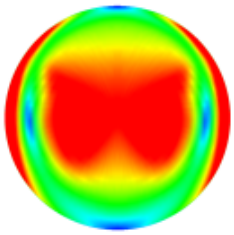

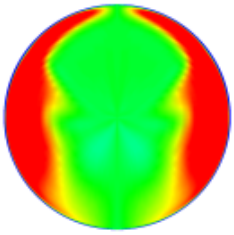

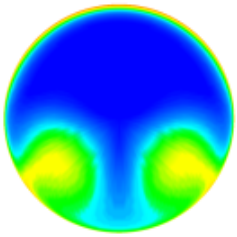

SA2
DC60pt = 0.0871
DC60q = 0.377
SC60 = 0.0101
PR = 0.941
$DCPC_{avg}$ = 0.0343
Mass flow = 2.0470%

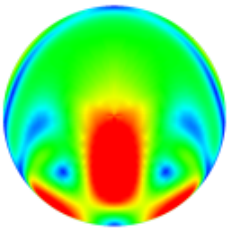

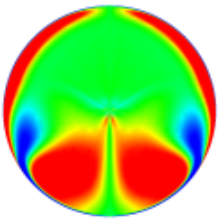

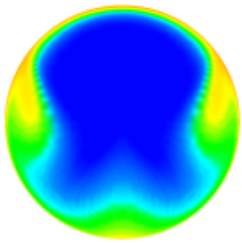

SP1
DC60pt = 0.0543
DC60q = 0.157
SC60 = 0.0833
PR = 0.945
$DCPC_{avg}$ = 0.0231
Mass flow = 1.9671%

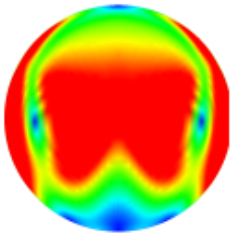

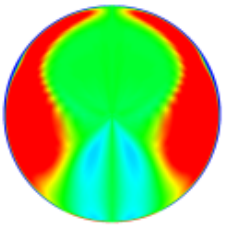

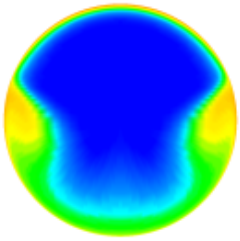

SRP
DC60pt = 0.0625
DC60q = 0.211
SC60 = 0.0696
PR = 0.945
$DCPC_{avg}$ = 0.0205
Mass flow = 1.7615%

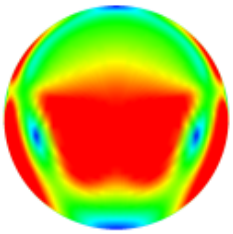

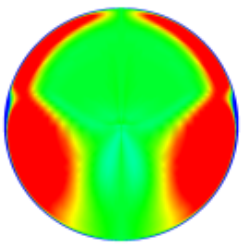

Total Pressure **Sec. Flow Vel.** **Vorticity**

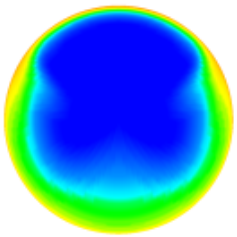

FSCIR
DC60pt = 0.0598
DC60q = 0.211
SC60 = 0.0355
PR = 0.947
$DCPC_{avg}$ = 0.0178
Mass flow = 1.8555%

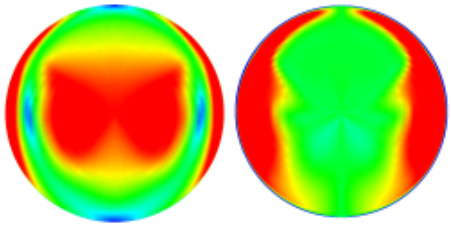

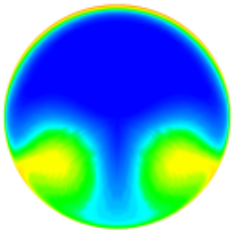

FSA2
DC60pt = 0.0896
DC60q = 0.383
SC60 = 0.0965
PR = 0.942
$DCPC_{avg}$ = 0.0358
Mass flow = 2.0418%

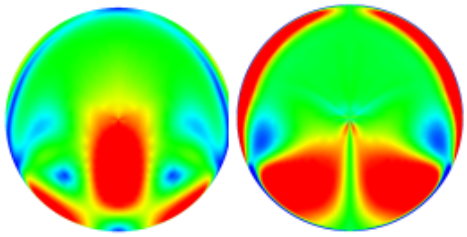

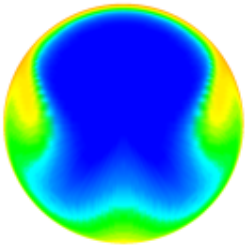

FSP1
DC60pt = 0.0586
DC60q = 0.180
SC60 = 0.0845
PR = 0.946
$DCPC_{avg}$ = 0.0240
Mass flow = 1.9643

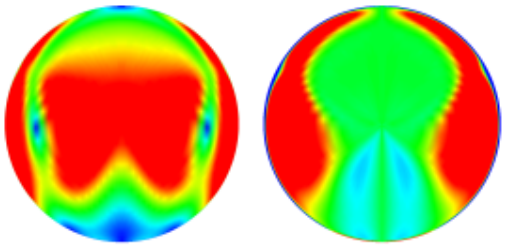

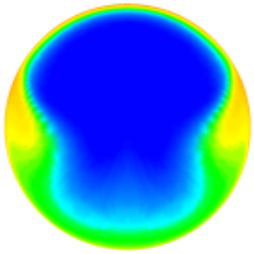

FSRP
DC60pt = 0.0595
DC60q = 0.192
SC60 = 0.0596
PR = 0.946
$DCPC_{avg}$ = 0.0264
Mass flow = %

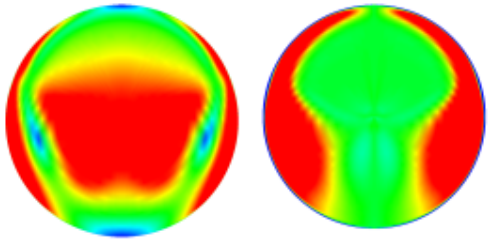

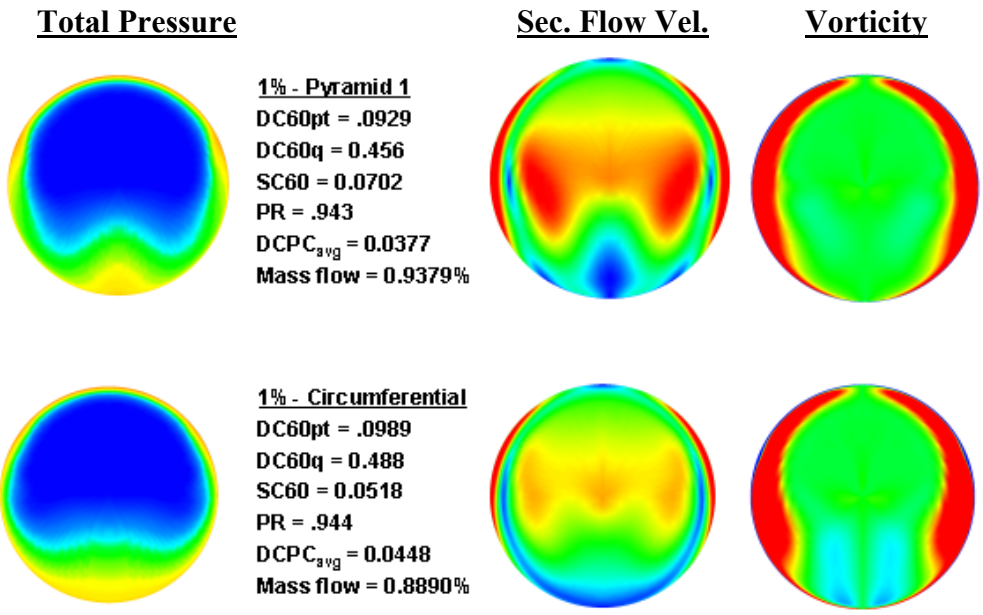

Flow Control Distortion Results

In this section, a brief description of all results obtained in the flow control analyses will be presented.

Figure G.0.5 and Figure G.0.6 show the obtained DC(60) distortion results for all flow control configurations tested. As compared to the baseline solution, all flow control cases reduced the AIP distortion to some extent. The application of 1% AIP mass suction alone did not appear to have any significant impact on the flow distortion. 'Conventional' flow control cases that utilized 1% of the AIP mass appeared to have varying degrees of effectiveness. The most successful of these cases were the circumferential and Pyramid 1 blowing schemes. Examinations of the 2% blowing only Pyramid blowing schemes suggest that the jet array angle has a significant impact on overall system effectiveness. The 2% axial blowing schemes did not substantially reduce distortion, although the axial 2 configuration showed improved performance over the axial 1 configuration when blowing fluid up the diffuser sidewall.

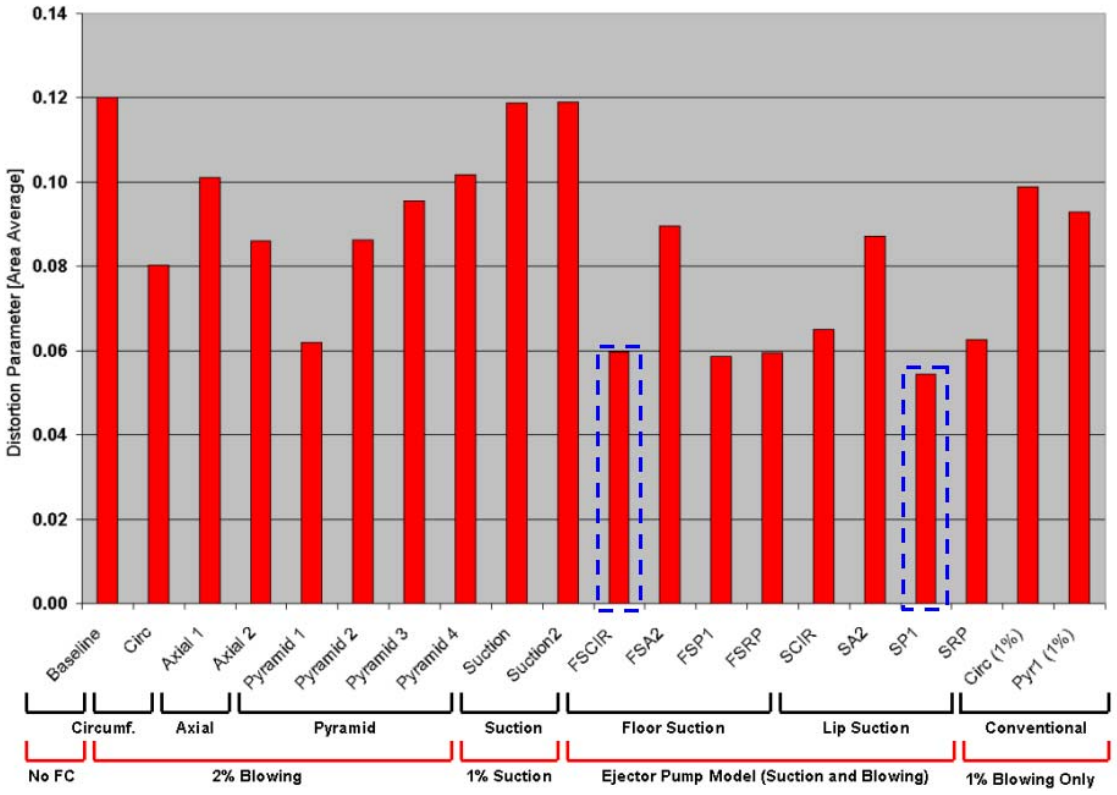

Figure G.0.5: DC(60)pt Distortion Parameter Results

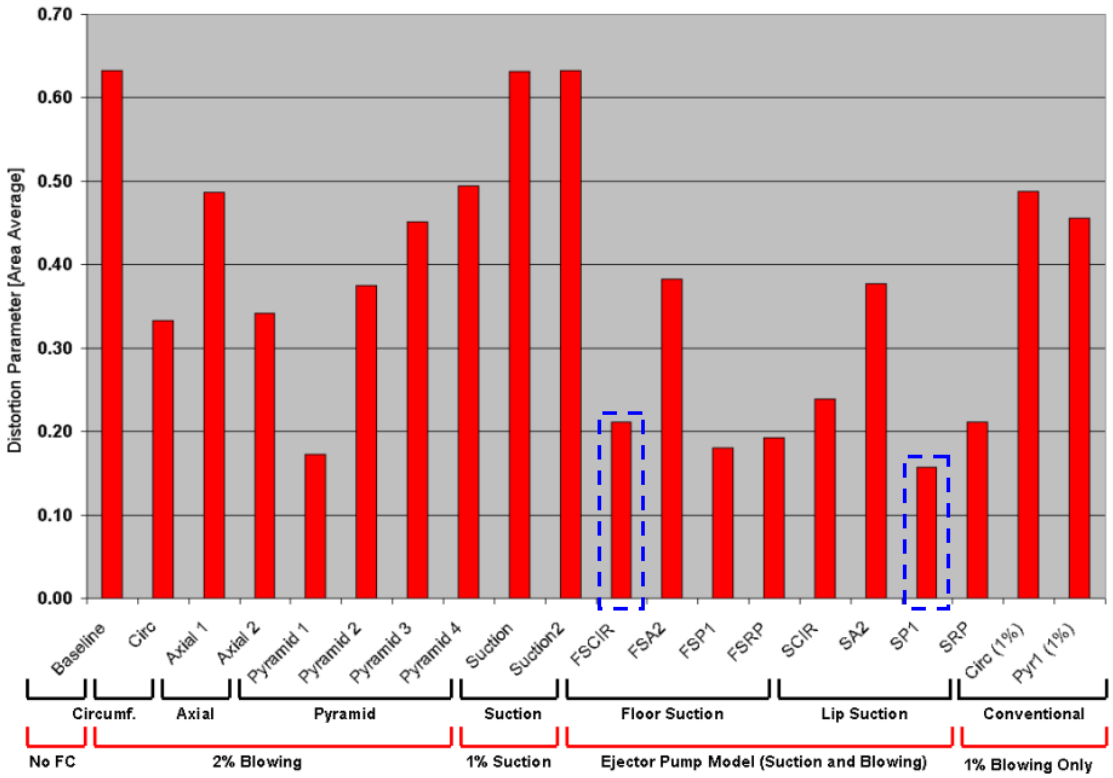

Figure G.0.6: DC(60)q Distortion Parameter Results

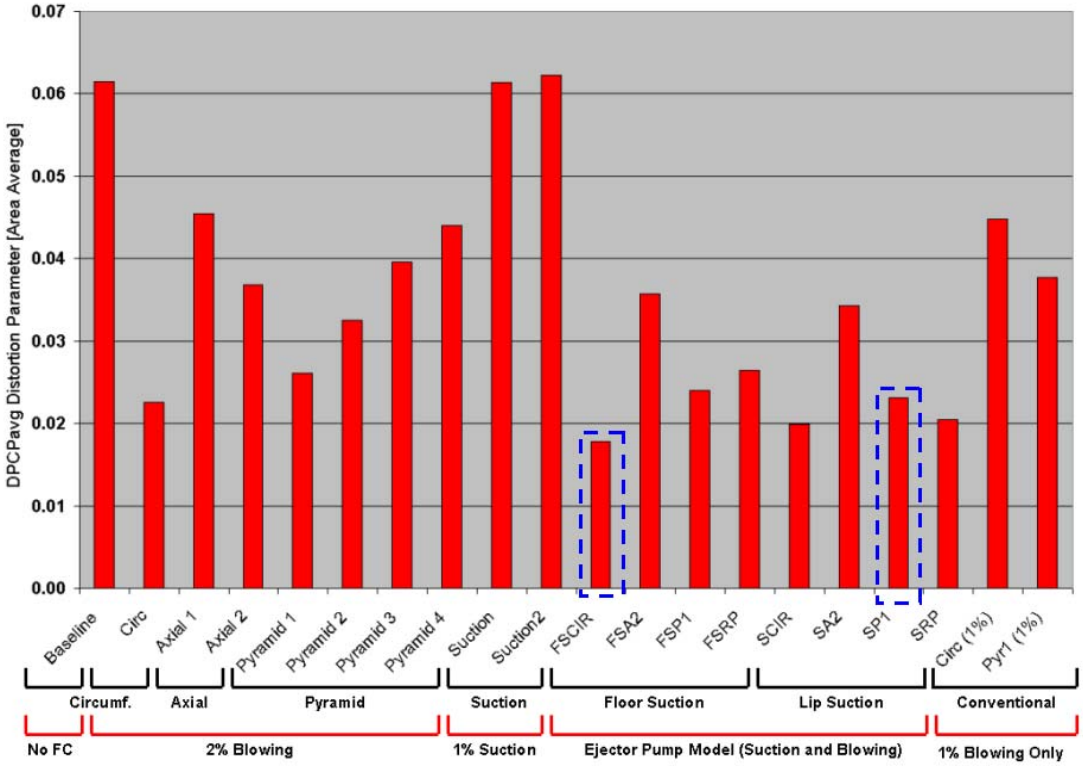

Figure G.0.7: DPCPavg Distortion Parameter Results

The SAE distortion descriptor DPCPavg, however, varies slightly in its perception of flow distortion at the AIP. (Figure G.0.7) In contrast to the DC(60) descriptors, the DPCPavg parameter reflects an average distortion for the whole AIP, as opposed to representing only the worst 60º sector of the flow. Although the distortion is significantly reduced by all flow control schemes, the circumferential and reverse Pyramid configurations are quantified as being more effective than the Pyramid1 configurations. The maximum reduction in distortion is achieved by the FSCIR scheme (71.1% reduction) which utilizes floor suction in combination with a circumferential blowing configuration. The reverse Pyramid configuration is also more effective than the Pyramid1 configuration. These results suggest that the lowest distortion is achieved by the configurations in which the individual jets do not coalesce into a single vortex. Both the circumferential and reverse Pyramid configurations have this feature, in contrast to the Pyramid 1 and axial schemes that continually reinforce a single vortex that sweeps up the sides of the diffuser.

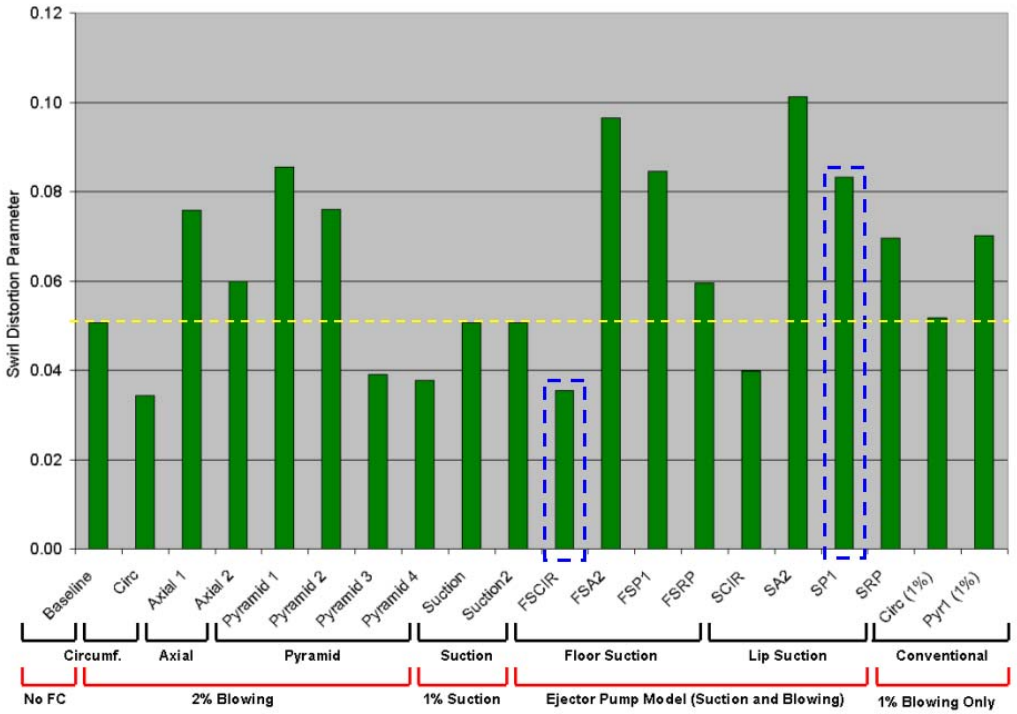

Figure G.0.8: SC(60) Swirl Distortion Parameter Results

Investigations of AIP flow swirl highlighted the impact of the flow control configurations on compressor flow quality. The DC(60) results suggested that in order to minimize flow distortion a significant blowing effort was required, and the 'conventional' 1% blowing cases did not have enough momentum to successfully counteract the diffuser secondary flows. However, the stronger ejector-driven jets needed to be carefully arranged so that they did not increase flow swirl at the AIP. With the exception of the reverse Pyramid configuration, the circumferential ejector case was the only ejector scheme to show a net reduction in swirl at the AIP. The larger angle Pyramid cases (3&4) show little increase in swirl, although these cases are closely related in configuration to the circumferential cases. In some cases it is also evident that the addition of flow suction had a negative impact on swirl at the AIP. When selecting a flow control configuration, it is important to realize that although some configurations can yield substantial improvements in total pressure distortion, the reduction is sometimes accomplished at the expense of an increase in swirl at the AIP. If of sufficient magnitude, swirl entering the compressor can lead to rotating stall and engine surge, thus trading one type of distortion for another.

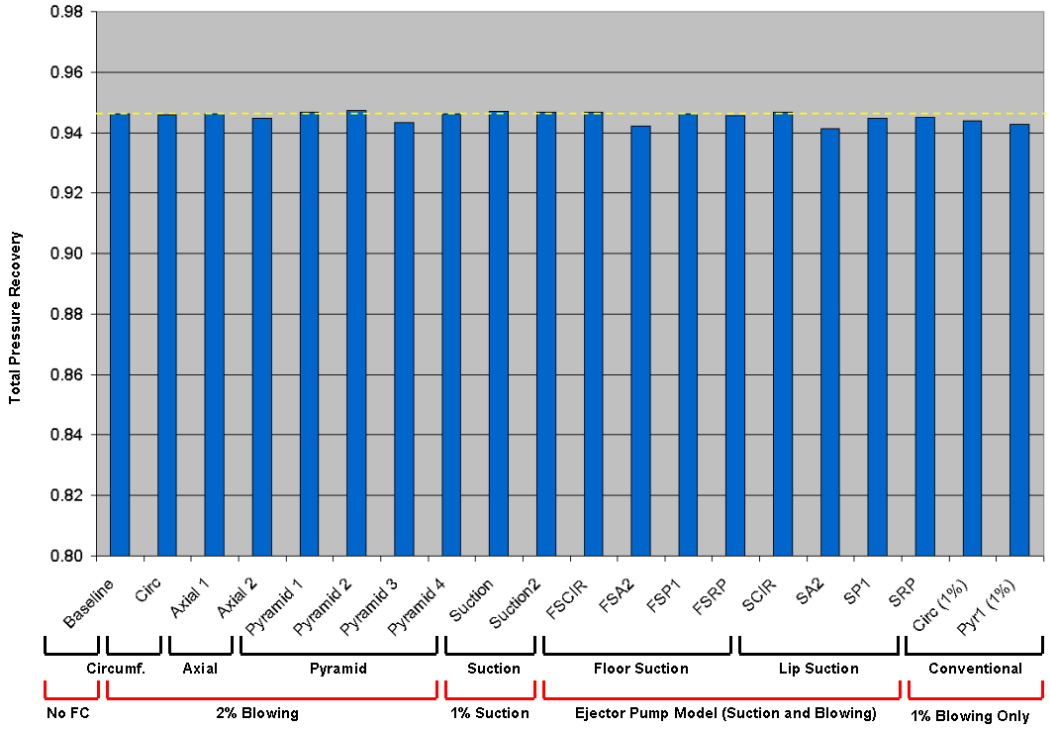

Figure G.0.9: Total Pressure Recovery Results

All configurations tested did not appear to have a strong impact on duct pressure recovery with no clear increase or decrease from the baseline value.

Appendix H: Calculations and Uncertainty

During the course of the experimental work, several flow quantities had to be calculated from measured temperature and pressure data. This section outlines those calculations and provides error estimates on all obtained data and the resulting calculations.

Experimental Calculations

The current experimental setup measures 111 time-averaged pressures and 6 time-averaged temperatures for each flow control condition at the desired simulated flight condition. An overview of these measurements is shown in the schematic of Figure H.0.1.

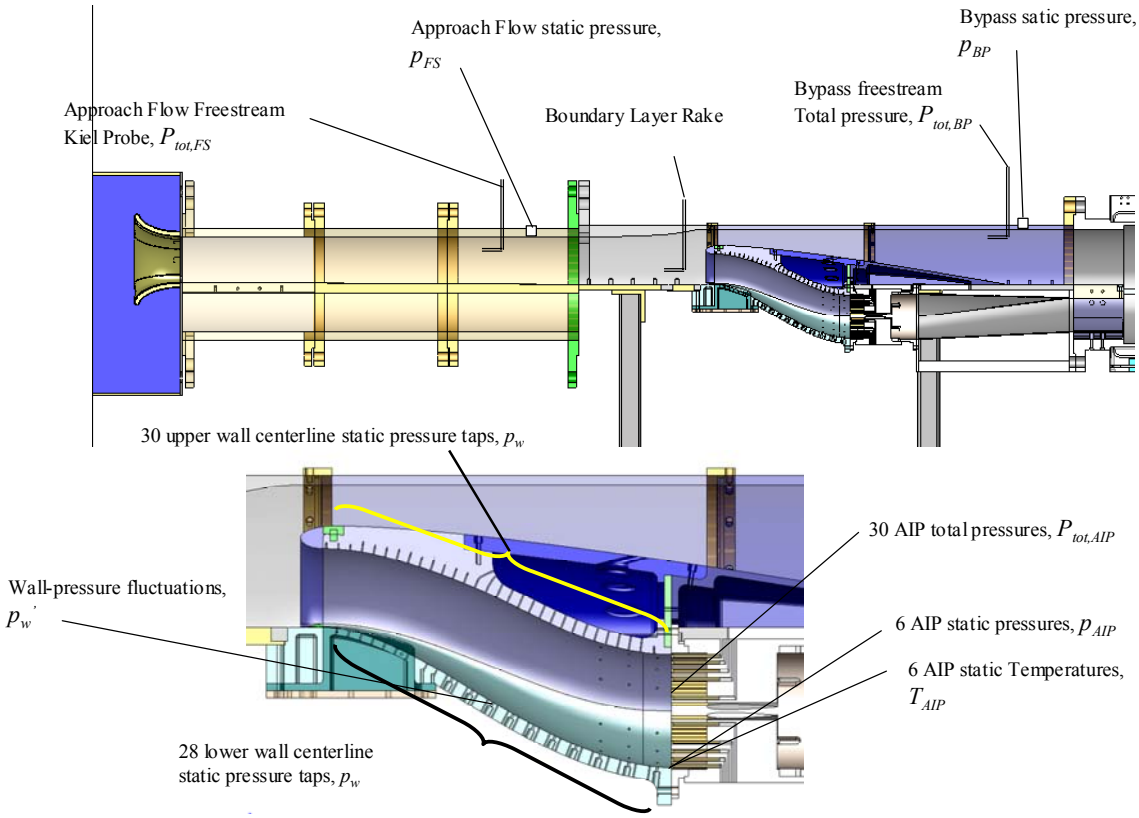

Figure H.0.1: Overview of measurements

A summary of the transducers and data acquisition is shown in Table H.2.

Table H.2: Summary of Transducers and Data Acquisition

Parameter	Quantity	Transducer	DAQ System
P_{FS}	2	ZOC, 0-15 psid	
p_{FS}	1	ZOC, 0-5 psid	
P_{BL}	7	ZOC, 0-5 psid	National Instruments,
p_w	60	ZOC, 0-5 psid and DSA	64-ch. Card
P_{AIP}	30	PSI	+ GPIB card for PSI
p_{AIP}	6	ZOC, 0-5 psid	system
T_{AIP}	6	K-type Thermocouple	+ Ethernet connection
P_{motive}	1	Transmitter	for DSA system
$p_{suction}$	1	ZOC, 0-5 psid	
$P_{massflow}$	4	ZOC, 0-5 psid	

In order to perform these pressure measurements, Techsburg has compiled three different pressure transducer systems: a 32-channel ScaniValve DSA pressure module system, a 32-channel PSI pressure measurement system, and a modular 48-channel ScaniValve ZOC pressure transducer system. The DSA and PSI pressure transducer systems both send digitized signals to a host computer via an Ethernet cable and a GPIB connection, respectively. The ZOC system sends analog signals to a National Instruments 64-channel A/D card in the host computer. A National Instruments Lab View program has been composed to simultaneously acquire the electrical signals from all three transducer systems and compute the necessary performance metrics of the experiment, which will be subsequently explained in this section of the report.

As seen in Figure H.0.1, the freeestream inlet approach flow will be characterized by the freestream total pressure P_{FS} , the freestream static pressure p_{FS}, and the freestream total temperature $T_{tot,FS}$, which will assumed to be equal to the room ambient temperature T_{amb}. With the aforementioned freestream approach flow parameters, the freestream Mach number M_{FS} will be calculated:

$$M_{FS} = \sqrt{\frac{2}{\gamma - 1}\left(\left(\frac{P_{FS}}{p_{FS}}\right)^{\gamma-1/\gamma} - 1\right)}$$

The static temperature of the freestream approach flow will be determined according to the isentropic relation:

$$T_{FS} = \frac{T_{amb}}{1 + \frac{\gamma - 1}{2} M_{FS}^2}$$

The freestream velocity will then be determined according to:

$$V_{FS} = M_{FS}\sqrt{\gamma RT_{FS}}$$

These equations will be used in conjunction with the measured inlet mass flow rate to compute the corrected mass flow ratio $c_{\dot{m}}$, which is a measure of the inlet capture.

Moving further downstream in the B.L. Development Region, the next parameter to be determined is the boundary layer thickness just upstream of the inlet entrance. A boundary layer rake will be used to measure the boundary layer total pressures P_{BL}, which in combination with local static pressure will be used to determine the velocity profile. This profile will then be used to determine the boundary layer thickness δ.

By far, most of the measurements to be performed in this experiment are concentrated inside the offset BLI inlet. There will be 60 duct centerline locations (30 along the top and 30 along the bottom) where time-averaged, wall-pressures p_w will be measured.

At the exit plane (AIP) of the offset BLI inlet a 30 total pressure probe rake is stationed in order to measure total pressure distortion. Each total pressure probe is positioned at the centroid of equal area sectors, which allows for area-weighted averages of the AIP total pressures P_{AIP} to be computed by the arithmetic mean of all 30 measurements. Also at the AIP, there will be 6 time-averaged wall-pressure p_{AIP} and 6 wall temperature T_{AIP} measurements made at locations indicated in Figure H.0.2.

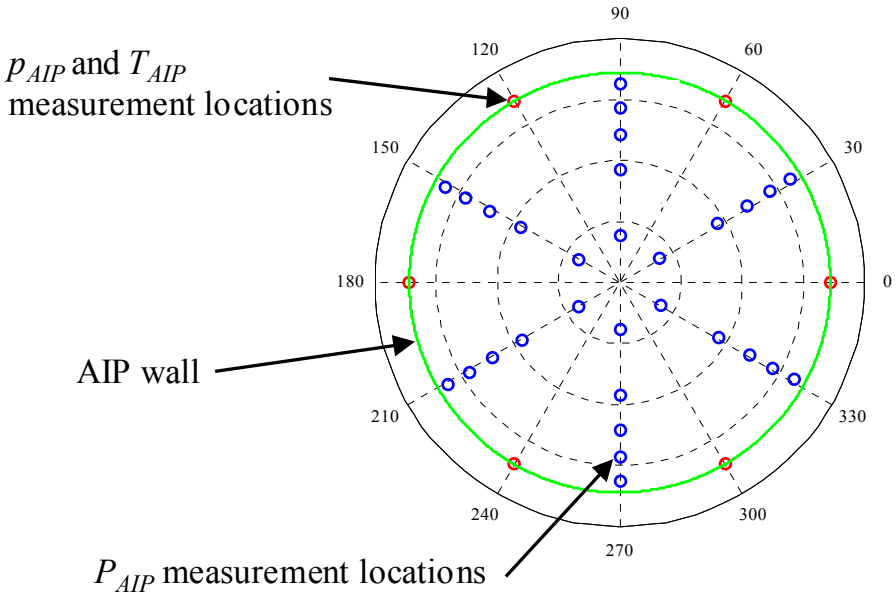

Figure H.0.2: AIP measurement locations

The inlet mass flow rate is then computed with the AIP measurements according to:

$$\dot{m}_{inlet} = \langle p_{AIP} \rangle \sqrt{\left(\frac{2\gamma}{R(\gamma - 1)\langle T_{AIP} \rangle} \right) \left[\left(\frac{\langle P_{AIP} \rangle}{\langle p_{AIP} \rangle} \right)^{\gamma - 1/\gamma} - 1 \right]}$$

where $\langle p_{AIP} \rangle \equiv$ arithmetic mean of 6 wall pressure measurements,

$\langle T_{AIP} \rangle \equiv$ arithmetic mean of 6 wall temperature measurements,

and $\langle P_{AIP} \rangle \equiv$ arithmetic mean of 30 AIP total pressure measurements.

Once the inlet mass flow rate is determined, the non-dimensional mass flow ratio $c_{\dot{m}}$ can be computed according to:

$$c_{\dot{m}} = \frac{\dot{m}_{inlet} R T_{FS}}{p_{FS} V_{FS} A_{AIP}}$$

This calculation serves as an indication of the amount of freestream flow captured by the inlet; NASA simulations use the design condition of $c_{\dot{m}} \approx 0.72$.

The next set of calculations are concerned with computing the total pressure distortion metrics DC(60). The DC(60) distortion metrics are defined as:

$$\text{DC60q} = \frac{\langle P_{AIP} \rangle - \langle P_{\theta} \rangle}{q_{AIP}}$$

$$\text{DC60pt} = \frac{\langle P_{MAX} \rangle - \langle P_{\theta} \rangle}{\langle P_{AIP} \rangle}$$

Where $\langle P_{\theta} \rangle$ is defined as the mean total pressure in the 'worst' sector (of angle θ) of the AIP, and $\langle P_{MAX} \rangle$ is the sector of 'best' total pressure. The dynamic pressure q_{AIP} will be estimated using the same nomenclature as above according to:

$$q_{AIP} = \frac{\gamma \langle p_{AIP} \rangle}{(\gamma - 1)} \left[\left(\frac{\langle P_{AIP} \rangle}{\langle p_{AIP} \rangle} \right)^{\gamma - 1/\gamma} - 1 \right].$$

Uncertainty Calculations

Calculations of uncertainty are based primarily on the uncertainty of individual transducers and the propagation of errors calculated according to the Kline-McClintock method.[25] This method utilizes a linear approximation between the dependent and measured variables. When the uncertainty in a measurement is dependent on more than one variable, the total uncertainty is correlated to the partial derivative of each dependent variable. Thus, if the function

$$F = f(a,b,c,d)$$

Then the uncertainty in F (u_F) is determined according to:

$$u_F = \pm \sqrt{\left(\left(\frac{\partial F}{\partial a} \right) \cdot \delta\, a \right)^2 + \left(\left(\frac{\partial F}{\partial b} \right) \cdot \delta\, b \right)^2 + \left(\left(\frac{\partial F}{\partial c} \right) \cdot \delta\, c \right)^2 + \left(\left(\frac{\partial F}{\partial d} \right) \cdot \delta\, d \right)^2}$$

Where $\left(\frac{\partial F}{\partial x} \right)$ represents the linear dependence of each variable and $\delta(x)$ represents the transducer errors represented in Table H.3.

Table H.3: Transducer Uncertainties (δ(x))

Transducer	Range	Uncertainty
ZOC	0-15 psid	± 0.00975 psi
ZOC	0-5 psid	± 0.00325 psi
DSA	0-30 psid	± 0.015 psi
DSA	0-5 psid	± 0.0025 psi
PSI	0-15 psid	± 0.0075 psi

These values can then be combined with the equations used to determine the uncertainty in each calculated flow parameter. Results obtained from this analysis yielded the uncertainty values listed in Table H.4.

Table H.4: System Metric Uncertainty Based on Transducer Error

Parameter	Uncertainty
M_{FS}	± 0.00355 psi
T_{FS}	± 1.7702 K
V_{FS}	± 1.4732 m/s
q_{AIP}	± 0.00167 psi
DC(60)pt	± 0.0010
DC(60)q	± 0.0051

The obtained transducer uncertainty results may then be plotted on the obtained data as error bars. The uncertainty results show a relatively small variation in the critical distortion parameters, and are likely less important than some of the basic assumptions inherent in the distortion equations. Of the most particular note is the assumption that the six static pressure measurements located around the AIP are sufficient to determine the face average pressure value. This assumption can be investigated through a brief examination of the CFD results.

By comparing the integrated CFD solutions with simulated wind tunnel calculation methods additional uncertainty values could be calculated. These uncertainties are based on the maximum deviation of tunnel calculation methods from interpolated CFD results. Values obtained from this analysis are listed in Table H.5.

Table H.5: Distortion Uncertainty Based on Assumption Error

Parameter	Uncertainty
DC(60)pt	± 0.0012
DC(60)q	± 0.0385

Based on experimental results, the uncertainty due to flow approximations can range from 5.6%-27.2% for the DC(60)q parameter, and 0.9%-2.2% for obtained DC(60)pt values. Experimentally calculated DC(60)q values are considerably affected by the flow assumptions. This increase in distortion uncertainty is largely the result of uncertainty in the calculation in AIP average dynamic pressure.

Appendix I: Wind Tunnel Adaptation of CFD Grid

To predict the basic wind tunnel performance, the flow control grid was modified to model the boundaries of the experimental setup. Far-field boundaries were replaced with the wind tunnel walls as represented in Figure I.0.1.

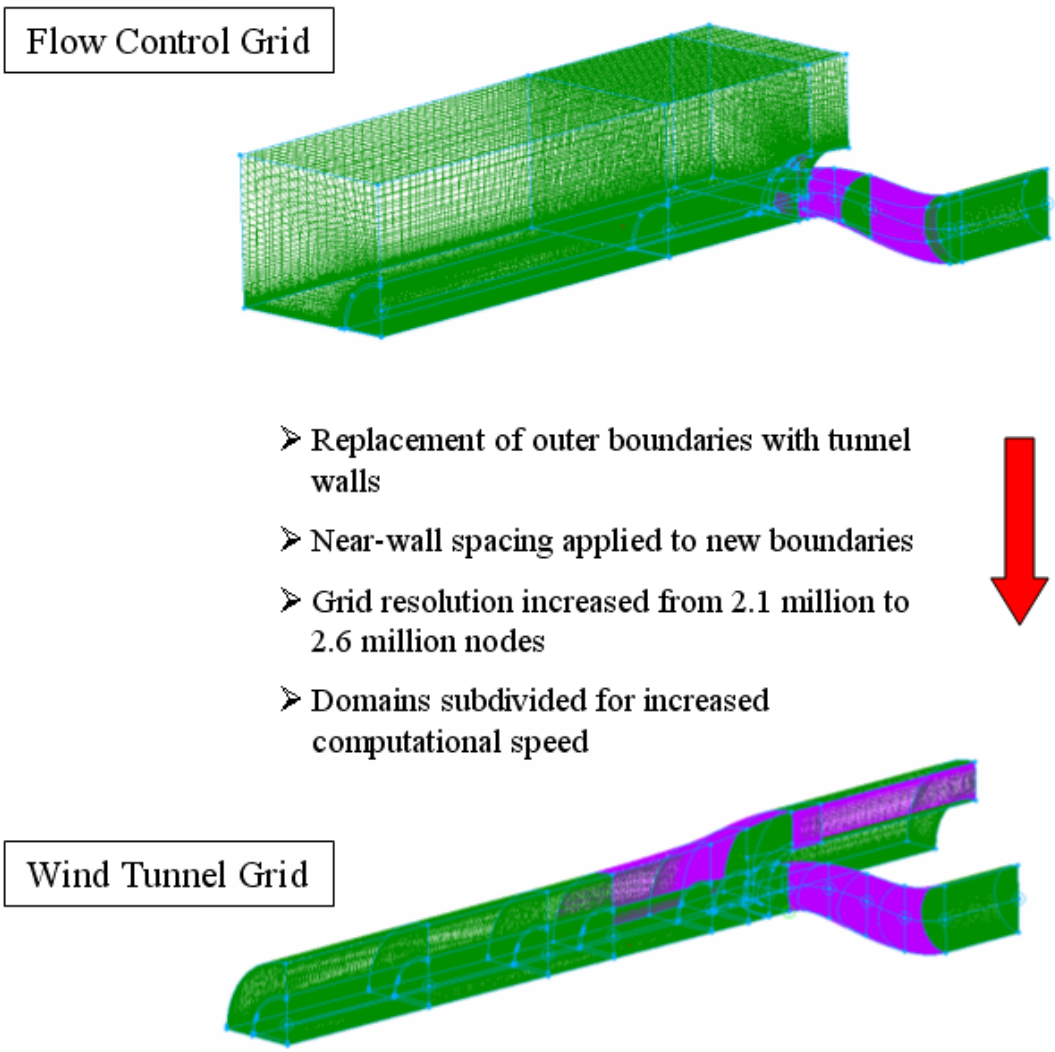

Figure I.0.1: Wind Tunnel Grid Modification

Due to this adaptation, the number of points within the grid increased in order to capture the boundary growth along the inside of the added tunnel walls. These calculations were critical as it was necessary to determine if the flow from the interior walls would be ingested by the inlet. In order to reduce this possibility, the tunnel walls expanded near the inlet. The wall curvature was based upon a streamline obtained from the CFD baseline solution.

The mesh was also adapted to remove the polar point from the mesh, by incorporating a center block and wrapping the internal duct surface mesh around it. (Refer to Figure I.0.2) This allowed for a quicker convergence due to the increased local time-step, but prohibited the use of the *distortion_param* program.

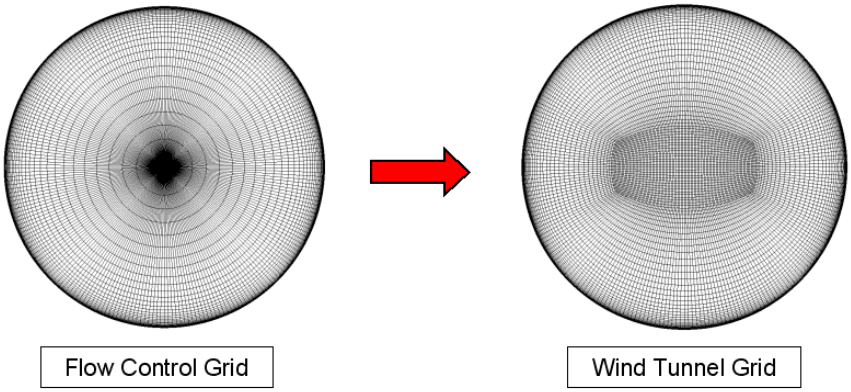

Figure I.0.2: AIP Grid Modification

Appendix J: Wind Tunnel Flow Quality

Axial Pressure Gradient

Investigations into the quality of flow within the wind tunnel were conducted during experiments. Data was collected to characterize the axial and transverse pressure gradients due to their ability to affect as well as diagnose boundary layer quality. In addition, the ingested boundary layer velocity profile was compared to computational predictions. Figure J.0.1 shows the static pressure gradient along the length of the boundary layer growth region. The pressure gradient along the growth region is relatively constant, although it is evident that the area expansion along the length was not sufficient to entirely prevent flow acceleration due to boundary layer displacement thickness growth. Significant change begins to occur at the onset of the tunnel area expansion. This expansion causes a drop in static pressure as the flow that is not ingested into the inlet is forced to accelerate into the flow bypass. A sharp pressure increase is evident when the ram effect of the inlet begins to impinge on the flow. This positive pressure gradient is characteristic of isentropic compression occurring as a result of engine inlet capture, and results in a local thickening of the boundary layer. (Shown in a previous section.)

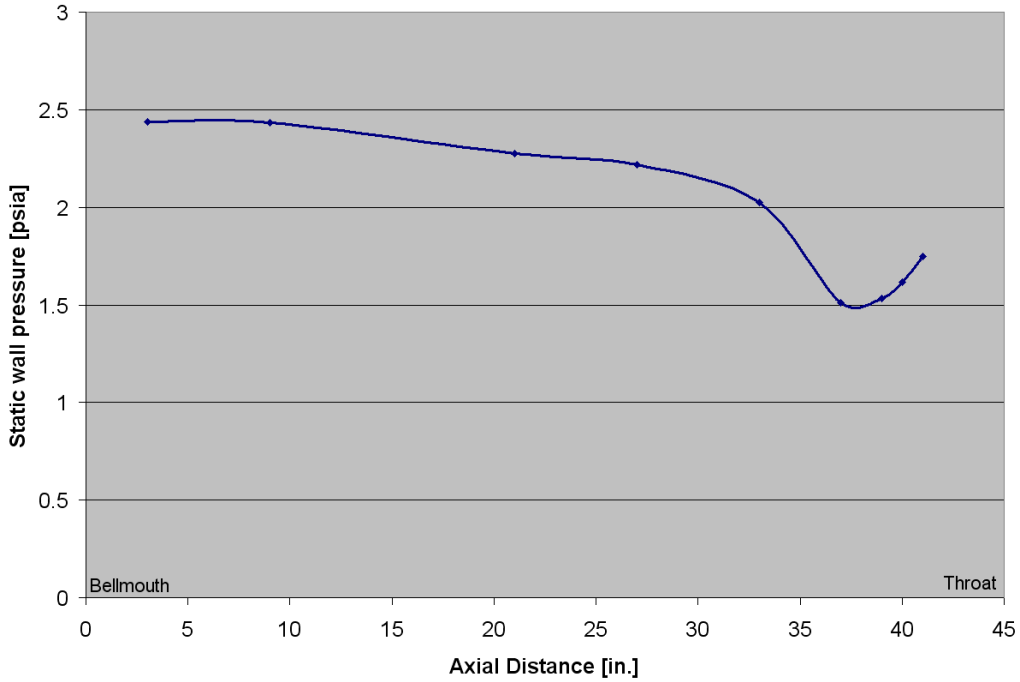

Figure J.0.1: Wind Tunnel Axial Pressure Gradient

Spanwise Pressure Gradient

Figure J.0.2 shows the transverse static pressure gradient ~2" upstream of the inlet. This gradient was measured in order to diagnose the quality of flow being ingested into the inlet. The relatively constant profile suggests that there are no large-scale flow perturbations being ingested. When coupled with the measured boundary layer velocity profile it was determined that the general boundary layer flow quality was reasonable and not likely to cause any large-scale deviations from predicted results. The slight drop in pressure at the outermost points may be flow that is being accelerated as it is diverted around the inlet lip; this outer flow was not likely ingested.

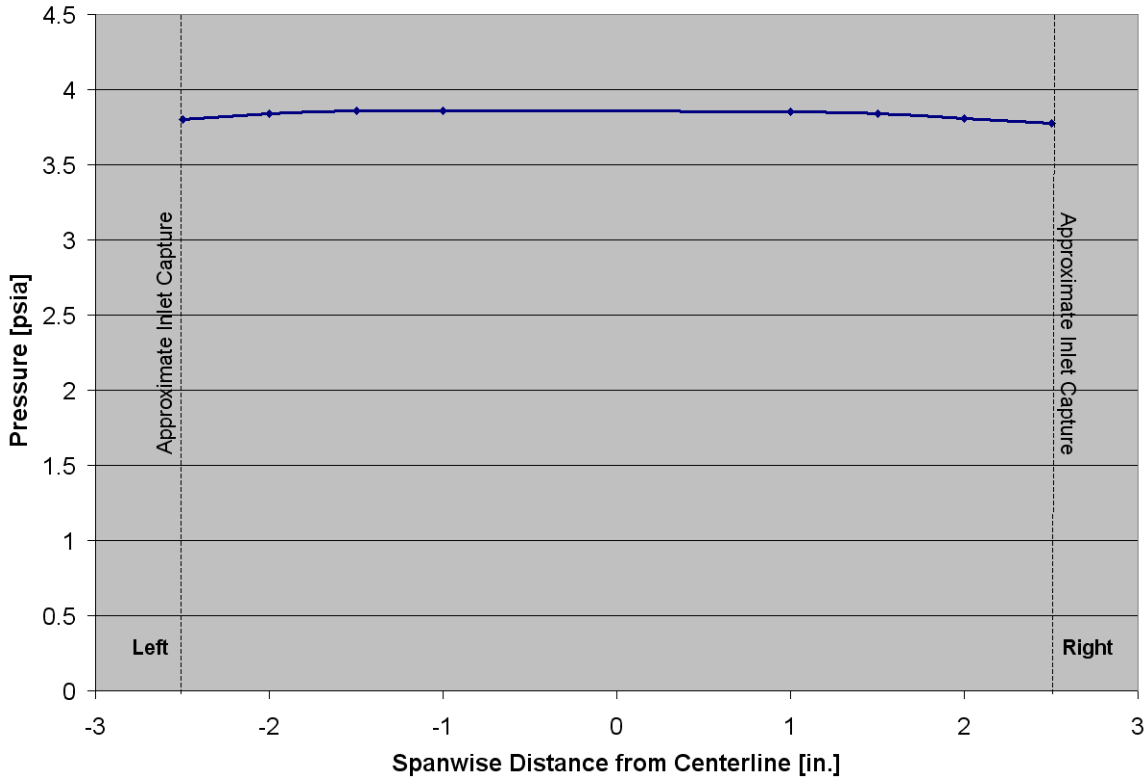

Figure J.0.2: Wind Tunnel Transverse Pressure Gradient

Diffuser Static Pressure Profile

Wind tunnel static pressure measurements of the upper and lower diffuser surfaces are shown in Figure J.0.3. The pressure profiles shown for the upper and lower surfaces compare well between the CFD and experimental results. The vertical offset is consistent with the variation in freestream Mach number; experimental data was not collected at as high a Mach number as analyzed in CFD. Upper surface contrours show the initial pressure rise associated with the first diffuser turn. This pressure then decreases throughout the length of the duct and begins to climb again briefly near the AIP at the onset of the second turn. Lower contours shown the effect of the area diffusion as the pressure gradually rises along the length of the duct. The pressure offset between the upper and lower walls at the AIP indicate a difference in the flow Mach number resulting from the presence of distortion on the lower diffuser surface.

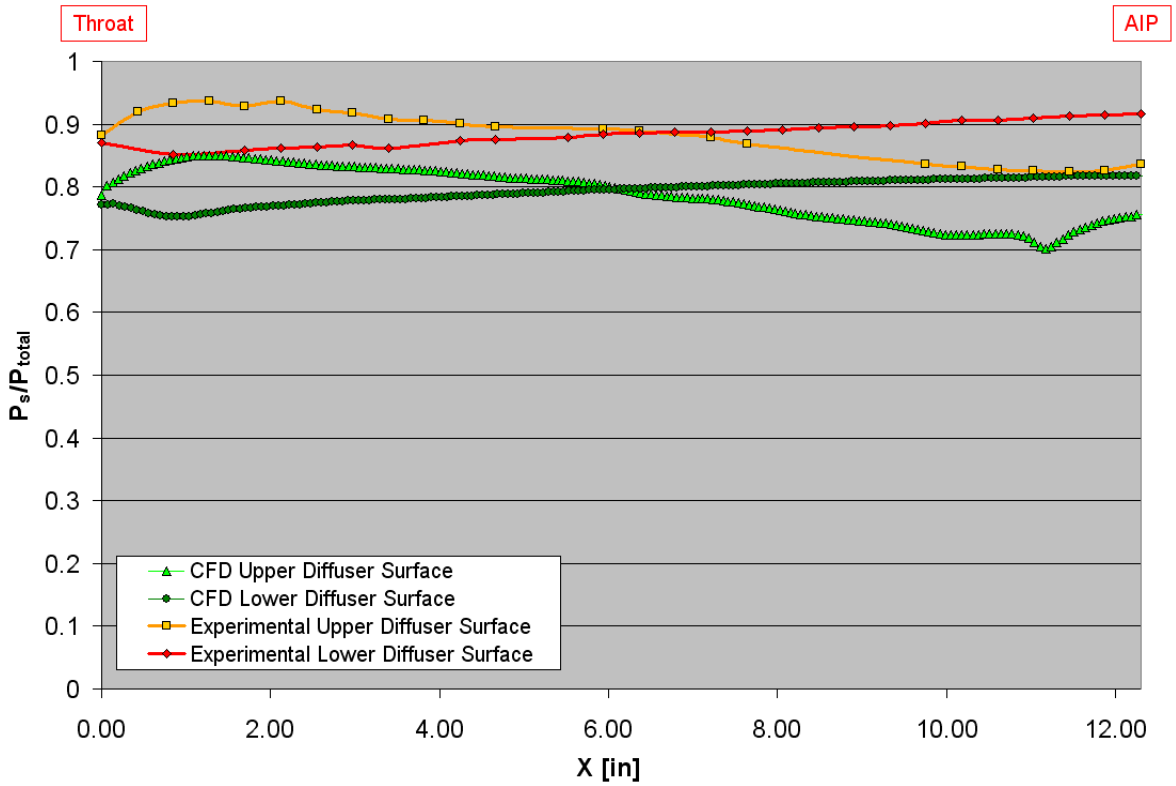

Figure J.0.3: Baseline Diffuser Centerline Static Pressure

Appendix K: ADPAC

ADPAC (Advanced Ducted Propfan Analysis Code) was created by the Allison Engine Company under funding by NASA.[19] It utilizes a finite-volume, multi-grid, Runge-Kutta time-marching solution algorithm to solve a time dependent form of the 3D Reynolds-Averaged Navier-Stokes (RANS) equations. The code provides a multiple block mesh discretization to allow for flexibility when meshing complex geometries. The Reynolds stresses (representing the time-averaged turbulence values) are modeled via the Boussinesq approximation. This simplifies the Reynolds shear-stress terms by eliminating them in favor of a modified effective viscosity:

$$\mu_{effective} = \mu_{laminar} + \mu_t$$

Where μ_t represents the eddy viscosity – a term used to relate the turbulent stresses to the flow mean strain rate.

The Spalart-Allmaras Turbulence Model

The Spalart-Allmaras (S-A) turbulence model is the highest-fidelity working turbulence model available for use in ADPAC. According to the Boussinesq approximation, the turbulent (eddy) viscosity is modeled, in this case by one equation that evaluates the kinematic viscosity (ν) in the transport equation:

$$\frac{D\tilde{\upsilon}}{Dt} = \Pr oduction + Diffusion - Destruction + Trip$$

Appendix L: Jet Configurations

The complete coordinate details of all jet configurations examined in this study are shown in this section. The x and y coordinates shown for each configuration are measured from the nacelle highlight and duct centerline respectively, as indicated in Figure L.0.1.

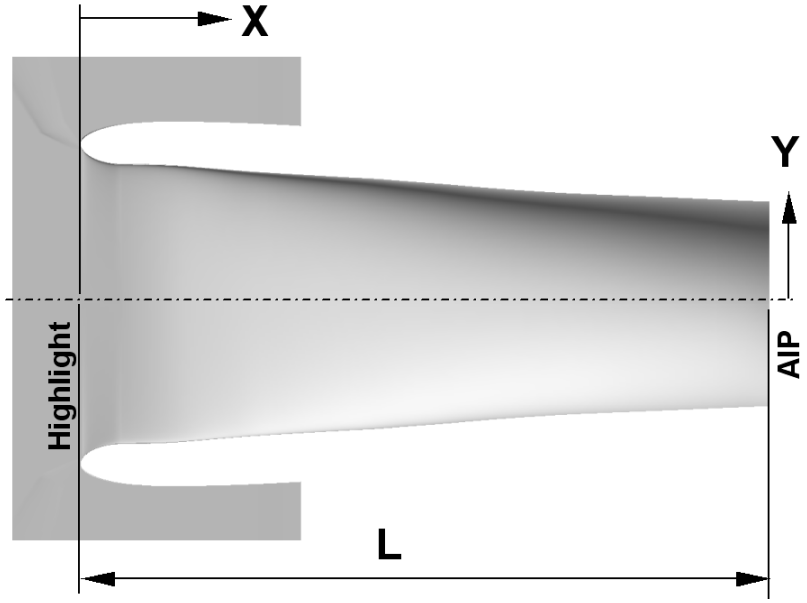

Figure L.0.1: Duct Coordinates

Axial 1

Jet	X/L	Y/L
1	0.125	0.136
2	0.156	0.129
3	0.185	0.118
4	0.213	0.111
5	0.238	0.108
6	0.267	0.107
7	0.298	0.110

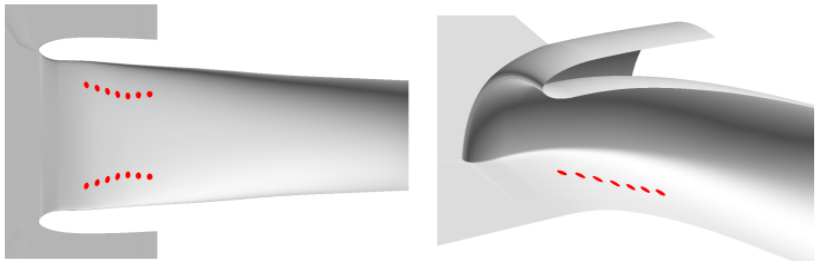

Figure L.0.2: Axial 1 Jet Coordinates

Axial 2

Jet	X/L	Y/L
1	0.126	0.017
2	0.156	0.017
3	0.184	0.017
4	0.212	0.017
5	0.241	0.017
6	0.270	0.017
7	0.302	0.017

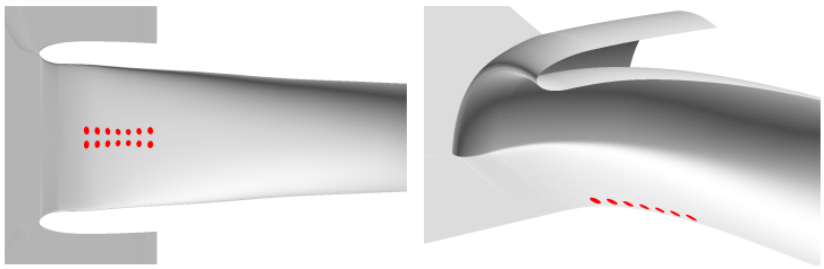

Figure L.0.3: Axial 2 Jet Coordinates

Circumferential

Jet	X/L	Y/L
1	0.126	0.021
2	0.126	0.062
3	0.126	0.101
4	0.126	0.136
5	0.126	0.174
6	0.126	0.201
7	0.126	0.195

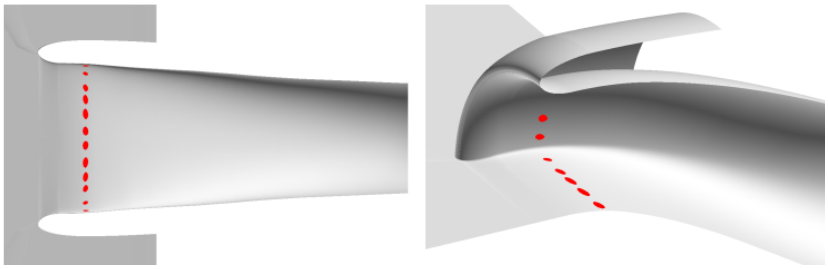

Figure L.0.4: Circumferential Jet Coordinates

Pyramid 1

Jet	X/L	Y/L
1	0.126	0.017
2	0.156	0.042
3	0.185	0.067
4	0.210	0.086
5	0.238	0.104
6	0.266	0.127
7	0.296	0.147

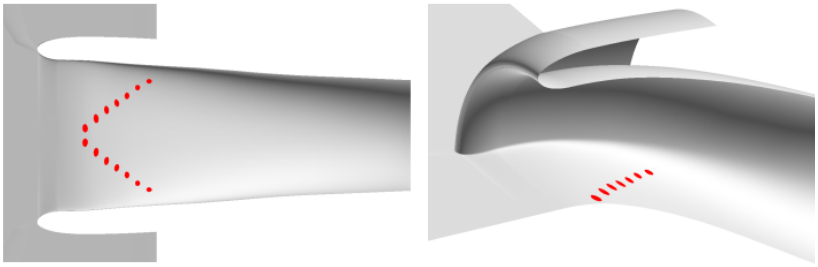

Figure L.0.5: Pyramid 1 Jet Coordinates

Pyramid 2

Jet	X/L	Y/L
1	0.126	0.021
2	0.157	0.059
3	0.181	0.094
4	0.209	0.118
5	0.239	0.145
6	0.267	0.166
7	0.299	0.178

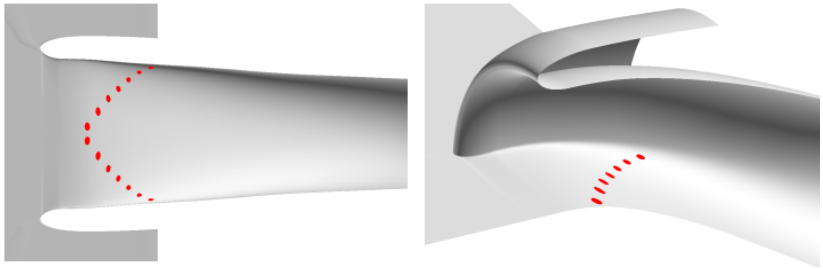

Figure L.0.6: Pyramid 2 Jet Coordinates

Pyramid 3

Jet	X/L	Y/L
1	0.126	0.019
2	0.155	0.089
3	0.183	0.139
4	0.210	0.171
5	0.238	0.191
6	0.268	0.190
7	0.300	0.181

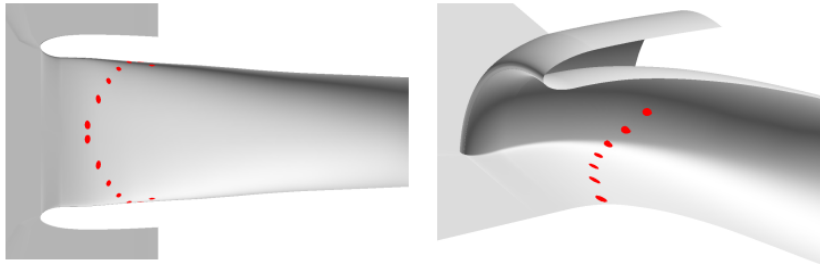

Figure L.0.7: Pyramid 3 Jet Coordinates

Pyramid 4

Jet	X/L	Y/L
1	0.126	0.019
2	0.143	0.092
3	0.159	0.145
4	0.175	0.177
5	0.191	0.195
6	0.207	0.194
7	0.224	0.185

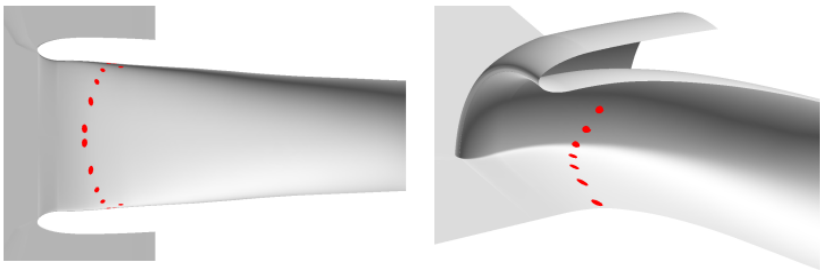

Figure L.0.8: Pyramid 4 Jet Coordinates

Reverse Pyramid

Jet	X/L	Y/L
1	0.125	0.168
2	0.155	0.147
3	0.183	0.118
4	0.211	0.086
5	0.239	0.059
6	0.268	0.039
7	0.300	0.018

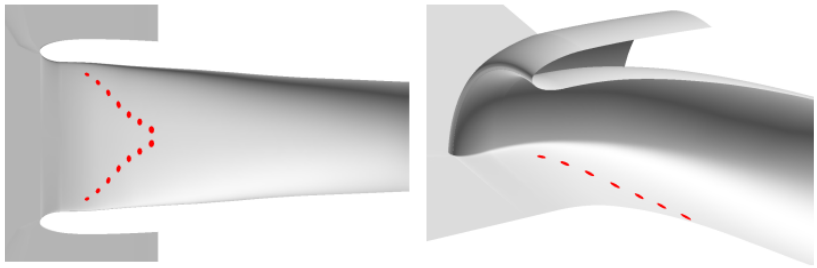

Figure L.0.9: Reverse Pyramid Jet Coordinates

Appendix M: Effects of DC(60)

Due to the physical constraints of wind tunnel modeling, it was not possible to create a rake of higher fidelity. Time constraints during testing also prevented rotating the rake to increase fidelity. Thus, the pressure contours at the AIP must be carefully interpreted. Computational and rake measurements are shown in Figure M.0.1 to show how distortion is captured by the rake. The case shown represents Reverse Pyramid results obtained by experiment. The far left contour is the analysis from CFD, and uses almost 10,000 points over the AIP area. The center image utilizes data from CFD and simulates what a standard DC(60) distortion rake (30 finite measurement locations) would interpret from this data. The far right image was measured experimentally. DC(60) distortion numbers for all cases are presented. Most apparent in the qualitative comparison of the CFD contours is that the distortion rake does not capture the lowest total pressure region due to the rake's finite nature. As such, this highlights the fact that taking finite measurements can provide both accurate and poor results based upon where the primary flow distortion lies. For this reason, a variety of flow distortion descriptors should be used, with as much resolution of measurements as possible. The experimental

contour image does highlight the fact that the experimental rake does capture the same flow physics as captured by the CFD rake. DC(60)pt Distortion descriptors show good comparison, and also suggest that reasonably accurate results were obtained with the rake configuration tested.

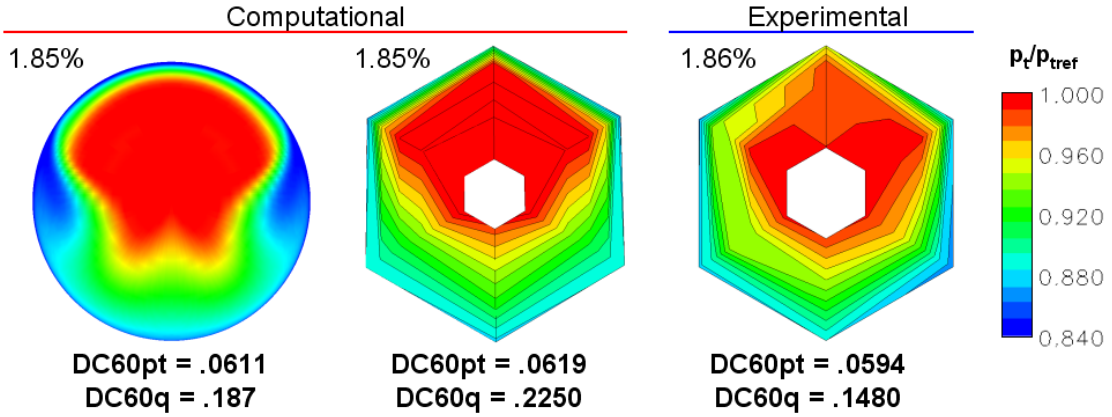

Figure M.0.1: Effect of Rake on Distortion

However, variation in the DC(60)q parameter highlights the difficulty in accurately determining values based upon the AIP dynamic pressure (q_{AIP}) during experimental investigations. This is primarily due to the need to estimate both AIP average static and total pressures based on finite measurements. The average total pressure is computed using the 30 rake measurements from within the flow field at the AIP. However, the average static pressure is calculated from wall measurements at select locations around the AIP. This can lead to a substantial error in estimation of the face dynamic pressure, and thus contributes to error in the DC(60)q metric. By examining the CFD interpolated results and comparing them to the CFD finite measurements used in this experiment by way of a "simulated" rake, this estimation can result in a DC(60)q uncertainty of ± 0.038. (As determined in Appendix H.) The reason for this variation is apparent when examining the AIP static pressure contours of Figure M.0.2, and the significant variation in static pressure across the engine face.

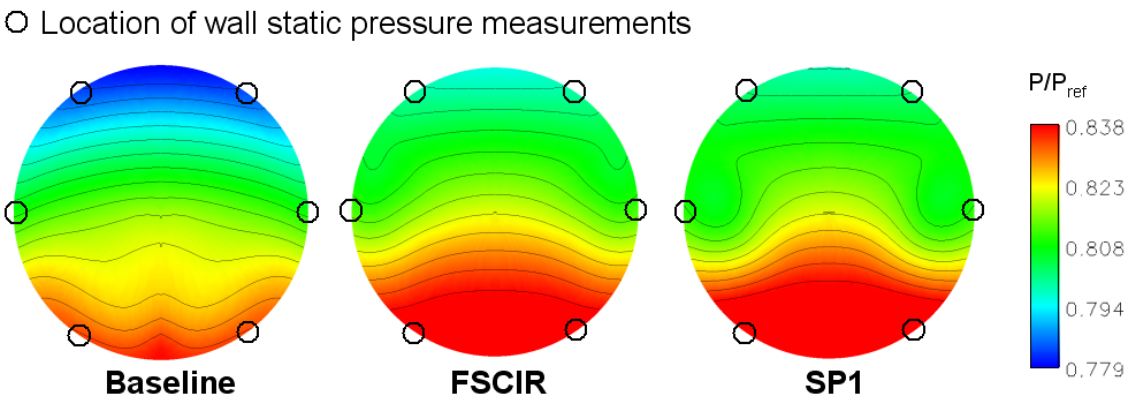

Figure M.0.2: AIP Static Pressure Contours

Because of these inaccuracies, any calculation based upon the face dynamic pressure will inherently have high error. For this reason, it seems much more practical to use the DC(60)pt parameter to describe results. Results obtained in this study also highlight an increased accuracy when comparing to predicted DC(60)pt values, in addition to being a more robust parameter capable of collapsing results for different flow rates and duct sizes.[4] Ultimately, engine companies have distortion descriptors that are more complicated, more costly, and tailored to the specific performance characteristics of their particular engine capabilities.

Vita

Neal Alexander Harrison was born in Brampton, Ontario, Canada. Following graduation from high school, he attended Ryerson Polytechnic University in Toronto, Ontario. During his undergraduate career, he had several internships in the design engineering department at Boeing Toronto, Ltd. His undergraduate thesis work was carried out in cooperation with Boeing Phantom Works in Long Beach California on *Trailing Edge Device Design to Reduce Hinge Moments* for the Blended Wing-Body program. In 2001 he earned a Bachelor of Engineering in Aerospace Engineering with honors. Neal was accepted into the graduate aerospace engineering program at Virginia Tech in 2003, where he studied under Dr. Wing Ng and Dr. William Mason. While pursuing his degree, Neal worked for a local research company, Techsburg, Inc. in Blacksburg, Virginia, on a NASA funded program researching *Active Flow Control of Boundary Layer Ingesting Serpentine Diffusers*. Following graduation, Neal will be employed by Boeing Phantom Works in the Advanced Design Department as an Aerodynamicist.